Disconnected Contributions to Hadronic Processes

Dissertation
zur
Erlangung des Doktorgrades (Dr. rer. nat.)
der
Mathematisch-Naturwissenschaftlichen Fakultät
der
Rheinischen Friedrich-Wilhelms-Universität Bonn

von
Neramballi Ripunjay Acharya
aus
Tumkur, India

Bonn, 14.10.2019

Angefertigt mit Genehmigung der Mathematisch-Naturwissenschaftlichen Fakultät der Rheinischen Friedrich-Wilhelms-Universität Bonn.

1. Gutachter:	Prof. Dr. Dr. h. c. Ulf-G. Meißner
2. Gutachter:	Prof. Dr. Feng-Kun Guo
Tag der Promotion:	04.12.2019
Erscheinungsjahr:	2020

Dedicated to my parents, Nanda and Ravi.

अस्मिन् विकारः खहरे न राशावपि प्रविष्टेष्वपि निःसृतेषु ।
बहुष्वपि स्याल्लय-सृष्टिकालेऽनन्तेऽच्युते भूतगणेषु यद्वत् ।।

सिद्धांतशिरोमणि
भास्कराचार्यः

In the way that the infinite immutable *Brahma* (cosmos) is not affected by living beings entering or leaving it at the time of dissolution or creation, there is no change in the *Khahara* (infinity) by addition or subtraction.

$$\infty \pm a = \infty$$

Siddhanta-Shiromani
Bhaskaracharya
Indian mathematician, circa 1100 CE.

Acknowledgements

I would like to thank Prof. Dr. Dr. h.c. Ulf-G. Meißner for his supervision and leadership over the last four years. I am particularly grateful to him for the significance he placed on my education and growth during my PhD, especially during the more challenging times. I am also thankful to him for providing me with several opportunities to travel to various scientific fora, which were hugely beneficial towards the completion of this thesis.

I would like to thank Prof. Dr. Feng-kun Guo for spearheading the different projects that were completed during the course of my PhD. I am extremely grateful to him for the support he provided me with during my stay in China, which ensured a smooth transition to life in Beijing.

I am grateful to Prof. Dr. Ian C. Brock and Prof. Dr. Marc Alexander Schweitzer for serving on my doctoral committee, reading my thesis and providing me with valuable feedback.

I am very grateful to Dr. Chien-yeah Seng for his guidance and collaboration in the completion of the projects described in this work. I would also like to thank Dr. Dilege Gülmez, Dr. Mao-jun Yan, Dr. Shayan Ghosh and Rahul Mehra for stimulating discussions of physics, which greatly contributed to my scientific development over the last few years.

I am immensely thankful to Barbara Kraus for the numerous times she assisted me in the complicated bureaucratic matters which follow one in Germany. I would also like to thank Barbara and Christa Boersch for their assistance in the HISKP. I am also grateful to Matthias Frink for five years of constant support in the office, and for football on Wednesdays.

Over the last four years, my life was immeasurably enriched by the kindness of friends - in times of health-related strife and, especially, during the good times. I am supremely grateful to the following people for their benevolence in a countless different ways:

Anjishnu, for seven years of friendship, and especially for kidney-intestine solidarity and Tannenbusch tribulations;

Arshia, for motta roast and coastal camaraderie;

Bita, for unquestioningly giving me shelter whenever I needed it;

Dilege, for teaching me how to say ‘Entschuldigung’;

Gautam, for all the instances I treated his house as mine;

Ilkin, simply for letting me annoy her so much;

Kiran and VK, for Kannadiga food and companionship;

Malati and Gajanana Hegde, for providing me with a home away from home;

Mao-jun, for his unwavering support in Beijing;

Mathew, for all the ripping and curling;

Owen, for those wonderful nights of football, Shaala and everything else in Beijing;

Paulina, for countless quesadillas and for inspiring me to be a better planner;

Rahul, for taking me to the hospital while I insulted him;

Shayan, for the future, when AI-baba will arise;

Vishwas, for some sakkath bisibelebath and excellent evenings all over Bonn;
and Yang Yang, for showing me the hutongs and for my painting, which I will yet retrieve.

I am especially grateful to Rahul and Shayan for showing me how to take care of Pippy, to Ilkin for keeping me fed me while I wrote this thesis, and to Dilege for being my oldest and not-really-wisest friend in Germany.

I would like to thank Akhila, Manojna, Pooja and Sindhu for all the decades of laughter. I am extremely thankful to Shashi Achar and family for their support throughout my life.

I cannot imagine life in Germany without the enduring encouragement of Vasantha Dhanya, and I am immensely grateful for his support.

I would like to thank Krishna for her untethered zeal and for providing me with fountains of solace. I am grateful to her for the disconnection of the weight from the wait.

I would like to thank Kinnari, whose inimitable belief keeps me motivated and my life colourful. I am grateful to her for always leading the way with her righteous rage and rebellion.

I am grateful to my parents for all their sacrifices.

Abstract

Lattice quantum chromodynamics (QCD) is a powerful tool to calculate the dynamics of low-energy, non-perturbative QCD. It has made great strides in numerically evaluating hadronic observables by simulating the interactions of quarks and gluons on a lattice in finite volume. However, the evaluation of disconnected diagrams, which are Wick contraction diagrams containing quark propagators beginning and ending at the same time coordinates, has consistently proven to be a challenge. These diagrams have a low signal-to-noise ratio, and extracting the discrete energy shifts from the simulations of these diagrams is consequently either difficult, expensive or both. In this thesis, we devise a way of separating, analysing and evaluating the different connected and disconnected diagrams contributing to the process of $\pi\pi$ scattering. We use partially quenched chiral perturbation theory, an effective field theory of the enlarged, partially quenched QCD to perform this separation of connected and disconnected diagrams. This procedure is inherently unphysical, and requires the trick of partial quenching wherein extra, unphysical quarks are added to QCD. Using the extra mesons that are generated by these quarks, we construct single-channel amplitudes for the individual connected and disconnected diagrams. We derive fully analytical expressions for their scattering lengths and effective ranges. These expressions are then used to accurately determine certain unphysical low-energy constants, which are fed back into the Lüscher equation to provide concrete, numerical predictions of energy shifts of certain combinations of the connected and disconnected diagrams. These predictions are stringent bounds that any future lattice collaboration studying $\pi\pi$ scattering must adhere to. This thesis thus provides an exemplary formalism to study disconnected contributions in various hadronic processes, and displays the benefits of the interplay between effective field theory and lattice QCD studies.

Contents

CHAPTER 1

Introduction

The Standard Model of particle physics has been immensely successful in describing the fundamental constituents of nature at an unprecedented level of precision. However, one of its foremost shortcomings is that it does not provide a qualitative and foundational understanding of certain aspects of the strong sector. The Standard Model cannot yet offer a practically convenient and analytical, first-principles description of the phenomenology - a bountiful proliferation of quark-composite states called hadrons - of low-energy Quantum Chromodynamics (QCD). This is due to the non-perturbative nature of the strong coupling constant α_s at energies below 1 GeV and the phenomenon of quark confinement. Traditional perturbative approaches are, thus, invalid at these scales and the complex structure of hadrons and their dynamics need to be developed and comprehended via non-perturbative means or numerical methods.

Great progress in this regard has been made by two of the theoretical techniques exemplified in this work. Firstly, Chiral Perturbation Theory (ChPT), an Effective Field Theory (EFT), has not just unpeeled the low-energy hadronic spectrum, but has also yielded unprecedented insights into the complicated structure of the QCD vacuum. On the other hand, lattice QCD is a computational tool that allows the realisation of the hadronic spectrum via simulations of the QCD path integral on powerful computers. It is then only natural that, as these techniques mature, synergy and interplay between them become significant in the progression towards an era of precision and depth in calculations.

It is this juxtaposition between chiral effective field theory and lattice QCD that this thesis aims to exploit. Lattice QCD relies upon the ability to compute a large number of simulations on a finite-sized lattice, and this requires aspects such as cost and efficiency to be taken into consideration. The computation of numerous configurations of the QCD path integral on the lattice translates into the direct computation of multiple quark contraction diagrams for each process of interest, and the extraction of signals corresponding to these diagrams that can then be related to physical observables. It is in this evolving procedure that virtually all the lattice QCD collaborations have repeatedly found it either difficult, expensive or both to compute *disconnected diagrams*.

Disconnected diagrams are simply any Wick contraction diagrams that contain quark propagators that begin and end on the same time coordinates on the lattice. Almost every physical process computed on the lattice necessarily contains contributions from disconnected diagrams. While their computations have been improving steadily, extracting good signal-to-noise ratios or performing simulations quickly and efficiently is still a considerable technical challenge. It would then be invaluable to glean insights about disconnected diagrams and their relative contributions to physical

observables from other sources.

In this work, we employ effective field theoretical methods to, firstly, separate and then evaluate the different contributing diagrams appearing in the computation of $\pi\pi$ scattering on the lattice. The concept of EFTs has usually been used towards understanding physical processes, but here, this separation of connected and disconnected Wick contractions is an inherently unphysical process. In order to accomplish this, we extend ChPT into a larger, unphysical domain via a technique called *partial quenching*, to develop Partially Quenched ChPT (PQChPT). This enlarged theory contains unphysical mesons, and the different connected and disconnected diagrams are described via scattering processes of these mesons. We also chart a mechanism to relate these quantities, evaluated in the infinite volume, to the finite volume discrete energy levels computed on the lattice.

Since EFT is founded on the tested, immutable principles of quantum field theory - locality, causality, unitarity, cluster decomposition and renormalisability - the analytical and numerical results obtained via this method are a clear and precise guiding light to future lattice QCD investigations of this process. We also provide a general, predictive framework of separating, analysing and evaluating disconnected diagrams, which can be extended to other processes, depending on the status and requirements of lattice calculations in those processes. We, thus, deliver both a complementary analysis to lattice computations of $\pi\pi$ scattering, as well as specific, numerical bounds for energy levels for future lattice collaborations to heed.

This work begins with an overview of QCD in Chapter 2, and then describes the low-energy effective field theory of QCD, ChPT, in Chapter 3. In Chapter 4, we provide an explanation of partial quenching and the essentials of the unphysical effective theory of PQChPT. In Chapter 5, we perform the separation of connected and disconnected diagrams using PQChPT and provide analytical and numerical infinite volume results. The connection to specific lattice QCD data and finite volume results and predictions are provided in Chapter 6. The work concludes with a discussion of the results in Chapter 7.

1.1 Units and Conventions

Natural units are used in the entirety of this thesis,

$$\hbar = c = 1. \tag{1.1}$$

Repeated Lorentz and colour indices are summed, and the Feynman slash notation is used,

$$\not{D} = \gamma_\mu D^\mu. \tag{1.2}$$

1.2 List of Publications

Substantial sections of this thesis (in particular, Chapters 5 and 6) have been published in the following articles:

1. N. R. Acharya et al., *Connected and disconnected contractions in pion–pion scattering*, Nucl. Phys. **B922** (2017) 480, arXiv: 1704.06754 [hep-lat].

2. N. R. Acharya et al., *Constraints on disconnected contributions in $\pi\pi$ scattering*, JHEP **04** (2019) 165, arXiv: 1902.10290 [hep-lat].

The following article was also published during the period of this thesis:

3. N. R. Acharya et al., *Theta-dependence of the lightest meson resonances in QCD*, Phys. Rev. **D92** (2015) 054023, arXiv: 1507.08570 [hep-ph].

CHAPTER 2

Quantum Chromodynamics

2.1 The Standard Model

Quantum field theory (QFT) has been one of the most successful theories in the natural sciences. By extending the ancient notions of *matter* and *forces* to mathematically sound quantum fields, QFT enables us to comprehend nature at a fundamental, scrupulous level. The Standard Model of particle physics is the QFT that describes the fundamental matter and force particles [4–6]. Remarkably, the Standard Model appears to be valid across a broad energy range, and was conceived from a relatively small number of assumptions and principles. The central tenets of QFT - locality, causality, unitarity, cluster decomposition and renormalisability - when reinforced with certain symmetry properties, almost automatically yield a substantially predictive as well as extensively applicable theory. Though a glaring drawback of the theory is the nineteen input parameters the Standard Model requires, it has repeatedly survived intense experimental scrutiny over the last century[1].

The principles of locality, unitarity, analyticity and cluster decomposition are erected on firm foundations: they are imposed by the requirements of special relativity, quantum mechanics and their conjunction; renormalisability is essential if we aim to realise meaningful predictions at arbitrary energies that can be experimentally tested. Considerations due to principles of symmetry, historically, arose in concert with a host of experimental discoveries of new particles. The imposition of invariance under gauge symmetry, and the associated symmetry breaking scenarios, ineluctably explained unanticipated particles or predicted missing elements.

It is most convenient to express the dynamics of the Standard Model in the Lagrangian formalism, so that Lorentz invariance is manifest. The degrees of freedom of the Standard Model Lagrangian are embedded in the Lie group $SU(3)_C \otimes SU(2)_L \otimes U(1)_Y$. The spin-$\frac{1}{2}$ fermion fields and the spin-1 gauge boson fields, together with their antiparticles, interact with each other to induce the strong, weak and electromagnetic forces (Fig. 2.1). The fermions are comprised of quarks and leptons, which are organised in triplicate families by virtue of their hierarchical mass and flavour structure. Each force is accompanied by mediating gauge bosons - eight gluons for the strong force, the $W^{\pm}$ and the Z bosons for the weak force, and the photon γ for the electromagnetic force. The gluons and the photon are massless, while the $W^{\pm}$ and Z bosons are rendered massive due to Spontaneous Symmetry Breaking

[1] Outstanding success notwithstanding, we are now certain that the Standard Model is, if not incorrect, definitely incomplete. The discovery of neutrino masses, astrophysical evidence of dark matter and several niggling inconsistencies in the flavour sector indicate that the Standard Model is deficient (for reviews, see [7–9]).

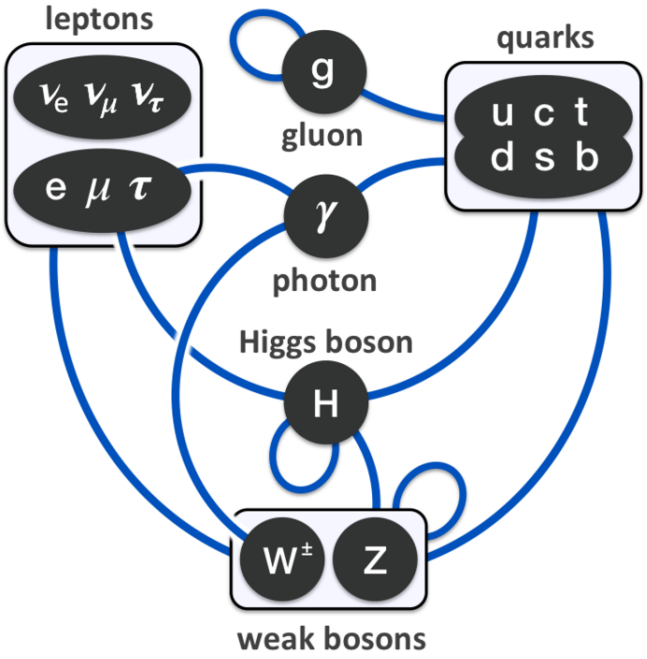

Figure 2.1: The fundamental constituents of the Standard Model. The lines indicate interactions, including self-interactions of the non-Abelian gauge bosons and the Higgs boson.

(SSB) of the electroweak gauge group into the electromagnetic group due to the vacuum,

$$SU(2)_L \otimes U(1)_Y \quad \xrightarrow{\text{SSB}} \quad U(1)_{\text{QED}}.$$

This SSB engenders the Higgs boson via Goldstone's Theorem, which in turn generates fermion masses and mixing in the Standard Model via the Yukawa terms [10, 11].

2.2 Symmetries of QCD

Quantum Chromodynamics (QCD) is the gauge theory that describes strong force interactions in the Standard Model. It is an enormously rich theory, with vastly different phenomena at low- and high-energy scales. It is also replete with myriad symmetries which lend it an abundant phenomenology.

2.2.1 Poincaré: Local $ISO(3,1)$

QCD is necessarily invariant under transformations belonging to the Poincaré group, which is the Lie group $ISO(3,1)$, since it is a relativistic QFT. The Poincaré group (or the inhomogeneous Lorentz group) is essentially the set of all constant translations added to the Lorentz group. It is a ten parameter group, and contains rotations and boosts due to the Lorentz transformations, in addition to translations. Thus, the QCD Lagrangian is invariant under the following transformations of the spacetime coordinate

x:

$$x' = T(\Lambda, a)x = \Lambda x + a, \tag{2.1}$$

where $T(\Lambda, a)$ is a $ISO(3,1)$ group element, and Λ represents Lorentz transformations which leaves the scalar product invariant,

$$(\Lambda x) \cdot (\Lambda y) = x \cdot y, \tag{2.2}$$

and has the specific properties of $\det \Lambda = 1$ and $\Lambda_0^0 \geq 1$ for the proper orthochronous Lorentz group $SO(3,1)$.

QCD is also invariant under $\mathcal{CPT}$ - charge conjugation (C), parity ($\mathcal{P}$) and time-reversal ($\mathcal{T}$) - since it is a relativistic, Lorentz invariant QFT and is subject to the $\mathcal{CPT}$ theorem [12].

2.2.2 Colour: Local $SU(3)_C$

The fundamental degrees of freedom of QCD are quarks and gluons,

$$\mathcal{L}_{QCD} = \sum_{f=1}^{N_f} \overline{q}_f \left[i\not{D} - m_q \right] q_f - \frac{1}{4} G^a_{\mu\nu} G^{\mu\nu}_a, \tag{2.3}$$

where

- q_f are the Dirac spinors representing quarks, which make up the matter content of the strong sector. Quarks belong to the *Dirac* representation of the Lorentz group $SO(3,1)$ and the *fundamental* representation **3** of the gauge group $SU(3)_C$. Quarks are thus $SU(3)_C$ triplets and are said to carry *colour* charges, which are usually denoted as red (R), green (G) or blue (B).
- N_f is the number of quark flavors. It is accepted that there are six flavors of quark: up, down, strange, charm, beauty and top.
- $D^\mu = \partial^\mu + igt^a A^{a,\mu}$ is the covariant derivative, which transforms in exactly the same way under gauge transformations as the Dirac spinor. The quark masses are denoted by m_q, while g is the coupling constant of the strong force. The interactions between quarks and gluons are thus contained in the covariant derivative.
- $G^a_{\mu\nu} = \partial_\mu A^a_\nu - \partial_\nu A^a_\mu + g f^{abc} A^b_\mu A^c_\nu$ is the gauge field strength tensor and a is the colour index carried by the gluon fields A_μ.
- $\left[t^a, t^b \right] = i f^{abc} t^c$ illustrates the non-Abelian nature of $SU(3)_C$, with f^{abc} the structure constant of the Lie group responsible for the gluon self-interactions.

The non-Abelian characteristic of $SU(3)_C$ also throws up a curious addition to Eq. (2.3),

$$\mathcal{L}_\theta = -\frac{\theta}{64\pi^2} \epsilon^{\mu\nu\rho\sigma} G^a_{\mu\nu} G^a_{\rho\sigma}. \tag{2.4}$$

The effects of the inclusion of this term, which occurs due to the topological nature of the non-Abelian gauge group, are parity ($\mathcal{P}$) and charge-parity ($\mathcal{CP}$) violating effects in QCD, leading to, for example, a neutron electric dipole moment (EDM) [13]. The latest bounds on the neutron EDM indicate that

the parameter θ is minuscule [14, 15]. That it is virtually zero, although allowed by gauge invariance, is an open fine-tuning question in the Standard Model [16]. We will ignore this term in this work.

2.2.3 Chiral: Global $SU(2)_R \times SU(2)_L$

In the limit of massless quarks $m_q \to 0$, Eq. (2.3) becomes

$$\mathcal{L}^0_{QCD} = \sum_{f=1}^{N_f} \overline{q}_f [i \not{D}] q_f - \frac{1}{4} G^a_{\mu\nu} G^{\mu\nu}_a . \tag{2.5}$$

Defining a new 'chirality' matrix $\gamma_5 = \gamma^5 = i\gamma^0\gamma^1\gamma^2\gamma^3$, we can introduce the projection operators,

$$\begin{aligned} P_R &= \tfrac{1}{2}\left(1 + \gamma_5\right), \\ P_L &= \tfrac{1}{2}\left(1 - \gamma_5\right), \end{aligned} \tag{2.6}$$

where R and L stand for 'right-' and 'left-handed'. The projection operators are 4×4 idempotent matrices which satisfy the usual completeness and orthogonality relations,

$$\begin{aligned} P^2_{R/L} &= P_{R/L}, \\ P_R + P_L &= 1, \\ P_R P_L &= P_L P_R = 0. \end{aligned} \tag{2.7}$$

These operators can be used to project the Dirac spinors into their 'chiral' components,

$$\begin{aligned} P_R q &= q_R, \\ P_L q &= q_L, \end{aligned} \tag{2.8}$$

and use this to decouple the left- and right-handed quark components,

$$\overline{q}\Gamma_i q = \begin{cases} \overline{q}_R \Gamma_1 q_R + \overline{q}_L \Gamma_1 q_L & \text{for } \Gamma_1 \in \left\{\gamma^\mu, \gamma^\mu\gamma_5\right\} \\ \overline{q}_R \Gamma_2 q_L + \overline{q}_L \Gamma_2 q_R & \text{for } \Gamma_2 \in \left\{1, \gamma_5, \sigma^{\mu\nu}\right\} \end{cases} . \tag{2.9}$$

Applying this to the first term of Eq. (2.5) gives

$$\mathcal{L}^0_{QCD} = \sum_{f=1}^{N_f} \overline{q}_{R,f} [i \not{D}] q_{R,f} + \overline{q}_{L,f} [i \not{D}] q_{L,f} - \frac{1}{4} G^a_{\mu\nu} G^{\mu\nu}_a . \tag{2.10}$$

The quark masses are determined from experiments and lattice simulations. There is a clear hierarchy in the masses of the different quark flavors [17],

$$\begin{pmatrix} m_u \approx 0.002 \text{ GeV} \\ m_d \approx 0.005 \text{ GeV} \\ m_s \approx 0.095 \text{ GeV} \end{pmatrix} \ll 1 \text{ GeV} \leq \begin{pmatrix} m_c \approx 1.28 \text{ GeV} \\ m_b \approx 4.18 \text{ GeV} \\ m_t \approx 173 \text{ GeV} \end{pmatrix}, \tag{2.11}$$

where the up, down and strange quarks are much lighter than the charm, beauty and top quarks. Here, the light quarks have been measured at a renormalisation scale ~ 2 GeV. This scale separation allows

us to explore the physics in the sub-1 GeV regime without having to explicitly consider the effects of the heavy quarks. In this work, we will go one step further and separate the up and down quarks from the strange quark, since $m_u, m_d \ll m_s$. The flavor-independence of the covariant derivative means that there is now a chiral symmetry in Eq. (2.10). The chiral Lagrangian $\mathcal{L}^0_{QCD}$ is invariant under independent transformations of the decoupled quark fields of the form

$$\begin{aligned} \begin{pmatrix} u_R \\ d_R \end{pmatrix} &\mapsto U_R \begin{pmatrix} u_R, \\ d_R \end{pmatrix} \\ \begin{pmatrix} u_L \\ d_L \end{pmatrix} &\mapsto U_L \begin{pmatrix} u_L \\ d_L \end{pmatrix}, \end{aligned} \tag{2.12}$$

where the $U_{R/L}$ are 2×2 unitary matrices which are group elements of $U(2)_{R/L}$. These can be parameterised as (see Appendix B)

$$\begin{aligned} U_R &= \exp\left(-i \sum_{a=1}^{3} \Theta_a^R \frac{\tau^a}{2}\right), \\ U_L &= \exp\left(-i \sum_{a=1}^{3} \Theta_a^L \frac{\tau^a}{2}\right). \end{aligned} \tag{2.13}$$

The parameters $\Theta_a^{R/L}$ are independent of the spacetime manifold, and this symmetry is a global $U(2)_R \times U(2)_L$ symmetry of the the massless QCD Lagrangian. This parameterisation implies that the Lagrangian is actually invariant under the transformations,

$$\begin{aligned} \begin{pmatrix} u_R \\ d_R \end{pmatrix} \mapsto U_R \begin{pmatrix} u_R \\ d_R \end{pmatrix} &= \exp\left(-i \sum_{a=1}^{3} \Theta_{Ra} \frac{\tau_a}{2}\right) e^{-i\Theta_R} \begin{pmatrix} u_R \\ d_R \end{pmatrix}, \\ \begin{pmatrix} u_L \\ d_L \end{pmatrix} \mapsto U_L \begin{pmatrix} u_L \\ d_L \end{pmatrix} &= \exp\left(-i \sum_{a=1}^{3} \Theta_{La} \frac{\tau_a}{2}\right) e^{-i\Theta_L} \begin{pmatrix} u_L \\ d_L \end{pmatrix}, \end{aligned} \tag{2.14}$$

which indicates that we have decomposed the symmetry as

$$\begin{array}{c} U(2)_R \times U(2)_L \\ \downarrow \\ SU(2)_R \times SU(2)_L \times U(1)_V \times U(1)_A \end{array},$$

with the new definitions $V = R + L$ and $A = R - L$, which stand for vector and axial vector respectively. The $SU(2)_R \times SU(2)_L$ symmetry is usually known as the chiral symmetry of QCD. We can promote this global $U(2)_R \times U(2)_L$ symmetry into a local one, by introducing spacetime dependence of the parameters $\Theta_a^{R/L}$. This allows us to apply Noether's theorem (Appendix A) to obtain eight conserved Noether currents at the classical level. For $SU(2)_{R/L}$, there are three currents each,

$$\begin{aligned} R^{\mu,a} &= \overline{q}_R \gamma^\mu \frac{\tau^a}{2} q_R, \quad \partial_\mu R^{\mu,a} = 0 \\ L^{\mu,a} &= \overline{q}_L \gamma^\mu \frac{\tau^a}{2} q_L, \quad \partial_\mu L^{\mu,a} = 0. \end{aligned} \tag{2.15}$$

The currents $R^{\mu,a}$ and $L^{\mu,a}$ transform as (**2,1**) and (**1,2**) under $SU(2)_R \times SU(2)_L$ respectively. It is convenient to redefine these currents using the vector and axial vector nomenclature,

$$\begin{aligned} V^{\mu,a} &= \overline{q}\gamma^{\mu}\frac{\tau^a}{2}q, \\ A^{\mu,a} &= \overline{q}\gamma^{\mu}\gamma_5\frac{\tau^a}{2}q. \end{aligned} \tag{2.16}$$

The $U(1)_{V/A}$ also generate a singlet current each,

$$\begin{aligned} V^{\mu} &= \overline{q}\gamma^{\mu}q, \\ A^{\mu} &= \overline{q}\gamma^{\mu}\gamma_5 q, \end{aligned} \tag{2.17}$$

where $\partial_\mu V^\mu = 0$ and the vector singlet current is conserved. This conserved vector current corresponds to *baryon number* (B) conservation and enables a definition of mesons ($B = 0$) and baryons ($B = 1$). However, the axial vector current is not conserved at the quantum level due to an anomaly [18, 19],

$$\partial_\mu A^\mu = \frac{g_s^2}{16\pi^2}\epsilon^{\mu\nu\rho\sigma}G^a_{\mu\nu}G^a_{\rho\sigma}, \tag{2.18}$$

which is related to the topological θ-term in Eq. (2.4), and its effects are virtually irrelevant to the contents of this work.

2.3 Symmetry Breaking in QCD

A striking feature of the Standard Model is not just the cohort of symmetries that seem to command its structure, but the multitude of symmetry breaking patterns it exhibits. By itself, QCD illustrates spontaneous symmetry breaking (SSB) as well as explicit symmetry breaking which are directly responsible for the huge number of composite quark states that have been experimentally detected.

2.3.1 Spontaneous Symmetry Breaking

Noether's theorem allows us to derive conserved charges for the different currents in Eq. (2.15),

$$\begin{aligned} Q^a_R(t) &= \int d^3x q^\dagger_R \frac{\tau^a}{2} q_R, \\ Q^a_L(t) &= \int d^3x q^\dagger_L \frac{\tau^a}{2} q_L. \end{aligned} \tag{2.19}$$

Since they are conserved charges, they commute with the massless QCD Hamiltonian,

$$\left[Q^a_{R/L}, H_0\right] = 0. \tag{2.20}$$

Similarly to Eq. (2.16), we can construct the linear combinations of the right- and left-handed currents, vector $Q^a_V = Q^a_R + Q^a_L$ and axial vector charges $Q^a_A = Q^a_R - Q^a_L$, which have opposite parity

transformations,

$$\begin{aligned} PQ_V^a P^{-1} &= Q_V^a, \\ PQ_A^a P^{-1} &= -Q_A^a. \end{aligned} \tag{2.21}$$

This directly implies a *parity doubling* for eigenstates of the QCD Hamiltonian H_0, where each positive parity state $|\phi\rangle$ is accompanied by a degenerate negative parity state [20]:

$$H_0|\phi\rangle = E|\phi\rangle, \tag{2.22}$$

where E is the eigenvalue and $P|\phi\rangle = +|\phi\rangle$. The commutativity of the charge operator Q_A^a with the Hamiltonian gives,

$$H_0 Q_A^a|\phi\rangle = Q_A^a H_0|\phi\rangle = EQ_A^a|\phi\rangle, \tag{2.23}$$

leading to

$$PQ_A^a|\phi\rangle = PQ_A^a P^{-1} P|\phi\rangle = -EQ_A^a|\phi\rangle. \tag{2.24}$$

Thus, the hadronic spectrum must contain a degenerate, negative parity state for each $|\phi\rangle$. It is clear, however, from empirical results that this parity doubling is not realised in nature, which indicates a fault in the above reasoning.

In the arguments presented above, we have made an implicit assumption that Q_A^a annihilates the vacuum. To illustrate this, consider a positive parity state $|\phi, +\rangle$ produced by a creation operator $a_\phi^\dagger$ and its corresponding negative parity state $|\psi, -\rangle$ created by $a_\psi^\dagger$. Both these states belong to an irreducible representation of the symmetry group $SU(2)_R \times SU(2)_L$, leading to an interdependence of the creation operators,

$$\left[Q_A^a, a_\phi^\dagger\right] = -t_{\phi\psi}^a a_\psi^\dagger, \tag{2.25}$$

where $t_{\phi\psi}^a$ is a constant denoting the mixing of the two states. The action of the charge operator on the positive parity state gives,

$$\begin{aligned} Q_A^a|\phi, +\rangle &= Q_A^a a_\phi^\dagger|0\rangle \\ &= \left[Q_A^a, a_\phi^\dagger\right]|0\rangle + a_\phi^\dagger Q_A^a|0\rangle \\ &= -t_{\phi\psi}^a a_\psi^\dagger|0\rangle + a_\phi^\dagger Q_A^a|0\rangle. \end{aligned} \tag{2.26}$$

The existence of the negative parity state $|\psi, -\rangle$ then requires that $Q_A^a|0\rangle = 0$. The members of the hadronic spectrum with the lowest masses are the pions, which form a triplet and exhibit isospin symmetry, which implies an $SU(2)$ symmetry. This means $Q_A^a|0\rangle \neq 0$ and a spontaneous symmetry breaking [21],

$$\begin{gathered} SU(2)_R \times SU(2)_L \\ \downarrow \\ SU(2)_V. \end{gathered} \tag{2.27}$$

In the case of $N_f = 3$, the inclusion of the strange quark results in an octet for the lowest-lying hadronic states, indicating an $SU(3)_V$ symmetry of the theory.

The ground state of QCD is shown to be invariant under $SU(3)_V \times U(1)_V$, with the three vector charges and the baryon number operator all annihilating the ground state,

$$Q_V^a|0\rangle = Q_V|0\rangle = 0. \tag{2.28}$$

Meson	Quark Content	Mass (MeV)
π^+/π^-	$u\bar{d}$ / $d\bar{u}$	140
π^0	$(u\bar{u} - d\bar{d})/\sqrt{2}$	135
K^+/K^-	$u\bar{s}$ / $s\bar{u}$	494
$K^0/\overline{K}^0$	$d\bar{s}$ / $s\bar{d}$	498
η	$(u\bar{u} + d\bar{d} - 2s\bar{s})/\sqrt{6}$	548
η'	$(u\bar{u} + d\bar{d} + s\bar{s})/\sqrt{3}$	958

Table 2.1: The masses of the lightest mesons [17]. The pions in the triplet $\{\pi^0, \pi^\pm\}$ all have almost exactly the same mass, and the differences arise only due to isospin breaking and electromagnetic effects. The mesons containing a strange quark are all much heavier than the pions, indicating that $SU(3)_V$ is not as strong as the $SU(2)_V$ symmetry, justifying the discussion after Eq. (2.11).

The Coleman-Mandula theorem asserts that the symmetry of the vacuum state is necessarily the symmetry of the Hamiltonian, and it is this symmetry that, consequently, determines the spectrum of the theory [22]. Thus, given the pion triplet as the lowest-lying members of the hadronic spectrum in the isospin limit ($m_u = m_d \ll m_s$), the assumption of Eq. (2.27) is validated. In Table 2.1, we show the masses of the lowest-lying mesons.

The triplet charge operators Q_V^a and Q_A^a do not form a closed algebra,

$$\begin{aligned} \left[Q_A^a, Q_A^b\right] &= i f^{abc} Q_V^c, \\ \left[Q_V^a, Q_A^b\right] &= i f^{abc} Q_A^c. \end{aligned} \tag{2.29}$$

According to Goldstone's theorem, then, for each axial vector generator Q_A^a which does not annihilate the vacuum, there exists a corresponding Nambu-Goldstone boson (NGB) field ϕ^a, leading to a triplet of NGBs: the pions $\{\pi^0, \pi^\pm\}$ [23–25]. This is consistent with the expectation that, according to the SSB pattern in Eq. (2.27), there need to be $N^2 - 1 = 3$ NGBs for $SU(2)$. These fields are massless,

$$m_\alpha^a = \left\langle 0 \left| e^{-i\alpha^a Q_A^a} \mathcal{H}_0 e^{i\alpha^a Q_A^a} \right| 0 \right\rangle = 0. \tag{2.30}$$

The properties of these NGBs are defined by the symmetry properties of the axial vector generators, and thus are pseudoscalar, with negative parity,

$$\phi^a(t, \vec{x}) \overset{P}{\longmapsto} -\phi^a(t, -\vec{x}). \tag{2.31}$$

The NGBs tranform linearly under the subgroup $SU(2)_V$ of the group $SU(2)_R \times SU(2)_L$,

$$\left[Q_V^a, \phi^b(x)\right] = i f^{abc} \phi^c(x). \tag{2.32}$$

Explicit Symmetry Breaking

The pseudoscalar NGBs are massless, according to Goldstone's theorem. However, in reality, the chiral limit is not exactly realised and the up and down quarks have small, non-zero masses. Introducing

quark masses induces an additional term in Eq. (2.10) which mixes the left- and right-handed quarks,

$$\mathcal{L}^{m}_{QCD} = -\overline{q}_R \mathcal{M} q_L - \overline{q}_L \mathcal{M}^{\dagger} q_R, \tag{2.33}$$

with

$$\mathcal{M} = \begin{pmatrix} m_u & 0 \\ 0 & m_d \end{pmatrix}. \tag{2.34}$$

This term *explicitly* breaks chiral symmetry in QCD. However, since the quark masses, especially in the case of just the up and down quarks, are much smaller than the pion masses (≈ 0.135 GeV), the chiral symmetry $SU(2)_R \times SU(2)_L$ is broken only weakly. It will be shown in the next chapter how these quark masses contribute to finite pion masses.

2.4 Running Coupling Constant and Asymptotic Freedom

As mentioned earlier, QCD exhibits vastly different phenomena at the lower and higher ends of its energy spectrum. This can most easily be charted by evaluating the beta function of the QCD coupling constant g from Eq. (2.3),

$$\beta(g) = \frac{d}{d(\ln \mu)} g(\mu), \tag{2.35}$$

where μ is the relevant energy scale. Specifically, for the case of non-Abelian $SU(3)_C$ [26, 27],

$$\beta(g) = -\left(11 - \frac{2N_f}{3}\right) \frac{g^3}{16\pi^2} + O\left(g^5\right). \tag{2.36}$$

For the physical case of six fermions, $N_f = 6$, the beta function remains negative, indicating that the coupling constant becomes weaker at smaller distances. Thus, at higher energies, the weaker coupling constant allows the usage of perturbation theory to evaluate the dynamics of the theory. This phenomenon of the diminishing strength of the strong force at higher energies is called asymptotic freedom. Conversely, at low energies (≤ 1 GeV), the coupling constant is too strong to meaningfully carry out perturbation theory. The solution of Eq. (2.35) at the lowest order is

$$\alpha_s(\mu) \equiv \frac{g^2(\mu)}{4\pi} = \frac{12\pi}{\left(33 - 2N_f\right) \ln\left(\frac{\mu^2}{\Lambda^2}\right)}, \tag{2.37}$$

with Λ an integration constant, which is a dimensionful parameter and replaces the dimensionless coupling constant g. Λ characterises the scale at which the coupling constant diverges, signalling the onset of the non-perturbative regime. $\Lambda \sim 211$ MeV when calculated in the $\overline{MS}$ scheme with $N_f = 5$ and a renormalisation scale $\mu = 2$ GeV [28]. At these energies, the only vestiges of quarks and gluons are hadrons due to the little-understood phenomenon of *confinement*. Any satisfactory description of the dynamics of the quark-composite hadrons thus requires alternative, non-perturbative techniques. In this work, we will focus on two of the most prominent and successful tools applied towards this end - Chiral Perturbation Theory and lattice QCD.

CHAPTER 3

Chiral Perturbation Theory

3.1 Effective Field Theories

The concept of an Effective Field Theory (EFT) has been the cornerstone of our endeavour to understand nature via physics. While the ultimate objective of physics has persistently been an ultimate theory that describes nature, across all energy ranges, in a single, singular formalism with minimal input parameters, the sheer magnitude of length scales pervading the universe has rendered this objective still inconceivable. It is fortuitous, then, that it is possible for us to separate the dynamics at, say, the longer length scales, without explicitly detailing the physics at shorter lengths. This *scale separation* has essentially endowed physics with the unprecedented predictive power that it has demonstrated in the last century. The method of effective field theories emphasises, formalises and exploits this ubiquitous feature of physics in a coherent and organised manner.

The notion and efficacy of EFTs is best illustrated by elucidating Chiral Perturbation Theory (ChPT), one of the most fruitful EFTs of the last few decades. It was mentioned earlier that confinement and the non-perturbative nature of QCD at low energies imply that an analytical first-principles description of hadron physics using quarks and gluons is practically impossible. The energy scales at which quarks and gluons, as fundamental degrees of freedom, explicitly affect dynamics are far-removed from the sub-1 GeV regime we are interested in. Scale separation, then, allows us to conjure up an EFT with the asymptotic hadron states as the fundamental degrees of freedom. Formally, this can be accomplished by invoking Weinberg's theorem [29],

"*If one writes down the most general possible Lagrangian, including all terms consistent with assumed symmetry principles, and then calculates matrix elements with this Lagrangian to any given order of perturbation theory, the result will simply be the most general possible S-matrix consistent with analyticity, perturbative unitarity, cluster decomposition and the assumed symmetry principles*".

To apply Weinberg's theorem in a productive and rigorous way, we need a cogent scheme to assemble, organise and order the possible terms in the effective Lagrangian. The salient features that need to be considered and executed in our expected theory of hadrons are:

- As mentioned, *scale separation* is crucial. In our theory with two light quarks and pions as asymptotic states, we encounter three distinct scales:
    1. Energies $\gg$ 10 GeV, at which quarks and gluons are virtually independent states, which are beyond the reach of the "low-energy" experimental probes relevant to the light hadrons.

2. Energies of $\sim$ 1 GeV $\equiv \Lambda$, which marks the onset of the non-perturbative phase of QCD. Hadrons inhabit this energy regime as the observable states.
3. The light quark masses, $\sim$ few MeV, which are minuscule compared to the scale of physics but need to be incorporated since they are responsible for the light pion masses via explicit symmetry breaking.

- Weinberg's theorem refers to "...all terms consistent with assumed symmetry principles...". This requires us to incorporate the symmetry principles of the parent theory, QCD, in our effective theory.
  1. The ChPT Lagrangian needs to integrate chiral symmetry and the symmetry breaking patterns exhibited in QCD. The Nambu-Goldstone bosons engendered by Spontaneous Symmetry Breaking (SSB) of chiral symmetry, which are the primary observable states at the relevant energy scales, are taken to be fundamental degrees of freedom in our EFT. Thus, ChPT is known as a *non-decoupling* EFT, since the degrees of freedom in ChPT are different from the underlying theory, QCD.
  2. It is also vital to ensure Lorentz invariance of the terms in the Lagrangian, in order to maintain a physically meaningful causal and analytical structure of the resulting S-matrix.
- In order to "write down the most general possible Lagrangian", it is necessary to formulate a scheme to organise the allowed terms of the Lagrangian - which are infinite in number.
  1. A *perturbative expansion* of the terms in the Lagrangian requires suitable expansion parameters. Since the dynamics of the theory are commanded by the energy regime within which the theory is valid, *momentum* is a pertinent expansion parameter. An expansion in momentum is also beneficial when evaluating Feynman diagrams: spacetime derivatives correspond to four-momenta in the derivation of Feynman rules. Given that $m_u, m_d \ll \Lambda$ and quark masses explicitly break chiral symmetry, *quark masses* are also a credible expansion parameter. Thus, a perturbative expansion in p/Λ and m_q/Λ is carried out to generate the infinite series of terms.
  2. The expansion parameters need to be accompanied by a *power counting scheme* that orders the infinite terms of the Lagrangian. Weinberg's power counting scheme, which orders a term by evaluating its *chiral dimension*, is used for ChPT.
  3. Using the chiral counting scheme, we can assign a chiral dimension to the building blocks of the ChPT Lagrangian - derivatives, Goldstone boson fields, external fields and mass terms.
  4. Lorentz invariance imposes another constraint on the successive terms in the perturbative expansion: Lorentz indices of the derivatives are always contracted with either the metric $\eta^{\mu\nu}$ or the Levi-Civita connection $\epsilon^{\mu\nu\rho\sigma}$, which means that the chiral Lagrangian for mesons can only contain terms of *even* chiral order,

$$\mathcal{L}_{ChPT} = \mathcal{L}_0 + \mathcal{L}_2 + \mathcal{L}_4 + \mathcal{L}_6 + \dots . \tag{3.1}$$

  5. Carrying out this procedure ensures that there are only a finite number of terms at each order, and delving deeper by evaluating observables order by order naturally increases the accuracy of our results.

- The infinite terms in the perturbative expansion of ChPT are accompanied by coefficients called Low-Energy Constants (LECs). The symmetry principles that constrain the terms themselves do not provide any restrictions on the nature of the LECs. The LECs contain the inherent information of QCD, and, in principle, can be evaluated by matching to the fundamental theory. In practice, however, in the case of QCD, such a matching procedure is impractical and the LECs are determined by fitting to experimental or lattice QCD data.

- The perturbative nature of the expansion of parameters, with an energy 'cut-off' Λ governing the scale of validity of the theory, also portends differences in *unitarity* and *renormalisability*. Unitarity is only satisfied perturbatively in ChPT, where successively higher order contributions are required to satisfy S-matrix unitarity. This naturally necessitates an infinite series of terms. Similarly, ChPT is non-renormalisable in the traditional sense, since it contains operators with mass dimension higher than four. The cancellation of divergences at a certain order requires contributions from the next order, and this procedure can be carried out successively until the required degree of accuracy is met.

ChPT is thus a model-independent perturbation theory for non-perturbative QCD rooted in the founding principles of QFT, which means that predictions of ChPT are stringent and reliable, within the valid energy regime [30]. On the other hand, traversing to higher orders becomes very complicated very quickly, since the number of unknown parameters increases drastically [31].

Weinberg's Power Counting Scheme

Weinberg's power counting scheme proffers a definition of the chiral dimension and allows the classification of different Feynman diagrams, using which the ChPT Lagrangian can be constructed [29]. For a specific diagram with V_n vertices from the $\mathcal{L}_n$ term in the Lagrangian, L independent loops and I internal lines, the *chiral dimension* is calculated as,

$$D = 4L - 2I + \sum_n nV_n. \tag{3.2}$$

Using $L = I - \sum_n V_n + 1$, the dependence on the number of internal lines can be eliminated,

$$D = \sum_n V_n(n-2) + 2L + 2. \tag{3.3}$$

To illustrate the applicability of the chiral dimension D, as a theoretical instrument, consider a rescaling of the expansion parameters in the following way: the external momenta rescaled as $p_i \to tp_i$ and the light-quark masses rescaled as $m_q \to t^2 m_q$[1]. This results in a rescaling of the amplitude of the diagram,

$$\mathcal{M}(tp_i, t^2 m_q) = t^D \mathcal{M}(p_i, m_q). \tag{3.4}$$

While there are infinite terms in the perturbative series expansion of the ChPT Lagrangian, Eq. (3.3) assures us that there is only a finite number of contributing terms at a given chiral dimension D, since there are finite combinations of loops and vertices. The application of momentum and quark masses as expansion parameters in ChPT is justified as it ensures that for small momenta and masses,

[1] The reason for these rescaling choices will become evident in the following section, from Eq. (3.40).

only diagrams with correspondingly small chiral dimension contribute to a certain process, with suppression of diagrams with higher D. This in turn automatically suppresses loop diagrams as evident from Eq. (3.3).

3.2 The Leading Order Lagrangian

The ChPT Lagrangian needs to be invariant under the chiral symmetry $(SU(2)_R \times SU(2)_L \times U(1)_V)$ transformation of the NGBs, with the three NGBs - $\{\pi^0, \pi^\pm\}$ - transforming as a triplet under the subgroup $H = SU(2)_V$. SSB dictates that the ground state must be invariant under $SU(2)_V \times U(1)_V$. Using the results from Appendix B, we can parameterise the pseudoscalar NGBs in the exponential representation,

$$U(x) = \exp\left(\frac{i\sqrt{2}\Phi}{F}\right), \tag{3.5}$$

where F is a dimensionful constant and,

$$\Phi = \sum_{i=1}^{2} \tau_i \phi_i(x) = \frac{1}{\sqrt{2}} \begin{pmatrix} \pi^0 & \sqrt{2}\pi^+ \\ \sqrt{2}\pi^- & -\pi^0 \end{pmatrix}. \tag{3.6}$$

$U(x)$ is the fundamental degree of freedom of the ChPT Lagrangian, and transforms non-linearly in the $(\mathbf{3}, \bar{\mathbf{3}})$ representation of global $SU(2)_R \times SU(2)_L$,

$$U(x) \mapsto RU(x)L^\dagger, \tag{3.7}$$

with R and L belonging to $SU(2)_R$ and $SU(2)_L$ respectively. After SSB, $R = L$ and $U(x)$ thus transforms linearly under transformations of $SU(2)_V$,

$$U(x) \mapsto LU(x)L^\dagger, \tag{3.8}$$

leaving the ground state $\Phi = 0$, $U_0 = 1$ invariant under vector transformations as required by SSB,

$$\begin{aligned} U_0 &\mapsto LU_0L^\dagger = LL^\dagger = \mathbb{1}, \\ U_0 &\mapsto A^\dagger U_0 A^\dagger = A^\dagger A^\dagger \neq \mathbb{1}. \end{aligned} \tag{3.9}$$

The chiral transformations of the remaining elementary blocks required for the kinetic terms in the Lagrangian follow,

$$\begin{aligned} \partial_\mu U &\mapsto R\partial_\mu UL^\dagger, \\ U^\dagger &\mapsto LU^\dagger R^\dagger, \\ \partial_\mu U &\mapsto L\partial_\mu U^\dagger R^\dagger. \end{aligned} \tag{3.10}$$

The NGBs in the ChPT Lagrangian require a derivative coupling, since the pions do not interact with each other at vanishing momenta. Thus, noting that the lowest order term in the Lagrangian,

corresponding to $\mathcal{L}_0$, is trivial since $UU^\dagger = 1$, the first consequential term in the ChPT Lagrangian is:

$$\mathcal{L}_K = \frac{F^2}{4}\left\langle \partial_\mu U^\dagger \partial^\mu U \right\rangle, \tag{3.11}$$

where $\langle \ldots \rangle = \mathrm{Tr}\,[\ldots]$ is the trace in flavour space. The different building blocks are chirally counted as,

$$U = O(p^0), \quad \partial_\mu U = O(p^1). \tag{3.12}$$

Using the cyclic property of the trace, it is easy to show that this term is indeed invariant under chiral transformations:

$$\mathcal{L}_K \mapsto \frac{F^2}{4}\left\langle L\partial_\mu U^\dagger R^\dagger R \partial^\mu U L^\dagger \right\rangle = \frac{F^2}{4}\left\langle L^\dagger L \partial_\mu U^\dagger \mathbb{1} \partial^\mu U \right\rangle = \frac{F^2}{4}\left\langle \partial_\mu U^\dagger \partial^\mu U \right\rangle. \tag{3.13}$$

Along with chiral symmetry invariance, we have ensured that the other symmetries of QCD - Poincaré invariance, charge conjugation C, parity $\mathcal{P}$ and time reversal $\mathcal{T}$ invariance (in the limit of vanishing θ-term Eq. (2.4)) - are all respected by this LO Lagrangian.

It is now possible to evaluate the Noether currents generated by chiral symmetry for this Lagrangian. In order to calculate the Noether currents, we first need to promote the global parameters Θ_R^a and Θ_L^a from Eq. (2.13) to local parameters with spacetime dependence. Setting $\Theta_R^a = 0$, to first order in Θ_L^a, we obtain,

$$\begin{aligned}
U &\mapsto RUL^\dagger = U\left(1 + i\Theta_a^L \frac{\tau^a}{2}\right), \\
U^\dagger &\mapsto \left(1 - i\Theta_a^L \frac{\tau^a}{2}\right) U^\dagger, \\
\partial_\mu U &\mapsto \partial_\mu U \left(1 + i\Theta_a^L \frac{\tau^a}{2}\right) + U i\partial_\mu \Theta_a^L \frac{\tau^a}{2}, \\
\partial_\mu U^\dagger &\mapsto \left(1 - i\Theta_a^L \frac{\tau^a}{2}\right) \partial_\mu U^\dagger - i\partial_\mu \Theta_a^L \frac{\tau^a}{2} U^\dagger.
\end{aligned} \tag{3.14}$$

Applying these to $\mathcal{L}_K$, the variation of the Lagrangian is,

$$\begin{aligned}
\delta\mathcal{L}_K &= \frac{F^2}{4}\left\langle U\partial_\mu \Theta_a^L \frac{\tau^a}{2}\partial^\mu U^\dagger + \partial_\mu U\left(-i\partial_\mu \Theta_a^L \frac{\tau^a}{2} U^\dagger\right)\right\rangle, \\
\delta\mathcal{L}_K &= \frac{F^2}{4} i\partial_\mu \Theta_a^L \left\langle \tau^a \partial^\mu U^\dagger U \right\rangle.
\end{aligned} \tag{3.15}$$

The left-handed Noether currents $\mathcal{L}_K$ are:

$$J_L^{a,\mu} = \frac{\partial\left(\delta\mathcal{L}_2\right)}{\partial(\partial_\mu \Theta_a^L)} = i\frac{F^2}{4}\left\langle \tau^a \partial^\mu U^\dagger U \right\rangle. \tag{3.16}$$

Similarly, we obtain the right-handed currents,

$$J_R^{a,\mu} = \frac{\partial\left(\delta\mathcal{L}_2\right)}{\partial(\partial_\mu \Theta_a^R)} = -i\frac{F^2}{4}\left\langle \tau^a U \partial^\mu U^\dagger \right\rangle. \tag{3.17}$$

The vector and axial vector currents are then just the linear combinations of the left- and right-handed currents,

$$\begin{aligned} J_V^{a,\mu} &= J_R^{a,\mu} + J_L^{a,\mu} = -i\tfrac{F}{4}\left\langle \tau^a \left[U, \partial^\mu U^\dagger\right]\right\rangle, \\ J_A^{a,\mu} &= J_R^{a,\mu} - J_L^{a,\mu} = -i\tfrac{F^2}{4}\left\langle \tau^a \left\{U, \partial^\mu U^\dagger\right\}\right\rangle. \end{aligned} \tag{3.18}$$

We can expand the field $U(x)$ in terms of the pion fields,

$$U = \mathbb{1} + \frac{i\sqrt{2}\Phi}{F} - \frac{\Phi^2}{F^2} + \dots . \tag{3.19}$$

The axial vector current $J_A^{a,\mu}$ contains terms with odd numbers of NGBs, and the leading term of this current is,

$$J_A^{a,\mu} = -F\partial^\mu \phi^a. \tag{3.20}$$

The current $J_A^{a,\mu}$, when contracted with the vacuum and a Goldstone boson state, returns a non-vanishing matrix element:

$$\left\langle 0 \left| J_A^{a,\mu}(x) \right| \phi^b(p) \right\rangle = ip^\mu F e^{-ip\cdot x}\delta^{ab}. \tag{3.21}$$

This relation shows that the constant F is related to physical pion-decay, and hence is called the "pion-decay constant" (in the chiral limit, $F = F_\pi$). It has been measured in the leptonic decay of the pion in the process $\pi^+ \to \ell^+ \nu_\ell$ to be $F_\pi = 92.2$ MeV [17].

3.2.1 Including Masses

As already mentioned, finite quark masses break chiral symmetry explicitly and lead to finite NGB masses. In order to incorporate these quark masses in the ChPT Lagrangian, we employ a technique called the *spurion* trick [32]. In our case, the spurion trick involves the following steps:

- The quark mass term is introduced as a spurion field that transforms appropriately in the fundamental theory, QCD,

  $$\mathcal{L}_{QCD}^m = -\overline{q}_R \mathcal{M} q_L - \overline{q}_L \mathcal{M}^\dagger q_R, \tag{3.22}$$

  where $\mathcal{M}$ is the spurion field,

  $$\mathcal{M} = \begin{pmatrix} m_u & 0 \\ 0 & m_d \end{pmatrix}. \tag{3.23}$$

- The transformation of the complex spurion field $\mathcal{M}$ under chiral symmetry,

  $$\mathcal{M} \mapsto R\mathcal{M}L^\dagger, \tag{3.24}$$

  allows its insertion as an operator in the ChPT Lagrangian along with the other building blocks. Chiral symmetry in the ChPT Lagrangian is, thus, broken in exactly the same way as in QCD.

- Once the invariant Lagrangian is constructed, the spurion field is set to its correct value - here, the physical quark masses, in the ensuing calculations.

Taking these steps into account, the form of the mass term to be added to the chiral Lagrangian

is [33],

$$\mathcal{L}_{\mathcal{M}} = \frac{F^2}{4}\left\langle \chi U^\dagger + \chi^\dagger U \right\rangle, \tag{3.25}$$

where a new parameter has been introduced:

$$\chi = 2B\mathcal{M}. \tag{3.26}$$

The parameter B is related to the scalar quark condensate as,

$$\Sigma = 2F^2 B = -\langle \overline{q}q \rangle. \tag{3.27}$$

Chiral symmetry also allows a term of the form $\left\langle \chi U^\dagger - \chi^\dagger U \right\rangle$ to be included in the lowest non-trivial Lagrangian, but this term has an opposite transformation under parity and is thus excluded.

Reading off the coefficients of the quadratic pion terms in the expansion of Eq. (3.25),

$$\begin{aligned} \frac{F^2}{4}\left\langle \chi U^\dagger + \chi^\dagger U \right\rangle &= \frac{F^2 B}{2}\left\langle \mathcal{M}U^\dagger + \mathcal{M}^\dagger U \right\rangle \\ &= F^2 B\left(m_u + m_d\right)\left(\mathbb{1} - \frac{\pi\cdot\pi}{2F^2} + \ldots\right) \end{aligned} \tag{3.28}$$

gives us the pion masses, which is the famous Gell-Mann–Oakes–Renner (GMOR) relation ($\overline{m} = \frac{1}{2}(m_u + m_d)$) [34]:

$$M^2 = B\left(m_u + m_d\right) = 2B\overline{m}. \tag{3.29}$$

The GMOR relation clarifies how the pion masses must be counted in the chiral power counting scheme,

$$m_q = O(p^2), \tag{3.30}$$

leading to

$$\chi = O(p^2). \tag{3.31}$$

Thus, we have formulated a complete leading order ChPT Lagrangian for the global, chiral $SU(2)_R \times SU(2)_L$ symmetry. In order to derive the Ward identities for ChPT, analogous to QCD, in the functional formalism, we require a locally invariant generating functional expansion of ChPT. The generating functional of QCD, with vector (v), axial vector (a), scalar (s) and pseudoscalar (p) external sources, $Z_{QCD}[v, a, s, p]$ must reproduce the ChPT generating functional in a series $Z^{(2)}[v, a, s, p] + Z^{(4)}[v, a, s, p] + \ldots$. This allows us to easily introduce any necessary external fields coupled with the NGBs in ChPT [33].

The building blocks for the complete, perturbatively expanded Lagrangian can be organised, then, based on their compliance with local, chiral symmetry, with the $SU(2)_R \times SU(2)_L$ group elements $R(x)$ and $L(x)$ now spacetime dependent.

- The pion field is most conveniently represented in the exponential parameterisation,

$$U = \exp\left(\frac{i\sqrt{2}\Phi}{F}\right), \tag{3.32}$$

and a local, chiral transformation of the NGBs encoded in

$$U(x) \mapsto R(x)U(x')L^{\dagger}(x). \tag{3.33}$$

- The covariant derivative is defined analogously to QCD,

$$D_\mu U \equiv \partial_\mu U - ir_\mu U + iUl_\mu, \tag{3.34}$$

and transforms identically to the NGB,

$$D_\mu U \mapsto R(D_\mu U)L^{\dagger}. \tag{3.35}$$

- The gauge boson fields of the theory are defined via the field strength tensors,

$$\begin{aligned} f^R_{\mu\nu} &\equiv \partial_\mu r_\nu - \partial_\nu r_\mu + i\left[r_\mu, r_\nu\right], \\ f^L_{\mu\nu} &\equiv \partial_\mu l_\nu - \partial_\nu l_\mu + i\left[l_\mu, l_\nu\right], \end{aligned} \tag{3.36}$$

and the left- and right-handed gauge bosons are combined linearly to give us the vector $v_\mu = \frac{1}{2}(r_\mu + l_\mu)$ and axial vector $a_\mu = \frac{1}{2}(r_\mu - l_\mu)$ gauge bosons in Eq. (3.34). The field strength tensors transform as,

$$\begin{aligned} f^R_{\mu\nu} &\mapsto R f^R_{\mu\nu} R^{\dagger}, \\ f^L_{\mu\nu} &\mapsto L f^L_{\mu\nu} L^{\dagger}. \end{aligned} \tag{3.37}$$

- The spurion trick is now elevated to include the external scalar and pseudoscalar sources,

$$\chi \equiv 2B(s + ip) = 2B\mathcal{M}, \tag{3.38}$$

so that χ transforms similarly to the field U,

$$\chi \mapsto R\chi L^{\dagger}. \tag{3.39}$$

Applying the chiral counting scheme to our building blocks,

$$\begin{aligned} U &= O(p^0), \\ D_\mu U &= O(p^1), \\ r_\mu, l_\mu &= O(p^1), \\ f^{R/L}_{\mu\nu} &= O(p^2), \\ \chi &= O(p^2). \end{aligned} \tag{3.40}$$

In concert with the discrete symmetries of charge conjugation (C), parity ($\mathcal{P}$) and time-reversal invariance ($\mathcal{T}$) and Lorentz invariance, the effective chiral Lagrangian, with manifest local, chiral invariance, can be constructed order by order. Given any objects A, B, C and D transforming as $RXL^{\dagger}$

($X = A, B, C, D$) under $SU(2)_R \times SU(2)_L$, chirally invariant terms are constructed as

$$\begin{aligned} &\left\langle AB^\dagger \right\rangle, \\ &\left\langle AB^\dagger CD^\dagger \right\rangle, \\ &\left\langle AB^\dagger \right\rangle \cdot \left\langle CD^\dagger \right\rangle \quad \text{and so on,} \end{aligned} \tag{3.41}$$

where the cyclic property of the flavour trace has been exploited. The argument of Lorentz invariance impelling only terms in the Lagrangian of even chiral order still holds, and combining all the above constraints finally gives us the leading order (LO), locally invariant ChPT Lagrangian,

$$\mathcal{L}_2 = \frac{F^2}{4} \left\langle D_\mu U^\dagger D^\mu U \right\rangle + \frac{F^2}{4} \left\langle \chi U^\dagger + \chi^\dagger U \right\rangle. \tag{3.42}$$

The two free parameters of $\mathcal{L}_2$ are the pion-decay constant F and B, which is associated with the scalar quark condensate. This LO Lagrangian may be expanded in terms of the physical pion fields to calculate physical results such as the pion masses and LO scattering amplitudes,

$$\begin{aligned} \mathcal{L}_2 =& \frac{1}{2} \left[\partial_\mu \pi \cdot \partial^\mu \pi - M^2 \pi \cdot \pi \right] + \frac{1}{6F^2} \left[\left(\pi \cdot \partial_\mu \pi \right) \left(\pi \cdot \partial^\mu \pi \right) - \left(\pi \cdot \pi \right) \left(\partial_\mu \pi \cdot \partial^\mu \pi \right) \right] \\ &+ \frac{1}{24F^2} \left[M^2 (\pi \cdot \pi)^2 \right] + O\left(\pi^6 \right), \end{aligned} \tag{3.43}$$

where $\pi \cdot \pi = \pi^a \pi^a$ is the vector product, and the GMOR relation of Eq. (3.29) has been applied to make the pion masses explicit. The LO $\pi\pi$ scattering amplitude is easily evaluated from this expansion [29],

$$A(s,t,u) = \frac{s - M^2}{F^2}, \tag{3.44}$$

where $s = (p_1 + p_2)^2$, $t = (p_1 - p_3)^2$ and $s = (p_1 - p_4)^2$ are the usual Mandelstam variables constructed to present a Lorentz-invariant scattering amplitude.

The $\pi\pi$ scattering amplitude is analytic on the complex s-plane, which follows from Weinberg's theorem, and this property manifests as *crossing symmetry* of the scattering amplitudes. Utilising this in the isospin limit ($m_u = m_d$), we obtain simple relations for the different isospin (I) projected $\pi\pi$ scattering amplitudes [35]:

$$\begin{aligned} T^{I=0} &= 3A(s,t,u) + A(t,u,s) + A(u,s,t), \\ T^{I=1} &= A(t,u,s) - A(u,s,t), \\ T^{I=2} &= A(t,u,s) + A(u,s,t). \end{aligned} \tag{3.45}$$

3.3 Next-to-Leading Order

3.3.1 Unitarity and Renormalisability

We now expound upon the need to progress to higher orders of the ChPT Lagrangian. As mentioned in Section 3.1, due to the perturbative nature and construction of ChPT, the essential requirements of

unitarity and renormalisability require the inclusion of successive, higher-order terms in the chiral expansion. Unitarity is one of the core principles of QFTs, and satisfaction of unitarity constraints in the theory is crucial to maintain the physical validity of the resulting S-matrix elements. S-matrix unitarity can be written simply as [36],

$$SS^\dagger = S^\dagger S = \mathbb{1}, \tag{3.46}$$

which translates for the T-matrix ($S = \mathbb{1} + iT$) as,

$$T - T^\dagger = iTT^\dagger. \tag{3.47}$$

For any partial wave-projected amplitude T_l, this relation takes the form,

$$\operatorname{Im} T_l(s) = \sigma(s) \left|T_l(s)\right|^2, \tag{3.48}$$

where $\sigma(s)$ is the two-body phase space factor. However, the LO scattering amplitude Eq. (3.44) clearly does not contain an imaginary part and unitarity is broken. Unitarity, then, is only satisfied perturbatively, and the inclusion of successively higher-order terms are thus necessary,

$$\begin{aligned} &\operatorname{Im} T_l^{(2)}(s) = 0, \\ &\operatorname{Im} T_l^{(4)}(s) = \sigma(s) \left|T_l^{(2)}(s)\right|^2, \ \ldots \ . \end{aligned} \tag{3.49}$$

In order for these relations to quantitatively work, it is also necessary for there to be enough counterterms at each successive order to cancel the ultraviolet divergences arising from loop diagrams, which provide the requisite imaginary parts to satisfy Eq. (3.48) at each order. Thus, including all the possible terms in the Lagrangian, according to Weinberg's theorem, would ensure that we have a complete, unitary and renormalisable theory.

3.3.2 The NLO Lagrangian

The Next-to-Leading Order (NLO) Lagrangian is constructed analogously to the LO Lagrangian, by assembling all possible operators to make up $O(p^4)$ terms. This is not an entirely straightforward procedure, as minimising the basis of terms to obtain the most general, minimal Lagrangian requires careful handling of each term. The process of utilising the equations of motion of $\mathcal{L}_2$ to eliminate redundant terms in the expressions has been outlined in [33], and the final form of the $\mathcal{L}_4$ is:

$$\begin{aligned} \mathcal{L}_4 =& \frac{l_1}{4}\left\langle D_\mu U^\dagger D^\mu U\right\rangle^2 + \frac{l_2}{4}\left\langle D_\mu U^\dagger D_\nu U\right\rangle\left\langle D^\mu U^\dagger D^\nu U\right\rangle + \frac{l_3}{16}\left\langle \chi^\dagger U + \chi U^\dagger\right\rangle^2 \\ &+ \frac{l_4}{4}\left\langle D_\mu \chi^\dagger D^\mu U + D_\mu \chi D^\mu U^\dagger\right\rangle + \frac{l_5}{4}\left\langle U^\dagger f^R_{\mu\nu} U f_{\mu\nu}\right\rangle \\ &+ \frac{il_6}{2}\left\langle f^R_{f\nu} D^\mu U D^\nu U^\dagger + f^L_{\mu\nu} D^\mu U^\dagger D^\nu U\right\rangle - \frac{l_7}{16}\left\langle \chi^\dagger U - \chi U^\dagger\right\rangle^2 \\ &+ \frac{h_1+h_3}{4}\left\langle \chi^\dagger \chi\right\rangle + \frac{h_1-h_3}{2}\operatorname{Re}(\det \chi) - h_2\left\langle f^L_{\mu\nu'} J^{L,\mu\nu} + f^R_{\mu\nu} f^{R,\mu\nu}\right\rangle. \end{aligned} \tag{3.50}$$

The seven coefficients l_i are known as the Low-Energy Constants (LECs), and the h_i are the so-called High-Energy Constants, which accompany only external fields and are irrelevant for our investigations into meson-meson scattering. This $SU(2)$ NLO Lagrangian has three fewer terms than the corresponding NLO Lagrangian in the $SU(3)$ Lagrangian [37]. This is due to the implementation of the Cayley-Hamilton theorem for $SU(2)$ matrices that renders some of the terms redundant.

We can now use Weinberg's power counting scheme to classify the diagrams contributing to the $\pi\pi$ scattering amplitude up to NLO:

$$D = \sum_n V_n(n-2) + 2L + 2. \tag{3.51}$$

At leading order, we have $D = 2$, $n = 2$, leaving us with no loops, $L = 0$, and only the tree-level diagram of the $\mathcal{L}_2$ contributes to the amplitude (Fig. 3.1).

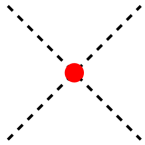

Figure 3.1: Leading-order tree level diagram, from the $\mathcal{L}_2$ vertex (circle, red).

At next-to-leading order, the chiral dimension is $D = 4$ and this leaves us with two possibilities:

- $n = 4$: this gives $L = 0$, so we have a tree-level diagram with the $\mathcal{L}_4$ vertex (Fig. 3.2).

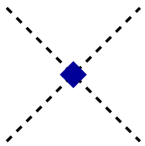

Figure 3.2: Next-to-leading order tree level diagram from the $\mathcal{L}_4$ vertex (square, blue).

- $n = 2$: here, $L = 1$, and the one-loop diagrams - two-point loop, tadpole contribution and external leg correction - due to $\mathcal{L}_2$ contribute to the amplitude (Fig. 3.3, Fig. 3.4 and Fig. 3.5).

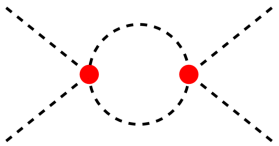

Figure 3.3: Two-point loop from $\mathcal{L}_2$.

These loop diagrams from the LO Lagrangian contain divergences that need to be renormalised. As alluded to earlier in this chapter, the inclusion of the NLO Lagrangian is necessary for the absorption of the infinities arising from the loops: the LECs l_i are modified by counterterms to absorb the divergences,

$$l_i = l_i^r + \gamma_i \lambda, \quad i = 1, \ldots, 7, \tag{3.52}$$

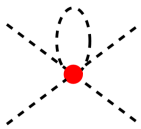

Figure 3.4: Tadpole vertex correction from $\mathcal{L}_2$.

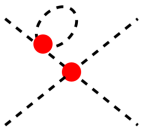

Figure 3.5: External leg correction from $\mathcal{L}_2$.

where the γ_i are coefficients given in Appendix C. The pole is contained in λ,

$$\lambda = \frac{1}{4\pi^2}\mu^{d-4}\left[\frac{1}{d-4} - \frac{1}{2}\left(\ln 4\pi + \Gamma'(1) + 1\right)\right], \tag{3.53}$$

with μ the renormalisation scale, $\Gamma'(1)$ is the Euler-Mascheroni constant and l_i^r, the renormalised LECs, are finite and scale-dependent. The scale-dependence of the renormalised LECs cancels with the scale dependence of the loop integrals, leaving the physical observables scale-independent. The l_i^r are independent of the quark masses as well, rendering them impossible to determine from the fundamental properties of QCD, such as symmetries, and need to be extracted from fitting to experimental or lattice QCD data.

3.3.3 Mass, Wavefunction and Pion-decay Constant Renormalisation

As a first application of the NLO Lagrangian, we evaluate its corrections to the pion mass. The pion mass is evaluated from the two-point correlation function, with the pionic operators time-ordered (T),

$$i\delta^{ab}\Delta(p) = \int d^4x\, e^{-ip\cdot x}\left\langle 0\left|T[\pi^a\pi^b]\right|0\right\rangle. \tag{3.54}$$

The pole of the Fourier transform of this correlator gives the lowest order pion mass,

$$i\Delta(p) = \frac{i}{p^2 - M^2 + i\epsilon}, \tag{3.55}$$

with M the pion mass from Eq. (3.29).

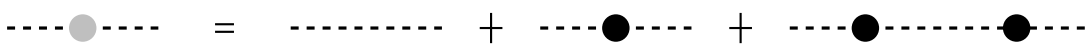

Figure 3.6: The unrenormalised propagator is a sum of self-energy diagrams. Here, the dark shaded vertices represent one-particle irreducible (1PI) diagrams. The infinite sum of higher order propagators can be represented as a geometric series.

The inclusion of diagrams from the NLO Lagrangian will induce corrections to the pion mass due

to self-energy factors from higher order propagators (Fig. 3.6):

$$\begin{aligned} i\Delta(p) &= \frac{i}{p^2 - M^2 + i\epsilon} + \frac{i}{p^2 - M^2 + i\epsilon}\left(-i\Sigma(p^2)\right)\frac{i}{p^2 - M^2 + i\epsilon} + \dots \\ &= \frac{i}{p^2 - M^2 - \Sigma(p^2) + i\epsilon}\,. \end{aligned} \tag{3.56}$$

Thus, the pion mass is renormalised by the higher order contributions, and the physical pion mass is given by the pole of Eq. (3.56):

$$M_\pi^2 - M^2 - \Sigma(M_\pi^2) = 0. \tag{3.57}$$

Figure 3.7: Diagrams contributing to the self-energy at $D = 4$.

The diagrams contributing to pion mass renormalisation up to NLO, obtained from the application of the chiral power counting arguments as before, are shown in Fig. 3.7. Here, we have two external lines (since it is a two-point correlator), and the pertinent Lagrangian terms are,

$$\mathcal{L}_{SE} = \mathcal{L}_2^{4\pi} + \mathcal{L}_4^{2\pi}. \tag{3.58}$$

The physical pion mass, thus, is a sum of a loop contribution from $\mathcal{L}_2$ and the tree-level propagator from $\mathcal{L}_4$. From Eq. (3.50), the only terms contributing to the tree-level pion propagator are the l_3 and l_7 terms,

$$\mathcal{L}_4^{2\pi} = -\frac{2l_3}{F^2}M^4(\pi\cdot\pi) + \frac{2l_7}{F^2}B^2\left(m_d - m_u\right)^2(\pi^0\pi^0). \tag{3.59}$$

Clearly, the l_7 term contribution vanishes in the isospin limit $m_u = m_d$, and contributes to the difference in masses of the charged and neutral pions. Using dimensional regularisation (Appendix C) and renormalising the divergences using the modified $\overline{MS}$ scheme (MS stands for Minimal Subtraction), the pion masses are evaluated to be [33],

$$\begin{aligned} M_{\pi^+}^2 &= M^2 + \frac{M^4}{F^2}\left(2l_3^r + \ln\frac{M^2}{\mu^2}\right), \\ M_{\pi^0}^2 &= M_{\pi^+}^2 - \frac{2l_7B^2}{F^2}\left(m_d - m_u\right)^2. \end{aligned} \tag{3.60}$$

These relations can be framed in a scale invariant way by redefining the LECs using

$$l_i^r = \frac{\gamma_i}{32\pi^2}\left(\bar{l}_i + \ln\frac{M^2}{\mu^2}\right), \quad i = 1,\dots,6. \tag{3.61}$$

The neutral and charged pion masses up to one-loop in ChPT are,

$$\begin{aligned} M_{\pi^+}^2 &= M^2 + \frac{M^4}{32\pi^2 F^2}\bar{l}_3, \\ M_{\pi^0}^2 &= M_{\pi^+}^2 - \frac{2l_7 B^2}{F^2}\left(m_d - m_u\right)^2, \end{aligned} \tag{3.62}$$

which simplify in the isospin limit to,

$$M_\pi^2 = M^2 + \frac{M^4}{32\pi^2 F^2}\bar{l}_3. \tag{3.63}$$

A similar procedure can be used to calculate the wave-function renormalisation Z_π [33],

$$Z_\pi = 1 + \frac{4}{3}\mu_\pi - \frac{2M_\pi^2}{F_\pi^2}l_4^r - \frac{8M_\pi^2}{3F_\pi^2}\lambda, \tag{3.64}$$

and the renormalisation of the pion-decay constant [33],

$$F_\pi = F\left(1 + \frac{M_\pi^2}{16\pi^2 F_\pi^2}\bar{l}_4\right). \tag{3.65}$$

Here, we have introduced μ_π, which is dependent on the chiral logarithm,

$$\mu_\pi \equiv -\frac{M_\pi^2}{32\pi^2 F_\pi^2}\ln\frac{\mu^2}{M_\pi^2}. \tag{3.66}$$

Thus, all scale dependence and infinities are absent in the expressions for the pion masses and the pion-decay constant, which are both physically relevant quantities.

3.3.4 $\pi\pi$ Scattering

Evaluating the contributions of all the relevant diagrams (Figs. 3.1 to 3.5), then, gives us the final $\pi\pi$ scattering amplitude up to NLO, $A(s,t,u) = A_{\pi^+\pi^-\to\pi^0\pi^0}(s,t,u)$, in $SU(2)$ ChPT [33]:

$$\begin{aligned} A_2(s,t,u) =& \frac{s-M^2}{F^2}, \\ A_4(s,t,u) =& B(s,t,u) + C(s,t,u), \\ B(s,t,u) =& \frac{1}{6F^2}\left\{3(s^2-M^4)\overline{J}(s) + \left[t(t-u) - 2M^2t + 4M^2u - 2M^4\right]\overline{J}(t)\right\} \\ &+ \left[u(u-t) - 2M^2u + 4M^2t - 2M^4\right]\overline{J}(u)\Big\}, \\ C(s,t,u) =& \frac{1}{96\pi^2F^4}\left\{2\left(\bar{l}_1 - \frac{4}{3}\right)(s-2M^2)^2 + \left(\bar{l}_2 - \frac{5}{6}\right)\left[s^2 + (t-u)^2\right] - 12M^2s + 15M^4\right\}, \end{aligned} \tag{3.67}$$

where s, t, u are the Mandelstam variables and $\overline{J}(s)$ is a representation of the loop integral (Appendix C),

$$\begin{aligned}\overline{J}(s) &= \frac{1}{16\pi^2}\left[\sigma(s)\ln\frac{\sigma(s)-1}{\sigma(s)+1}+2\right],\\ \sigma(s) &= \sqrt{1-\frac{4M^2}{q^2}}.\end{aligned} \tag{3.68}$$

Thus, the full amplitude in the isospin limit contains only four low-energy constants: F, M, $\bar{l}_1$ and $\bar{l}_2$. The amplitude $A_2(s,t,u)$ in Eq. (3.67), is again the LO scattering amplitude in Eq. (3.44) and the contributions due to the loops from $\mathcal{L}_2$ are contained in $B(s,t,u)$. $C(s,t,u)$ contains the contributions from the tree-level $\mathcal{L}_4$ diagram, Fig. 3.2. In this representation, the parameters F and M are simply the bare parameters, defined by Eq. (3.21) and Eq. (3.29) respectively [33].

CHAPTER 4

Partial Quenching

The goal of this work is to gain a better understanding of *disconnected diagrams* arising in lattice QCD calculations of mesonic processes, using effective field theoretical methods. The process of separating and calculating the effects of these disconnected diagrams is inherently unphysical, and this requires a modification of Chiral Perturbation Theory.

4.1 Partially Quenched QCD

Partial quenching is the process of setting the “sea" or “dynamical" quark masses different from the “valence" quark masses in a QCD correlation function [38–40]. This is possible since the quark masses appear in two distinct ways in the correlation function - in the determinant and in the propagators,

$$\begin{aligned} C_\pi(\tau) &= -\left\langle \sum_{\vec{x}} \overline{u}\gamma_5 d(\vec{x},\tau)\overline{d}\gamma_5 u(0)\right\rangle \\ &\equiv -\frac{1}{Z}\int DU\prod_q Dq D\overline{q}\; e^{-S_{\text{gauge}}-\int_x \sum_q \overline{q}(\not{D}+m_q)q}\sum_{\vec{x}}\overline{u}\gamma_5 d(\vec{x},\tau)\overline{d}\gamma_5 u(0) \\ &= \frac{1}{Z}\int DU\prod_q \det(\not{D}+m_q)e^{-S_{\text{gauge}}}\sum_{\vec{x}}\text{tr}\left[\gamma_5\left(\frac{1}{\not{D}+m_d}\right)_{x0}\gamma_5\left(\frac{1}{\not{D}+m_u}\right)_{0x}\right]. \end{aligned} \tag{4.1}$$

Here, we have used the pion correlator to illustrate the two ways the quark masses appear in the correlation function in Euclidean space [41, 42]. u, d are the quark spinor fields, m_i are the respective quark masses and Z is the QCD generating functional. In going from the second line to the third in Eq. (4.1), the functional integral for the quarks has been evaluated to give the determinant, $\det(\not{D}+m_q)$. While the calculation of physical observables and the preservation of unitarity require $m_S = m_V$, we have the freedom to set these masses to be different and deviate from the physical domain. Concurrently, we also retain the ability to revert back to the physical realm by setting the sea and valence quark masses to be equal.

Our aim is to develop an EFT of partially quenched quantum chromodynamics (PQQCD), so that this EFT can then be quantitatively related to QCD. This requires a PQQCD that has its symmetries explicitly manifest, since it is these symmetries that drive the formulation of the EFT. To this end, we begin by employing Morel’s trick and introduce *commuting* fermion fields called ‘ghost’ quarks into

our PQQCD [43],

$$\int D\widetilde{q}^{\dagger} D\widetilde{q} e^{-\widetilde{q}^{\dagger}(\not{D}+m_q)\widetilde{q}} = \frac{1}{\det(\not{D}+m_q)}, \tag{4.2}$$

since their determinant cancels out the determinant due to the valence quark,

$$\int D\overline{q} D q e^{-\overline{q}(\not{D}+m_q)q} = \det(\not{D}+m_q). \tag{4.3}$$

This means that PQQCD has three distinct types of quarks, which can be compactly organised into $N+2M$-dimensional vectors (N = number of sea quarks, M = number of valence/ghost quarks),

$$\overline{Q} = (\underbrace{\overline{q}_{S1},\ldots,\overline{q}_{SN}}_{\text{sea}},\underbrace{\overline{q}_{V1},\ldots,\overline{q}_{VM}}_{\text{valence}},\underbrace{\widetilde{q}^{\dagger}_{V_1},\ldots,\widetilde{q}^{\dagger}_{VM}}_{\text{ghost}}). \tag{4.4}$$

The masses may be arranged similarly,

$$\mathcal{M} = (\underbrace{m_{S1},\ldots,m_{SN}}_{\text{sea}},\underbrace{m_{V1},\ldots,m_{VM}}_{\text{valence}},\underbrace{m_{V1},\ldots,m_{VM}}_{\text{ghost}}). \tag{4.5}$$

The QCD Lagrangian then is the same as in Eq. (2.3), with the modification in the fermionic part of the Lagrangian,

$$\begin{aligned}\overline{Q}(\not{D}+\mathcal{M})Q = &\sum_{j=1}^{N}\overline{q}_{Sj}(\not{D}+m_{Sj})q_{Sj} + \sum_{i=1}^{M}\overline{q}_{Vi}(\not{D}+m_{Vi})q_{Vi} \\ &+ \sum_{k=1}^{M}\widetilde{q}^{\dagger}_{Vk}(\not{D}+m_{Vk})\widetilde{q}_{Vk}.\end{aligned} \tag{4.6}$$

This procedure, however, returns the QCD generating functional since

$$\begin{aligned}Z_{\text{PQ}} &= \int DUD\overline{Q}DQe^{-S_{\text{PQ}}} \\ &= \int DUe^{-S_{\text{gauge}}}\prod_{i=1}^{M}\left(\frac{\det(\not{D}+m_{Vi})}{\det(\not{D}+m_{Vi})}\right)\prod_{j=1}^{N}\det(\not{D}+m_{Sj}) \\ &= \int DUe^{-S_{\text{gauge}}}\prod_{j=1}^{N}\det(\not{D}+m_{Sj}) \\ &= Z_{\text{QCD}},\end{aligned} \tag{4.7}$$

where a modification to the functional integral measure has been induced,

$$D\overline{Q}DQ \equiv \prod_{i=1}^{M}\left(D\overline{q}_{Vi}Dq_{Vi}D\widetilde{q}^{\dagger}_{Vi}D\widetilde{q}_{Vi}\right)\prod_{j=1}^{N}\left(D\overline{q}_{Sj}Dq_{Sj}\right). \tag{4.8}$$

The application of partial quenching to the pion correlator from Eq. (4.1) then gives,

$$\begin{aligned} C_\pi^{\mathrm{PQ}}(\tau) &\equiv \frac{-1}{Z_{\mathrm{PQ}}} DUD\overline{Q}DQe^{-S_{\mathrm{PQ}}} \sum_{\vec{x}} \overline{u}_V \gamma_5 d_V(\vec{x},\tau)\overline{d}_V \gamma_5 u_V(0) \\ &= \frac{-1}{Z_{\mathrm{PQ}}} \int DU \prod_{j=1}^{N} \det(\not{D} + m_{Sj}) e^{-S_{\mathrm{gauge}}} \sum_{\vec{x}} \mathrm{tr}\left[\gamma_5 \left(\frac{1}{\not{D} + m_{Vd}}\right)_{x0} \gamma_5 \left(\frac{1}{\not{D} + m_{Vu}}\right)_{0x}\right], \end{aligned} \tag{4.9}$$

where the difference in sea and valence quark masses is now explicit. It is also useful to confirm that setting $m_S = m_V$ returns the QCD result for the pion correlator,

$$\begin{aligned} C_\pi^{\mathrm{PQ}}(\tau) =& \frac{-1}{Z_{\mathrm{PQ}}} \int DUD\overline{Q}DQe^{-S_{\mathrm{PQ}}} \sum_{\vec{x}} \overline{u}_V \gamma_5 d_V(\vec{x},\tau)\overline{d}_V \gamma_5 u_V(0) \\ =& \frac{-1}{Z_{\mathrm{PQ}}} \int DUD\overline{Q}DQe^{-S_{\mathrm{PQ}}} \sum_{\vec{x}} \overline{u}_S \gamma_5 d_S(\vec{x},\tau)\overline{d}_S \gamma_5 u_S(0) \\ =& \frac{-1}{Z_{\mathrm{PQ}}} \int DUD\overline{q}Dqe^{-S_{\mathrm{QCD}}} \sum_{\vec{x}} \overline{u}_S \gamma_5 d_S(\vec{x},\tau)\overline{d}_S \gamma_5 u_S(0) \\ =& C_\pi^{\mathrm{QCD}}(\tau). \end{aligned} \tag{4.10}$$

The second line follows since the propagators of the sea and valence quarks are the same when the quark masses are all equal.

4.2 $SU(4|2)$ Partially Quenched ChPT

It is evident from numerous lattice simulations of PQQCD that it exhibits qualitatively very similar behaviour to QCD at different energy scales. In particular, the pion correlation function from Eq. (4.1) behaves in PQQCD, at both the lower- and higher-energy scales, similarly to that in QCD. It has an exponential decay ($\sim \exp(-M_\pi)t$) at long-distance scales, and the pion mass in PQQCD obeys the GMOR relation (Eq. (3.29)), $m_\pi^2 \propto (m_{Vu} + m_{Vd})$, almost exactly [41]. Other indicators such as unphysical double poles arise only in exceptional conditions, barring which PQQCD has an analogous infrared (IR) or low-energy structure to that of QCD. There is thus a separation of energy scales exhibited in PQQCD, which is the primary condition for the construction of an EFT. In addition to the fact that QCD is a sub-theory of PQQCD, stringent Ward identities can be derived for PQQCD for different correlation functions. These conditions provide sufficient motivation for us to *assume* that a low-energy EFT of PQQCD exists, and proceed to detail its construction.

In order to formulate an EFT of PQQCD, we need to first elucidate the symmetries of Eq. (4.6). Perhaps the most obvious difference between PQQCD and QCD originates from the inclusion of the ghost quarks: PQQCD has a *graded* chiral symmetry, which is evident after chirally projecting the partially quenched quark vector Eq. (4.4), leading to invariance under transformations of the kind [44, 45],

$$\begin{aligned} Q_{L,R} &\longrightarrow U_{L,R} Q_{L,R}, \\ \overline{Q}_{L,R} &\longrightarrow \overline{Q}_{L,R} U_{L,R}^\dagger, \end{aligned} \tag{4.11}$$

with $U_{L,R} \in SU(N+M|M)$, the graded Lie group (Appendix C).

Thus, the PQQCD Lagrangian possesses a chiral $SU(N+M|M)_L \times SU(N+M|M)_R \times U(1)_V$ symmetry in the chiral limit ($\mathcal{M} = 0$). We thus expect a non-linear realisation of the graded chiral symmetry for the Nambu-Goldstone bosons arising from the assumed spontaneous symmetry breaking [45],

$$\begin{array}{c} SU(N+M|M)_R \times SU(N+M|M)_L \\ \downarrow \\ SU(N+M|M)_V. \end{array} \tag{4.12}$$

For our work, specifically, we require two additional quarks to be added to the original $SU(2)$ ChPT. We thus include two additional valence quarks, and hence two ghost quarks via Morel's trick above, leading to a graded, chiral group of $SU(4|2)$. We proceed to analogously define the fundamental degrees of freedom of partially quenched chiral perturbation theory (PQChPT) as in ChPT,

$$U = \exp\left\{\frac{2i}{F_0}\sum_{a=1}^{35}\phi^a T^a\right\}. \tag{4.13}$$

Following from the definition of the s(uper)trace (Eq. (B.8)) in Appendix B, we construct the effective Lagrangian according to the now-familiar rules from Chapter 3 - by creating building blocks that are invariant under the graded chiral symmetry group $SU(N+M|M)_V \times U(1)_V$ and ordering them according to the chiral power counting scheme. We, thus, obtain the leading order $SU(4|2)$ PQChPT Lagrangian,

$$\mathcal{L}^{(2)} = \frac{F^2}{4}\,\mathrm{Str}\left[\partial_\mu U^\dagger \partial^\mu U\right] + \frac{F^2}{2}\,\mathrm{Str}\left[\chi U^\dagger + U\chi^\dagger\right]. \tag{4.14}$$

It is immediately evident that this Lagrangian looks identical to the usual LO $SU(2)$ ChPT Lagrangian from Eq. (3.42). Here, in Eq. (4.14), we have suppressed the covariant derivative and included meson masses via the addition of the spurion field, χ. The mass matrix contained within is comprised of the quark masses of the sea, valence and ghost quarks,

$$\mathcal{M} = \mathrm{diag}(m_S, m_S, m_V, m_V, m_V, m_V). \tag{4.15}$$

For the rest of this work, it is sufficient to set all the quark masses to be degenerate, $m_S = m_V$. This also ensures that we easily recover the $SU(2)$ ChPT results from PQChPT.

The next-to-leading order Lagrangian follows via a similar procedure [46],

$$\begin{aligned}
\mathcal{L}^{(4)} =& L_0^{\mathrm{PQ}}\,\mathrm{Str}\left[\partial_\mu U^\dagger \partial_\nu U \partial^\mu U^\dagger \partial^\nu U\right] + (L_1^{\mathrm{PQ}} - \frac{1}{2}L_0^{\mathrm{PQ}})\,\mathrm{Str}\left[\partial_\mu U^\dagger \partial^\mu U\right]\mathrm{Str}\left[\partial_\nu U^\dagger \partial^\nu U\right] \\
&+ (L_2^{\mathrm{PQ}} - L_0^{\mathrm{PQ}})\,\mathrm{Str}\left[\partial_\mu U^\dagger (\partial_\nu U\right]\mathrm{Str}\left[\partial^\mu U^\dagger \partial^\nu U\right] \\
&+ (L_3^{\mathrm{PQ}} + 2L_0^{\mathrm{PQ}})\,\mathrm{Str}\left[\partial_\mu U^\dagger \partial_\nu U^\dagger \partial^\nu U\right] \\
&+ 2L_4^{\mathrm{PQ}}\,\mathrm{Str}\left[\partial_\mu U^\dagger \partial^\mu U\right]\mathrm{Str}\left[U^\dagger\chi + \chi^\dagger U\right] + 2L_5^{\mathrm{PQ}}\,\mathrm{Str}\left[\partial_\mu U^\dagger \partial^\mu U U^\dagger \chi + \chi^\dagger U\right] \\
&+ 4L_6^{\mathrm{PQ}}\left(\mathrm{Str}\left[U^\dagger\chi + \chi^\dagger U\right]\right)^2 + 4L_7^{\mathrm{PQ}}\left(\mathrm{Str}\left[U^\dagger\chi - \chi^\dagger U\right]\right)^2 \\
&+ 4L_8^{\mathrm{PQ}}\,\mathrm{Str}\left[\chi U^\dagger \chi U^\dagger + \chi^\dagger U \chi^\dagger U\right].
\end{aligned} \tag{4.16}$$

The low-energy constants (LECs) of this Lagrangian are denoted by a superscript PQ, to indicate that they are different from the *physical* LECs appearing in the NLO Lagrangian of physical ChPT, Eq. (3.50). The PQ LECs appearing here, however, are all the same as the LECs that appear in $SU(3)$ ChPT [37], since physical QCD (or ChPT) is contained within PQQCD (PQChPT) as a sub-theory. Any calculations in PQChPT involving *only* the physical mesons are dependent only on the physical LECs and return the results of physical ChPT. In comparison with the $SU(3)$ ChPT NLO Lagrangian, though, one glaring difference stands out - the terms with the coefficient L_0^{PQ}. These terms are eliminated from physical ChPT by virtue of the Cayley-Hamilton theorem, which was mentioned in the context of $SU(2)$ ChPT in Chapter 3. However, the Cayley-Hamilton theorem is invalid for matrices with dimension > 3, and the L_0^{PQ} LEC persists in the NLO $SU(4|2)$ PQChPT Lagrangian [47].

The physical LECs from Eq. (3.50) can be related to the unphysical LECs from Eq. (4.16) via the following well-known relations [33, 37]:

$$\begin{aligned} l_1 &\equiv 2(2L_1^{\mathrm{PQ}} + L_3^{\mathrm{PQ}}), \\ l_2 &\equiv 4L_2^{\mathrm{PQ}}, \\ l_3 &\equiv -4(2L_4^{\mathrm{PQ}} + L_5^{\mathrm{PQ}} - 4L_6^{\mathrm{PQ}} - 2L_8^{\mathrm{PQ}}), \\ l_4 &\equiv 4(2L_4^{\mathrm{PQ}} + L_5^{\mathrm{PQ}}), \\ l_7 &\equiv -8(2L_7^{\mathrm{PQ}} + L_8^{\mathrm{PQ}}). \end{aligned} \tag{4.17}$$

Thus, any calculation of physical observables, as mentioned, can be made dependent only on the physical LECs by using these LEC relations. The full set of independent LECs we shall use in our ensuing calculations are $\{l_1, l_2, l_3, l_4, l_7, L_0^{\mathrm{PQ}}, L_3^{\mathrm{PQ}}, L_5^{\mathrm{PQ}}, L_8^{\mathrm{PQ}}\}$. Unphysical outputs, hence, will naturally be dependent on the partially quenched LECs $\{L_0^{\mathrm{PQ}}, L_3^{\mathrm{PQ}}, L_5^{\mathrm{PQ}}, L_8^{\mathrm{PQ}}\}$, or linear combinations of them, and thus it is imperative to gain a precise knowledge of these LECs from experimental or lattice QCD data.

In order to demonstrate the validity of our statement that the physical, $SU(2)$ ChPT is contained within $SU(4|2)$ PQChPT as a sub-theory, we performed calculations of the mass, wavefunction and pion-decay constant renormalisation and the physical $\pi\pi$ scattering amplitude using only the $SU(2)$ quarks and their resulting mesons within Eq. (4.14) and Eq. (4.16). The results agree exactly with Eqs. (3.63), (3.64), (3.65) and (3.67) [1].

CHAPTER 5

Disconnected Contributions to $\pi\pi$ Scattering

Lattice quantum chromodynamics has been an immensely rewarding technique to calculate hadron properties from the first principles of QCD, wherein the QCD action is evaluated on a Euclidean spacetime lattice in a finite volume. It involves the direct evaluation of the QCD path integral and hence requires minimal input parameters to determine a large number of hadronic observables. The biggest drawback of lattice QCD is the dependence of the accuracy of its calculations on the lattice spacing (smaller is better) and lattice volume (larger is better). This means that systematic uncertainties are dependent on the available computational resources, since a greater number of simulations of the path integral on a lattice with smaller lattice spacing and larger volume would yield better resources. While great advancements in computational power have been made in the last few decades, certain processes require calculations that have been hampered due to limits on processing power and costs. One such important bugbear of lattice studies has been the calculation of *disconnected diagrams* in various hadronic processes.

Hadronic observables for a certain process are calculated in lattice QCD by evaluating n-point correlation functions with interpolating field operators corresponding to the external states of interest. In the case of pion-pion scattering, this correlation function is of the form

$$C_{\pi\pi\pi\pi}(t) = \left\langle \mathcal{O}_{\pi\pi}(t)\mathcal{O}'^{\dagger}_{\pi\pi}\left(t'\right)\right\rangle, \tag{5.1}$$

where the interpolating operator here is $\overline{q}\Gamma^i q(\boldsymbol{x},t)\overline{q}\Gamma^j q(\boldsymbol{y},t)$, with the quark fields comprised of the light quarks. The exponential decay of this correlation function, with the appropriate quantum numbers, will lead to the energy of the $\pi\pi$ state, which can then be related to the scattering length for the process via Lüscher equation. Numerous lattice studies have already explored different aspects of $\pi\pi$ scattering, to varying degrees of success [48–77]. There are broadly two ways in which the quark fields of these correlation functions can be Wick contracted. Any contraction diagrams that involve quark propagators beginning and ending at the same time slice or coordinates are known as disconnected diagrams, and all the others are known as connected diagrams. The computations of these diagrams on the lattice have proven to be difficult since the evaluated lattice signals are noisy and difficult to siphon.

It is important, then, to understand the qualitative and quantitative effects of these disconnected diagrams in different processes. In this work, we use effective field theoretical methods to provide a way to separate and understand the influence of these diagrams on lattice QCD results in pion-pion

scattering. The separation of connected and disconnected contributions of a physical, mesonic scattering processes is inherently unphysical, and this requires careful treatment and a modification of the usual EFT methods. Partial quenching of QCD allows us to deviate from the physical domain, and using PQChPT enables us to perform this unphysical separation of connected and disconnected diagrams in $\pi\pi$ scattering [1]. This procedure using EFTs was first carried out in [78], along with an analysis of the disconnected diagrams in the large-N_C limit for exotic mesons and was also employed in [79, 80] for other processes. It will be formalised here for mesonic scattering.

5.1 Classification of Diagrams in $\pi\pi$ Scattering

The aim of this section is to classify the connected and disconnected Wick contraction diagrams contributing to the scattering process $\pi(p_1)\pi(p_2) \to \pi(k_1)\pi(k_2)$. As mentioned in Section 3, we operate under the assumption of isospin symmetry ($m_u = m_d$), which means that only one independent amplitude is required to derive all isospin projected amplitudes, $\pi^+(p_1)\pi^-(p_2) \to \pi^0(k_1)\pi^0(k_2)$. Thus, using just the single amplitude $T(s,t,u)$ and crossing symmetry, the isospin-projected amplitudes are obtained. They are repeated here,

$$\begin{aligned} T^{I=0}(s,t,u) &= 3T(s,t,u) + T(t,s,u) + T(u,t,s), \\ T^{I=1}(s,t,u) &= T(t,s,u) - T(u,t,s), \\ T^{I=2}(s,t,u) &= T(t,s,u) + T(u,t,s). \end{aligned} \tag{5.2}$$

We can draw all the independent Wick contraction diagrams emanating from Eq. (5.1). The following points are pertinent:

- We are evaluating $\pi\pi$ scattering up to one loop (NLO). Each closed quark loop in a Wick contraction diagram corresponds to a flavour trace in the corresponding PQChPT Lagrangian. This implies that, drawing from the form of the NLO Lagrangian in Eq. (4.16), the relevant diagrams can have at most two quark loops up to NLO.
- Any diagram, such as Fig. 5.1, which contains a flavour-diagonal $\overline{q}q$ loop at the upper right vertex, vanishes when all the sea, valence and ghost quark masses are degenerate. The $SU(N|N_V)$ generators are straceless and a strace over such a loop in the isospin limit gives zero.

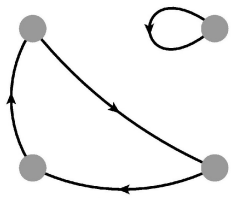

Figure 5.1: Any diagram that contains a flavour-diagonal loop vanishes due to the straceless $SU(N|N_V)$ generators in the isospin limit.

Given these constraints, there are only two independent Wick contracted quark propagator diagrams, shown in Fig. 5.2. These are labelled as $T_1(s,t,u)$ and $T_2(s,t,u)$ respectively. Setting $\pi^+ = u\overline{d}, \pi^- =$

$d\bar{u}, \pi^0 = (1/\sqrt{2})(u\bar{u} - d\bar{d})$, the full amplitude for the process $\pi^+(p_1)\pi^-(p_2) \to \pi^0(k_1)\pi^0(k_2)$ is written entirely in terms of $T_1(s,t,u)$ and $T_2(s,t,u)$ and their crossed amplitudes,

$$T(s,t,u) = T_1(s,t,u) + T_1(s,u,t) - T_1(u,t,s) + T_2(t,s,u). \tag{5.3}$$

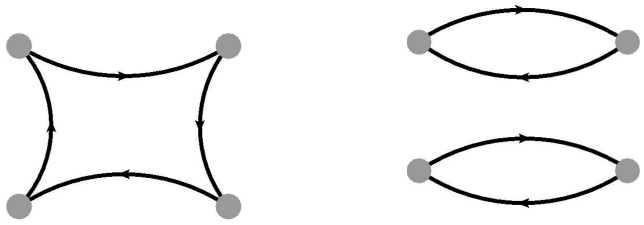

Figure 5.2: The Wick contraction diagrams contributing to the independent amplitudes $T_1(s,t,u)$ and $T_2(s,t,u)$ respectively.

The reason for our emphasis on $SU(4|2)$ PQChPT is now evident: a separation of the two diagrams in Fig. 5.2 requires an addition of two valence quarks to $SU(2)$ ChPT, and this in turn requires the addition of two ghost quarks to ensure that the determinants due to the valence quarks are cancelled in the generating functional. This also ensures that the number of dynamical degrees of freedom in the $SU(4|2)$ PQChPT matches the number in $SU(2)$ ChPT, which is two. Thus, we can now write the two independent amplitudes in terms of scattering of $SU(4|2)$ PQChPT mesons,

$$\begin{aligned} T_1(s,t,u) &= T_{(u\bar{d})(d\bar{j})\to(u\bar{k})(k\bar{j})}(s,t,u), \\ T_2(s,t,u) &= T_{(u\bar{d})(j\bar{k})\to(u\bar{d})(j\bar{k})}(s,t,u), \end{aligned} \tag{5.4}$$

In order to relate the separated Wick contracted quark diagrams to the various, physical isospin projected amplitudes evaluated on the lattice, we need to express all the different Wick contraction diagrams appearing in $\pi\pi$ scattering in terms of the amplitudes $T_1(s,t,u)$ and $T_2(s,t,u)$. According to lattice QCD nomenclature, they are classified as *connected*, *singly disconnected* and *doubly disconnected diagrams*.

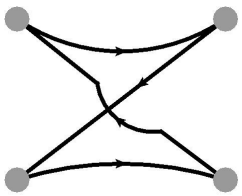

Figure 5.3: This diagram is connected and called 'Crossed' (C). It is represented by the amplitude $T_1(u,t,s)$.

The diagrams in Figs. 5.3 and 5.4 are connected diagrams, since they have both quark–anti-quark pairs propagating from the initial state to the final state, and have no quark propagators ending on the same time slice. In lattice QCD parlance [50], Fig. 5.3 is known as 'Crossed' (C), while the diagrams in Fig. 5.4 are called 'Direct' (D). While the former is given by $T_1(u,t,s)$, the latter are represented by $T_2(s,t,u)$ and $T_2(s,u,t)$ respectively.

Analogously, diagrams in Figs. 5.5 and 5.6 are the disconnected diagrams. Fig. 5.5 contains diagrams that are singly disconnected, where one quark–anti-quark pair propagates to the final state,

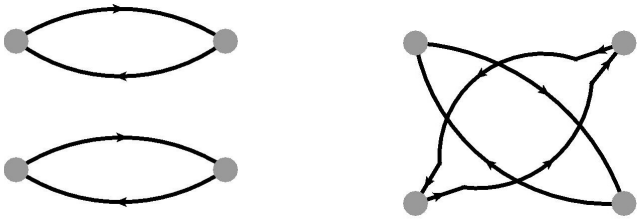

Figure 5.4: These two diagrams are both connected, and are known as 'Direct' (D). They are given by the amplitudes $T_2(s,t,u)$ and $T_2(s,u,t)$ respectively.

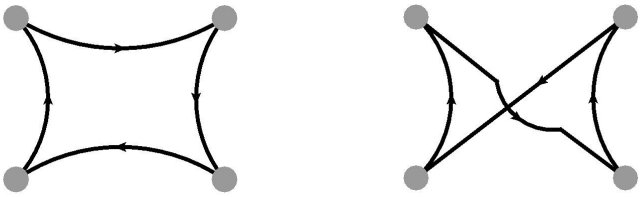

Figure 5.5: These diagrams are singly disconnected and are called 'Rectangular' (R). They are given by the amplitudes $T_1(s,t,u)$ and $T_1(s,u,t)$ respectively.

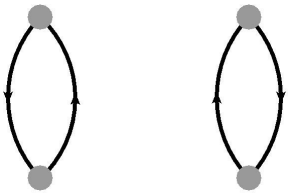

Figure 5.6: This diagram is the hardest to compute on the lattice since it is doubly disconnected. It is called the 'Vacuum' (V) diagram and is given by $T_1(u,t,s)$.

and they are called 'Rectangular' (R). The diagram in Fig. 5.6 is doubly disconnected, since both quark–anti-quark pairs begin and end on the same time slice, and is called the 'Vacuum' (V) diagram. The rectangular diagrams correspond to the amplitudes $T_1(s,t,u)$ and $T_1(s,u,t)$ respectively, and the vacuum diagram is given by the amplitude $T_2(t,s,u)$.

Combining Eq. (5.2) with the Wick contraction diagrams, the isospin projected amplitudes can be written in terms of the independent amplitudes $T_1(s,t,u)$ and $T_2(s,t,u)$ and their crossed amplitudes,

$$\begin{aligned}
T^{I=0}(s,t,u) &= \left[-T_1(u,t,s)\right] + \left[T_2(s,t,u) + T_2(s,u,t)\right] + \left[3\left(T_1(s,t,u) + T_1(s,u,t)\right)\right] + \left[3T_2(t,s,u)\right] \\
&\equiv T_C^{I=0}(s,t,u) + T_D^{I=0}(s,t,u) + T_R^{I=0}(s,t,u) + T_V^{I=0}(s,t,u), \\
T^{I=1}(s,t,u) &= \left[T_2(s,t,u) - T_2(s,u,t)\right] + \left[2\left(T_1(s,t,u) - T_1(s,u,t)\right)\right] \\
&\equiv T_D^{I=1}(s,t,u) + T_R^{I=1}(s,t,u), \\
T^{I=2}(s,t,u) &= \left[2T_1(u,t,s)\right] + \left[T_2(s,t,u) + T_2(s,u,t)\right] \\
&\equiv T_C^{I=2}(s,t,u) + T_D^{I=2}(s,t,u).
\end{aligned} \tag{5.5}$$

Here, the individual amplitude of each diagram has been defined as $\{T_X^I(s,t,u)\}(X = D,C,R,V)$.

Certain conclusions can already be made about the different connected and disconnected diagrams:

- It is clear that the $I = 0$ amplitude is the most difficult amplitude to evaluate on the lattice, since it contains contributions from the connected, singly disconnected and doubly disconnected diagrams. The lattice computations improve with increase in isospin, since the $I = 1$ amplitude has contributions from the connected and singly disconnected diagrams, and the $I = 2$ amplitude has contributions only from the connected diagram.
- As observed in [78], the contribution of the doubly disconnected vacuum (V) diagram is a purely NLO effect due to the two quark loop contractions, while the singly disconnected contributions are present at LO.
- Following from this, the $I = 0$ $\pi\pi$ scattering amplitude is more heavily dependent on the calculation of the singly disconnected diagram than the doubly disconnected diagram, and neglecting the latter in a lattice QCD computation would not cause a massive drop in accuracy since it is an NLO effect.
- However, for the $I = 1$ amplitude, the singly disconnected diagram contributes more substantially than the connected diagram, since the connected diagram here (direct D) has two quark loops and is an NLO effect.

5.2 Amplitudes of Connected and Disconnected Diagrams

We now evaluate the scattering amplitudes $T_1(s,t,u)$ and $T_2(s,t,u)$ in $SU(4|2)$ PQChPT:

$$\begin{aligned}
T_1(s,t,u) =& \frac{2M_\pi^2 - u}{2F_\pi^2} + \left(\frac{3u - 4M_\pi^2}{3F_\pi^2}\right)\mu_\pi + \left(\frac{2M_\pi^4 - 4M_\pi^2(s+t) + s(2s+t)}{12F_\pi^4}\right) J^r_{\pi\pi}(s) \\
&+ \left(\frac{2M_\pi^4 - 4M_\pi^2(s+t) + t(2t+s)}{12F_\pi^4}\right) J^r_{\pi\pi}(t) + \frac{4}{F_\pi^4}\left(s^2 + t^2 + u^2 - 4M_\pi^4\right) L_0^{\mathrm{PQ},r} \\
&+ \frac{2}{F_\pi^4}\left(4M_\pi^2 u + s^2 + t^2 - 8M_\pi^4\right) L_3^{\mathrm{PQ},r} - \frac{4M_\pi^2 u}{F_\pi^4} L_5^{\mathrm{PQ},r} + \frac{16M_\pi^4}{F_\pi^4} L_8^{\mathrm{PQ},r} \\
&- \frac{M_\pi^4}{72\pi^2 F_\pi^4} + \frac{M_\pi^2 u}{96\pi^2 F_\pi^4} + \frac{2u^2 - s^2 - t^2}{576\pi^2 F_\pi^4},
\end{aligned} \tag{5.6}$$

$$\begin{aligned}
T_2(s,t,u) =& \frac{(s-2M_\pi)^2}{4F_\pi^4} J^r_{\pi\pi}(s) + \frac{(u-2M_\pi)^2}{4F_\pi^4} J^r_{\pi\pi}(u) + \left(\frac{2M_\pi^4 + t^2}{4F_\pi^4}\right) J^r_{\pi\pi}(t) \\
&+ \frac{4}{F_\pi^4}\left(4M_\pi^4 - s^2 - t^2 - u^2\right) L_0^{\mathrm{PQ},r} + \frac{2}{F_\pi^4}\left(t - 2M_\pi^2\right)^2 \left(l_1^r - 2L_3^{\mathrm{PQ},r}\right) \\
&+ \frac{1}{F_\pi^4}\left(s^2 + u^2 + 4M_\pi^2 t - 8M_\pi^4\right) l_2^r + \frac{2M_\pi^2}{F_\pi^4}\left(t - 2M_\pi^2\right)\left(l_4^r - 4L_5^{\mathrm{PQ},r}\right) \\
&+ \frac{2M_\pi^4}{F_\pi^4}\left(l_3^r + l_4^r - 8L_8^{\mathrm{PQ},r}\right),
\end{aligned} \tag{5.7}$$

i	0	1	2	3	4	5	6	7	8
Γ_i	$\frac{1}{24}$	$\frac{1}{12}$	$\frac{1}{6}$	0	$\frac{1}{8}$	$\frac{1}{4}$	$\frac{3}{32}$	0	0

Table 5.1: Coefficients of the UV divergence in the SU(4|2) PQChPT.

where the following quantities have been defined,

- The ultraviolet (UV) divergences and chiral logarithms, as in $SU(2)$ ChPT in Chapter 3, are contained in

$$\begin{aligned} \lambda &\equiv -\frac{1}{32\pi^2}\left(\frac{2}{4-d} + \ln 4\pi - \gamma + 1\right), \\ \mu_\pi &\equiv -\frac{M_\pi^2}{32\pi^2 F_\pi^2}\ln\frac{\mu^2}{M_\pi^2}. \end{aligned} \tag{5.8}$$

- The Passarino-Veltman two-point function [81],

$$B_0(p^2, m_1^2, m_2^2) \equiv \frac{(2\pi)^{4-d}}{i\pi^2}\int d^d k \frac{1}{(k^2 - m_1^2 + i\varepsilon)((k+p)^2 - m_2^2 + i\varepsilon)}, \tag{5.9}$$

  which has a simplified version due to the presence of just one mass M_π in this work:

$$J_{\pi\pi}(p^2) \equiv \frac{1}{16\pi^2} B_0\left(p^2, M_\pi^2, M_\pi^2\right). \tag{5.10}$$

  We can separate the finite and infinite parts of $J_{\pi\pi}(p^2)$,

$$J_{\pi\pi}\left(p^2\right) = -2\lambda + J_{\pi\pi}^r\left(p^2\right). \tag{5.11}$$

- The renormalised $SU(4|2)$ PQChPT LECs are defined via the bare LECs appearing in the Lagrangian Eq. (4.16),

$$L_i^{\mathrm{PQ}} = L_i^{\mathrm{PQ},r} + \lambda\Gamma_i, \tag{5.12}$$

  where the coefficients Γ_i are given in Table 5.1. The physical $SU(2)$ ChPT LECs are defined here, again, in terms of their scale-independent counterparts (Chapter 3),

$$l_i^r = \gamma_i\left(\frac{\bar{l}_i}{32\pi^2} + \frac{F_\pi^2}{M_\pi^2}\mu_\pi\right), \tag{5.13}$$

  for i=1,...,4 only, and $\gamma_1 = 1/3, \gamma_2 = 2/3, \gamma_3 = -1/2$ and $\gamma_4 = 2$.

The amplitudes $T_1(s,t,u)$ and $T_2(s,t,u)$ warrant a few observations,

- Both the amplitudes are finite and scale-independent.
- $T_1(s,t,u)$, as evident from Fig. 5.5, has a LO, $O(p^2)$ contribution, while $T_2(s,t,u)$, due to its two closed quark loops (Fig. 5.4), has only an NLO $O(p^4)$ contribution.
- $T_1(s,t,u)$ is symmetrical under $s \leftrightarrow t$ and $T_2(s,t,u)$ is symmetrical under $s \leftrightarrow u$.

- A crucial observation is that both the amplitudes have an explicit dependence on the unphysical PQChPT LECs. This indicates that the separation of Wick contractions into connected and disconnected diagrams is an intrinsically unphysical or artificial process.

5.2.1 Partial Wave Amplitudes

We now proceed to project the amplitudes for different Wick contraction diagrams into their partial waves:

$$T_X^{Il}(s) \equiv \frac{1}{64\pi}\int_{-1}^{+1} T_X^I(s,t(s,\cos\theta),u(s,\cos\theta))P_l(\cos\theta)\,d\cos\theta, \tag{5.14}$$

where $X = D, C, R, V$ stands for the different diagrams and $P_l(x)$ is the Legendre polynomial. It is convenient to express the imaginary parts of the different partial waves in the physical region, $s \geq 4M_\pi^2$, since they are independent of LECs and constitute direct PQChPT predictions at one loop order. The partial waves with imaginary parts that do not vanish are,

$$\begin{aligned}
\operatorname{Im} T_D^{00}(s) &= \frac{\left(s-2M_\pi^2\right)^2}{64\pi F_\pi^4}\operatorname{Im} J_{\pi\pi}^r(s),\\
\operatorname{Im} T_R^{00}(s) &= \frac{3\left(s^2-4M_\pi^4\right)}{128\pi F_\pi^4}\operatorname{Im} J_{\pi\pi}^r(s),\\
\operatorname{Im} T_V^{00}(s) &= \frac{3\left(s^2+2M_\pi^4\right)}{128\pi F_\pi^4}\operatorname{Im} J_{\pi\pi}^r(s),\\
\operatorname{Im} T_R^{11}(s) &= \frac{\left(s-4M_\pi^2\right)^2}{576\pi F_\pi^4}\operatorname{Im} J_{\pi\pi}^r(s),\\
\operatorname{Im} T_D^{20}(s) &= \frac{\left(s-2M_\pi^2\right)^2}{64\pi F_\pi^4}\operatorname{Im} J_{\pi\pi}^r(s),
\end{aligned} \tag{5.15}$$

with the imaginary part of the loop function,

$$\operatorname{Im} J_{\pi\pi}^r(s) = \Theta(s-4M_\pi^2)\frac{1}{16\pi}\sqrt{\frac{s-4M_\pi^2}{s}}. \tag{5.16}$$

The physical $\pi\pi$ scattering partial wave and isospin projected amplitudes obey the single-channel perturbative unitarity relation,

$$\operatorname{Im} T_{\rm NLO}^{Il}(s) = \frac{2|\vec{p}|}{\sqrt{s}}\left|T_{\rm LO}^{Il}(s)\right|^2, \tag{5.17}$$

where $|\vec{p}|$ is the centre-of-mass momentum. However, the same amplitudes for a particular Wick contraction diagram do not satisfy similar single-channel relations since they cannot have specific

isospins. This means that they do satisfy a multi-channel perturbative unitarity condition,

$$\mathrm{Im}\, T^{l}_{\mathrm{NLO},ab\to cd}(s) = \sum_{e,f} \alpha_{ef} \frac{2|\vec{p}|}{\sqrt{s}} T^{l}_{\mathrm{LO},ef\to cd}(s) T^{l*}_{\mathrm{LO},ab\to ef}(s), \tag{5.18}$$

where $\alpha_{ef} = 1(2)$ if e and f are (are not) identical particles.

5.3 Predictions of Scattering Lengths

In order to compare our results with lattice data for the different contractions, we need to derive the scattering lengths for each type of diagram, which can then be related to the lattice studies via Lüscher equation (Chapter 6). The scattering lengths are evaluated via the partial wave projected amplitudes,

$$a^{Il}_{X} = \lim_{q^2\to 0} \frac{\mathrm{Re}\, T^{Il}_{X}\left(4M_\pi^2 + 4q^2\right)}{(q^2)^l}, \tag{5.19}$$

where the Mandelstam variable s, near the threshold, has been replaced by $(4M_\pi^2 + 4q^2)$. Thus, combining isospin projection (Eq. (5.5)) and the amplitudes from Eqs. (5.6) and (5.7), we can calculate the scattering length contributions for each individual Wick contraction diagram X. The results for the $l = 0, 1, 2$ scattering lengths for each contraction X are listed below.

$I = 0, l = 0$:

$$\begin{aligned}
a^{00}_{D} =& -\frac{M_\pi^2}{8\pi F_\pi^2}\left[\mu_\pi + \frac{M_\pi^2}{F_\pi^2}\left(-\frac{\bar{l}_1}{24\pi^2} - \frac{\bar{l}_2}{12\pi^2} + \frac{\bar{l}_3}{64\pi^2} + \frac{\bar{l}_4}{16\pi^2} + 24L_0^{\mathrm{PQ,r}} + 8L_3^{\mathrm{PQ,r}} - 8L_5^{\mathrm{PQ,r}}\right.\right.\\
&\left.\left. +8L_8^{\mathrm{PQ,r}} + \frac{1}{64\pi^2}\right)\right],\\
a^{00}_{C} =& \frac{M_\pi^2}{32\pi F_\pi^2}\left[1 - 2\mu_\pi + \frac{M_\pi^2}{F_\pi^2}\left(-48L_0^{\mathrm{PQ,r}} - 16L_3^{\mathrm{PQ,r}} + 16L_5^{\mathrm{PQ,r}} - 16L_8^{\mathrm{PQ,r}} - \frac{1}{16\pi^2}\right)\right],\\
a^{00}_{R} =& \frac{3M_\pi^2}{16\pi F_\pi^2}\left[1 - 2\mu_\pi + \frac{M_\pi^2}{F_\pi^2}\left(48L_0^{\mathrm{PQ,r}} + 16L_3^{\mathrm{PQ,r}} + 16L_8^{\mathrm{PQ,r}} + \frac{1}{8\pi^2}\right)\right],\\
a^{00}_{V} =& \frac{9M_\pi^2}{16\pi F_\pi^2}\left[\mu_\pi + \frac{M_\pi^2}{F_\pi^2}\left(\frac{\bar{l}_1}{72\pi^2} + \frac{\bar{l}_2}{36\pi^2} - \frac{\bar{l}_3}{192\pi^2} + \frac{\bar{l}_4}{16\pi^2} - 8L_0^{\mathrm{PQ,r}} - \frac{8L_3^{\mathrm{PQ,r}}}{3} - \frac{8L_5^{\mathrm{PQ,r}}}{3}\right.\right.\\
&\left.\left. -\frac{8L_8^{\mathrm{PQ,r}}}{3} + \frac{5}{192\pi^2}\right)\right].
\end{aligned} \tag{5.20}$$

$I = 2, l = 0$:

$$\begin{aligned} a_D^{20} &= a_D^{00}, \\ a_C^{20} &= -2a_C^{00}, \\ a_{\text{tot}}^{20} &= -\frac{M_\pi^2}{16\pi F_\pi^2}\left[1 + \frac{M_\pi^2}{\pi^2 F_\pi^2}\left(-\frac{\bar{l}_1}{12} - \frac{\bar{l}_2}{6} + \frac{\bar{l}_3}{32} + \frac{\bar{l}_4}{8} - \frac{1}{32}\right)\right]. \end{aligned} \tag{5.21}$$

$I = 1, l = 1$:

$$\begin{aligned} a_D^{11} &= \frac{1}{12\pi F_\pi^2}\left[\mu_\pi + \frac{M_\pi^2}{F_\pi^2}\left(-\frac{\bar{l}_1}{24\pi^2} + \frac{\bar{l}_2}{24\pi^2} + \frac{\bar{l}_4}{16\pi^2} + 8L_3^{\text{PQ,r}} - 4L_5^{\text{PQ,r}} - \frac{13}{384\pi^2}\right)\right], \\ a_R^{11} &= \frac{1}{24\pi F_\pi^2}\left[1 - 2\mu_\pi + \frac{M_\pi^2}{F_\pi^2}\left(-16L_3^{\text{PQ,r}} + 8L_5^{\text{PQ,r}} - \frac{13}{288\pi^2}\right)\right]. \end{aligned} \tag{5.22}$$

$I = 0, l = 2$:

$$\begin{aligned} a_D^{02} &= \frac{1}{90\pi F_\pi^4}\left[\frac{F_\pi^2}{M_\pi^2}\mu_\pi + \frac{\bar{l}_1}{16\pi^2} + \frac{\bar{l}_2}{16\pi^2} - 24\pi^2 L_0^{\text{PQ,r}} - 12\pi^2 L_3^{\text{PQ,r}} - \frac{77}{640\pi^2}\right], \\ a_C^{02} &= \frac{1}{180\pi F_\pi^4}\left[\frac{F_\pi^2}{M_\pi^2}\mu_\pi - 24\pi^2 L_0^{\text{PQ,r}} - 12\pi^2 L_3^{\text{PQ,r}} + \frac{13}{320\pi^2}\right], \\ a_R^{02} &= \frac{1}{30\pi F_\pi^4}\left[-\frac{F_\pi^2}{M_\pi^2}\mu_\pi + 24L_0^{\text{PQ,r}} + 6L_3^{\text{PQ,r}} - \frac{57}{1920\pi^2}\right], \\ a_V^{02} &= \frac{1}{60\pi F_\pi^4}\left[\frac{F_\pi^2}{M_\pi^2}\mu_\pi + \frac{\bar{l}_2}{8\pi^2} - 24L_0^{\text{PQ,r}} - \frac{3}{20\pi^2}\right]. \end{aligned} \tag{5.23}$$

$I = 2, l = 2$:

$$\begin{aligned} a_D^{22} &= a_D^{02}, \\ a_C^{22} &= -2a_C^{02}. \end{aligned} \tag{5.24}$$

These expressions are specific predictions of $SU(4|2)$ PQChPT for the different connected and disconnected diagrams of $\pi\pi$ scattering. However, some of the a_X^{Il} are dependent on LECs such as $\bar{l}_3$, L_0^{PQ} and L_3^{PQ}, which are riddled with very large uncertainties (Table 5.2) [82–84]. The fitting of these scattering lengths to data would thus be problematic, and we circumvent this issue by creating linear combinations of the a_X^{Il} that are dependent only on the LECs that are known more precisely. These

LECs	Values
$\bar{l}_1$	−0.4(6)
$\bar{l}_2$	4.3(1)
$\bar{l}_3$	3.0(8)
$\bar{l}_4$	4.4(2)
$10^3 L_0^{\mathrm{PQ},r}$	1.0(1.1)
$10^3(L_3^{\mathrm{PQ},r} + 2L_0^{\mathrm{PQ},r})$	−1.56(87)
$10^3 L_5^{\mathrm{PQ},r}$	0.501(43)
$10^3 L_8^{\mathrm{PQ},r}$	0.581(22)

Table 5.2: The LECs used in this analysis: the values of $\{\bar{l}_i\}$ are obtained from [82] and [83], while the PQ LEC values of $\{L_5^{\mathrm{PQ,r}}, L_8^{\mathrm{PQ,r}}\}$ and $\{L_0^{\mathrm{PQ,r}}, L_3^{\mathrm{PQ,r}}\}$ are obtained from the NLO and NNLO fits to lattice data, respectively, in [84] at $\mu = 1$ GeV.

combinations are:

$$\begin{aligned}
a_V^{00} - \frac{3}{2}a_D^{00} &= \frac{M_\pi^4}{\pi F_\pi^4}\left[\frac{3\bar{l}_4}{64\pi^2} - 3L_5^{\mathrm{PQ,r}} + \frac{9}{512\pi^2} + \frac{3F_\pi^2}{4M_\pi^2}\mu_\pi\right], \\
a_R^{00} + 6a_C^{00} - \frac{3M_\pi^2}{8\pi F_\pi^2} &= \frac{M_\pi^4}{\pi F_\pi^4}\left[3L_5^{\mathrm{PQ,r}} + \frac{3}{256\pi^2} - \frac{3F_\pi^2}{4M_\pi^2}\mu_\pi\right], \\
M_\pi^2 a_R^{11} + \frac{8}{3}a_C^{00} - 30M_\pi^4 a_C^{02} - \frac{M_\pi^2}{8\pi F_\pi^2} &= \frac{M_\pi^4}{\pi F_\pi^4}\left[\frac{5L_5^{\mathrm{PQ,r}}}{3} - \frac{4L_8^{\mathrm{PQ,r}}}{34560\pi^2} - \frac{5F_\pi^2}{12M_\pi^2}\mu_\pi\right], \\
M_\pi^4 a_R^{02} - 3M_\pi^4 a_C^{02} + \frac{4}{5}a_C^{00} - \frac{M_\pi^2}{40\pi F_\pi^2} &= \frac{M_\pi^4}{\pi F_\pi^4}\left[\frac{2L_5^{\mathrm{PQ,r}}}{5} - \frac{2L_8^{\mathrm{PQ,r}}}{5} - \frac{31}{9600\pi^2} - \frac{F_\pi^2}{10M_\pi^2}\mu_\pi\right].
\end{aligned} \tag{5.25}$$

These linear combinations are also constructed such that the LO ($O(p^2)$) contributions are subtracted, so that there is no suppression due to trivial power counting. On the lattice, the connected diagrams are computed most accurately, and their contributions a_D and a_C are related to the trickier diagrams (constituting the scattering lengths a_R and a_V) in the above expressions. Thus, these relations can be used to gauge the accuracy of lattice contributions via comparison of the better- and lesser-known components of $\pi\pi$ scattering.

We also list the total, physical scattering lengths $a_{\mathrm{tot}}^{Il} = \sum_X a_X^{Il}$ for each partial wave:

$I = 0, l = 0$:

$$a_{\mathrm{tot}}^{00} = \frac{7M_\pi^2}{32\pi F_\pi^2}\left[1 + \frac{M_\pi^2}{\pi^2 F_\pi^2}\left(\frac{5\bar{l}_1}{84} + \frac{5\bar{l}_2}{42} - \frac{5\bar{l}_3}{224} + \frac{\bar{l}_4}{8} + \frac{5}{32}\right)\right]. \tag{5.26}$$

$I = 2, l = 0$:

$$a_{\mathrm{tot}}^{20} = -\frac{M_\pi^2}{16\pi F_\pi^2}\left[1 + \frac{M_\pi^2}{\pi^2 F_\pi^2}\left(-\frac{\bar{l}_1}{12} - \frac{\bar{l}_2}{6} + \frac{\bar{l}_3}{32} + \frac{\bar{l}_4}{8} - \frac{1}{32}\right)\right]. \tag{5.27}$$

$I = 1, l = 1$:

$$a_{\text{tot}}^{11} = \frac{1}{24\pi F_\pi^2}\left[1 + \frac{M_\pi^2}{\pi^2 F_\pi^2}\left(-\frac{\bar{l}_1}{12} + \frac{\bar{l}_2}{12} + \frac{\bar{l}_4}{8} - \frac{65}{576}\right)\right]. \tag{5.28}$$

$I = 0, l = 2$:

$$a_{\text{tot}}^{02} = \frac{1}{1440\pi^3 F_\pi^4}\left[\bar{l}_1 + 4\bar{l}_2 - \frac{53}{8}\right]. \tag{5.29}$$

$I = 2, l = 2$:

$$a_{\text{tot}}^{22} = \frac{1}{1440\pi^3 F_\pi^4}\left[\bar{l}_1 + \bar{l}_2 - \frac{103}{40}\right]. \tag{5.30}$$

The total scattering lengths correspond to those in [33]. The unphysical PQChPT LECs cancel out in these expressions and hence they are only dependent on the physical, $SU(2)$ LECs. These expressions thus serve as a verification of the validity of our computation.

5.4 Numerical Results

We now proceed to provide quantitative predictions of the scattering lengths of the different connected and disconnected diagrams. This requires the insertion of the numerical values of the LECs involved. Since our expressions require both the physical and unphysical LECs, these values have been included from estimations from a variety of experimental and lattice data.

- $\bar{l}_1$, $\bar{l}_2$ and $\bar{l}_4$ are physical LECs that are well-known from analysis of $\pi\pi$ scattering data [82]. However, $\bar{l}_3$ in [82] has a much larger uncertainty, which has since been reduced by the incorporation of lattice data [83]. Thus, for the physical LECs, we use the scale-independent LEC values from [84] that combines experimental data and lattice calculations.

- The unphysical LECs were estimated from lattice results fitted to the pion mass and pion-decay constant calculated from $N_f = 2 + 1$ domain wall QCD at NLO and next-to-next-to-leading order (NNLO) PQChPT, including finite volume corrections due to NLO, by the RBC-UKQCD Collaboration [84]. The collaboration used partially quenched QCD, by separately varying the sea and valence quark masses on the lattice, and matched with PQChPT results to perform the required fits. The $L_5^{\text{PQ,r}}$ and $L_8^{\text{PQ,r}}$ LECs were fitted to a reasonable precision (Table 5.2) at NLO, but $L_0^{\text{PQ,r}}$ and $L_3^{\text{PQ,r}}$ were obtained only by a NNLO fit since the NLO mass and decay constant are independent of these LECs. They thus have a larger uncertainty than the other quantities involved in our expressions.

- We choose the renormalisation scale to be $\mu = 1$ GeV. The results for the LECs obtained in [84] used two different mass cuts for the heaviest unitary pion included in their fits: 370 MeV and 450 MeV. We chose the latter value of 450 MeV, since the experimental values of the physical LECs $\bar{l}_i$ were reproduced to a higher accuracy with this cut.

	$10^2 a_X^{00}$	$10^2 a_X^{20}$	$10^2 M_\pi^2 a_X^{11}$	$10^4 M_\pi^4 a_X^{02}$	$10^4 M_\pi^4 a_X^{22}$
D	0.35 ± 0.24	0.35 ± 0.24	0.02 ± 0.26	3.5 ± 2.0	3.5 ± 2.0
C	2.41 ± 0.12	-4.81 ± 0.23	0	0.95 ± 0.96	-1.9 ± 1.9
R	14.8 ± 0.7	0	3.59 ± 0.26	6.7 ± 7.8	0
V	2.48 ± 0.38	0	0	0.8 ± 7.3	0
Total	20.0 ± 0.2	-4.46 ± 0.07	3.61 ± 0.04	11.9 ± 0.8	1.54 ± 0.71

Table 5.3: PQChPT predictions of the scattering lengths of each type of contraction diagram.

We provide the PQChPT predictions of the different scattering lengths a_X^{Il} in Table 5.3. The uncertainties of the LECs from Table 5.2 are the only contributing errors, and our final uncertainties were determined by an error formula that uses uncorrelated LEC errors and combined in a quadrature. Clearly, the poorly estimated LECs $\bar{l}_3$, $L_0^{\mathrm{PQ,r}}$ and $L_3^{\mathrm{PQ,r}}$ contribute to the large uncertainty of each of the scattering lengths. As designed, the values of the linear combinations of the scattering lengths given in Eq. (5.25) are much more precise,

$$\begin{aligned}
a_V^{00} - \frac{3}{2} a_D^{00} &= (1.96 \pm 0.16) \times 10^{-2}, \\
a_R^{00} + 6 a_C^{00} - \frac{3 M_\pi^2}{8\pi F_\pi^2} &= (2.00 \pm 0.02) \times 10^{-2}, \\
M_\pi^2 a_R^{11} + \frac{8}{3} a_C^{00} - 30 M_\pi^4 a_C^{02} - \frac{M_\pi^2}{8\pi F_\pi^2} &= (6.38 \pm 0.13) \times 10^{-3}, \\
M_\pi^4 a_R^{02} - 3 M_\pi^4 a_C^{02} + \frac{4}{5} a_C^{00} - \frac{M_\pi^2}{40\pi F_\pi^2} &= (1.47 \pm 0.03) \times 10^{-3}, \\
M_\pi^4 a_V^{02} + 6 M_\pi^4 a_C^{02} - \frac{4}{5} a_C^{00} + \frac{M_\pi^2}{40\pi F_\pi^2} &= (-4.39 \pm 0.47) \times 10^{-4}.
\end{aligned} \tag{5.31}$$

The numerical results in Eq. (5.31) serve a two-fold purpose. Firstly, the various linear combinations of the connected and disconnected contributions can be directly checked with lattice results to estimate the accuracy of lattice calculations of these diagrams. Secondly, since the connected contributions can be computed on the lattice rather precisely, a better estimate of the unphysical LECs $L_0^{\mathrm{PQ,r}}$ and $L_3^{\mathrm{PQ,r}}$ can be gleaned via NLO fits of the a_D^{Il} and a_C^{Il} from Eq. (5.25). This is especially relevant because these LECs, as mentioned, do not appear in the expressions of the NLO corrections to the pion mass and pion-decay constant. Such an improved evaluation of the unphysical LECs will be beneficial to any mesonic PQChPT studies at NLO, and particularly improve the accuracy of observables involved in $\pi\pi$ scattering and disconnected contributions to this process.

It is also insightful to examine the full energy (s) dependence of the partial waves evaluated in Section 5.2.1. Unlike for the case of scattering lengths, there is no simple linear combination of partial wave amplitudes that eliminates their dependence on the LECs $\bar{l}_3$, $L_0^{\mathrm{PQ,r}}$ and $L_3^{\mathrm{PQ,r}}$, which also rise with increasing s. However, it is useful to present the imaginary parts of these partial wave amplitudes, since, as mentioned, they do not depend on the LECs (Fig. 5.7). In the physical region, it is evident that the imaginary part of the $I = 0$ amplitude receives contributions from the direct (D), rectangular (R) as well as the vacuum (V) diagrams. The imaginary parts of the $I = 1$ and the $I = 2$ in the physical

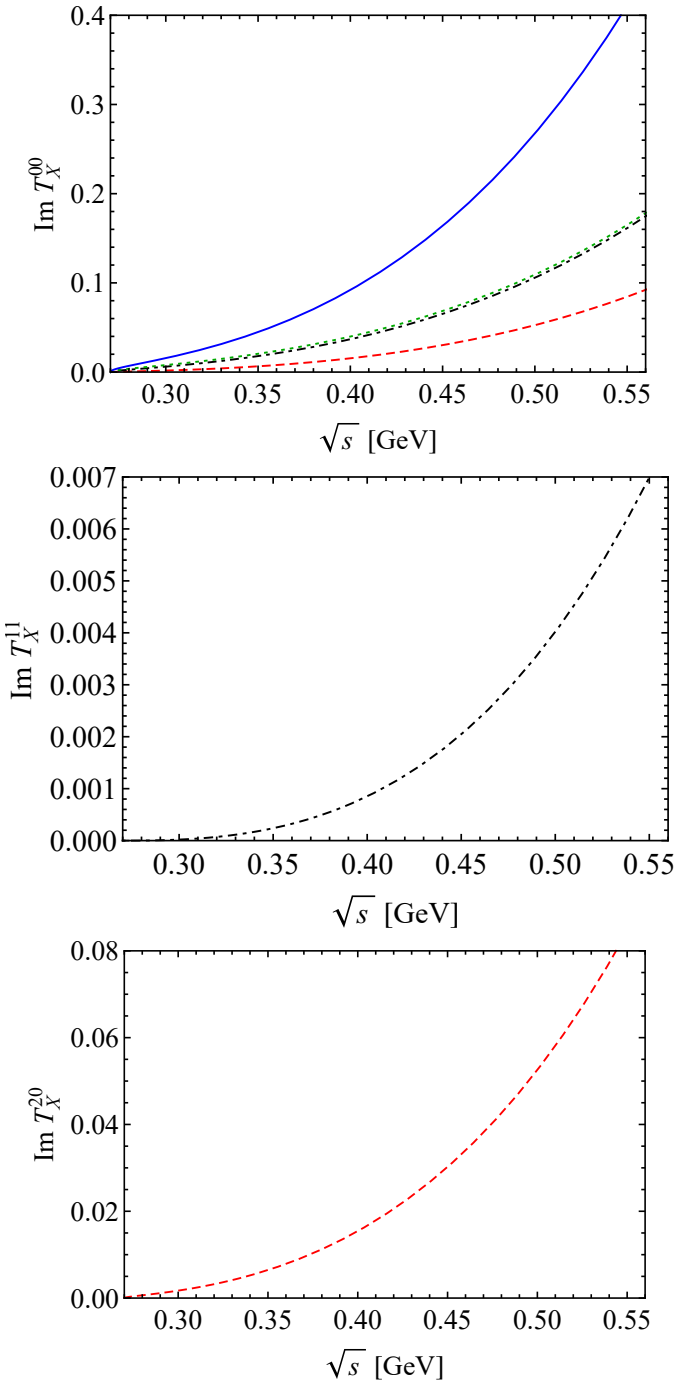

Figure 5.7: The imaginary parts of the direct (red, dashed), rectangular (black, dash-dotted), vacuum (green, dotted) and total (blue, solid, for T^{00} only) contributions to the isospin and partial wave projected amplitudes T^{00}, T^{11} and T^{20}.

region receive contributions from only the rectangular (R) and the direct (D) diagrams respectively.

5.5 Summary

The efforts of this chapter were aimed towards a more coherent, concerted understanding of $\pi\pi$ scattering from the interplay between effective field theoretical methods and lattice QCD. Certain specific suggestions of how the quantitative results of this chapter may be utilised by lattice QCD studies to, for example, better nail down the poorly known LECs $\bar{l}_3$, $L_0^{\mathrm{PQ,r}}$ and $L_3^{\mathrm{PQ,r}}$ have already been mentioned. A better understanding of these LECs, needless to say, will have far-reaching consequences in our overall understanding of mesonic scattering processes, both theoretically and on the lattice. We would also like to mention the possibility of lattice studies determining the scattering lengths for the individual connected and disconnected contractions directly. This would lead the way to joint EFT and lattice studies to calculate the relevant observables involving disconnected diagrams, which would prove to be more economical and efficient than current methods. For example, such an effort would entail the precise estimation of the unphysical LECs $L_0^{\mathrm{PQ,r}}$ and $L_3^{\mathrm{PQ,r}}$ from lattice calculations of the connected contributions fitted to our formulae at NLO, and then a feedback of these now-precise LECs into our EFT-derived expressions to quantitatively clarify the exact size of disconnected contributions to various processes and amplitudes.

CHAPTER 6

Constraints on Disconnected Contributions in $\pi\pi$ Scattering

We concluded the previous chapter by noting how our analytical and numerical results of the scattering lengths of the different connected and disconnected diagrams may be used to compare and guide lattice QCD studies of $\pi\pi$ scattering. In particular, it was shown how certain linear combinations of the individual scattering lengths were dependent only on well known LECs, and these could be directly contrasted with lattice QCD results to ensure that the lattice studies were evaluating different diagrams accurately. However, such a comparison faces an important barrier - lattice QCD simulations are performed in finite volume to derive discrete energy levels, whereas our effective field theory results were derived in infinite volume. We thus need to extend our partially quenched chiral perturbation theory formalism of separating connected and disconnected diagrams to include finite volume effects. The standard method used to relate infinite volume scattering lengths to the lattice QCD evaluated finite volume energy levels is Lüscher's formalism.

6.1 Single-Channel Lüscher equation

We have already derived the essential mechanism to isolate the disconnected Wick contractions from the full $\pi\pi$ scattering amplitude for different isospins and partial waves by implementing PQChPT in infinite volume. Lüscher developed a method to relate physical observables such as scattering lengths of a process to their finite volume counterparts - which, in lattice QCD are discrete energy levels of different correlation functions [85, 86].

To see this explicitly, we begin with the expression for the centre-of-mass (CM) momentum expressed in terms of the CM energy, $E = \sqrt{s}$, using the Källén function, $\lambda(x, y, z) = x^2+y^2+z^2-2xy-2yz-2zx$, as [87],

$$p_a = \frac{\lambda^{1/2}(E^2, m_{a1}^2, m_{a2}^2)}{2E}. \tag{6.1}$$

For the case of a single-channel scattering process, the scattering amplitude may be expanded in terms of its partial wave amplitudes,

$$T(s,t,u) = \sum_{l=0}^{\infty}(2l+1)T_l(E)P_l(\cos\theta), \tag{6.2}$$

where the $\{T_l(E)\}$ are the partial wave amplitudes with angular momentum l, $P_l(\cos\theta)$ are the Legendre polynomials and θ is the scattering angle. This definition of the partial wave amplitudes differs from Eq. (5.14) by a normalisation factor of 32π. Subject to this normalisation factor, we have already mentioned that the partial wave amplitudes in a single channel obey the following unitarity condition:

$$\operatorname{Im} T_l(E) = \Theta\left(E - m_1 - m_2\right) \frac{p}{8\pi E} \left|T_l(E)\right|^2 . \tag{6.3}$$

This condition allows us to parameterise the single-channel partial wave amplitudes as,

$$T_l(E) = \frac{8\pi E}{p \cot \delta_l(E) - ip}, \tag{6.4}$$

where $\delta_l(E)$ are the respective phase shifts. Since we are working in degenerate PQChPT, we shall choose $m_1 = m_2 = M_\pi$, leading to a more simplified derivation and $p = \sqrt{E^2 - 4M_\pi^2}/2$.

Until now, we have been working with dimensional regularisation to regularise UV-divergent integrals. The s-channel two-point scalar loop function $G(E)$, in the CM frame, is defined as,

$$G(E) = i \int \frac{d^4q}{(2\pi)^4} \frac{1}{(q^2 - M_\pi^2 + i\varepsilon)} \frac{1}{((P-q)^2 - M_\pi^2 + i\varepsilon)}, \tag{6.5}$$

which is regularised using dimensional regularisation,

$$G(E) \to i\mu^\epsilon \int \frac{d^dq}{(2\pi)^d} \frac{1}{(q^2 - M_\pi^2 + i\varepsilon)} \frac{1}{((P-q)^2 - M_\pi^2 + i\varepsilon)}, \tag{6.6}$$

where $\epsilon = 4 - d$. We now revert to a hard cut-off regularisation for this function,

$$G(E) = \int_{|\vec{q}|<\Lambda} \frac{d^3q}{(2\pi)^3 \omega_\pi} \frac{1}{E^2 - 4\omega_\pi^2 + i\varepsilon}, \tag{6.7}$$

with Λ the cut-off momentum and we have defined $\omega_\pi = \sqrt{M_\pi^2 + \vec{q}^2}$. These two techniques are equivalent and the regularisation parameters may be matched via

$$\Lambda = \mu \exp \frac{1}{2} \left\{ \frac{2}{\epsilon} - \gamma_E + \ln \pi + 2 \right\}. \tag{6.8}$$

The imaginary part of $G(E)$ is finite:

$$\operatorname{Im} G(E) = -\frac{p}{8\pi E} \Theta\left(E^2 - (4M)^2\right). \tag{6.9}$$

The scalar two-point loop function is modified in the finite volume, for degenerate masses, as,

$$\widetilde{G}(E) = \frac{1}{L^3} \sum_{|\vec{q}|<\Lambda} \frac{1}{\omega_\pi} \frac{1}{E^2 - 4\omega_\pi^2}, \tag{6.10}$$

where the loop momentum in the finite volume loop function is discretised,

$$\vec{q} = (2\pi/L)\vec{n}, \quad \vec{n} \in \mathbb{Z}^3. \tag{6.11}$$

The finite volume in which lattice QCD simulations are performed are characterised by the lattice size L and the lattice spacing a. The correlation functions are computed in this lattice, leading to the measured quantities that correspond to poles of the T-matrix in finite volume. Lüscher derived the relation between the discrete energy levels and the infinite volume observables by bridging them via the finite volume T-matrix and relating it to its infinite volume counterpart.

We begin with the Bethe-Salpeter equation [88], used in the context of chiral effective field theory for coupled channels in [89], and later adapted to the unitarised finite volume T-matrix in [90, 91] as,

$$\widetilde{T}_l(E) = \frac{-V_l(E)}{1 - V_l(E)\widetilde{G}(E)}. \tag{6.12}$$

The matrix $V_l(E)$ does not require a finite volume counterpart. This function does not possess a singularity in the physical region, which implies that the integral and discrete sums present in $V_l(E)$ can only differ by exponentially suppressed terms at large lattice size L [90]. $V_l(E)$ can thus be eliminated by using,

$$\begin{aligned} T_l^{-1} &= -V_l^{-1} + G, \\ \widetilde{T}_l^{-1} &= -V_l^{-1} + \widetilde{G}, \end{aligned} \tag{6.13}$$

to obtain,

$$\widetilde{T}_l^{-1}(E) = T_l^{-1}(E) + \Delta G(E), \tag{6.14}$$

where we have introduced the difference between the infinite volume (Eq. (6.7)) and finite volume (Eq. (6.10)) scalar two-point loop functions,

$$\Delta G(E) = \widetilde{G}(E) - G(E). \tag{6.15}$$

Cut-off regularisation ensures that the function $\Delta G(E)$ is UV-finite as long as $\Lambda \gg M_\pi$, since the UV contributions are cancelled due to $\widetilde{G}(E) - G(E)$. In Eq. (6.14), each of $\widetilde{T}_l^{-1}(E)$, $T_l^{-1}(E)$ and $\Delta G(E)$ are UV finite as well as scale-independent.

The discrete energy level on the lattice is recovered through the decay of the finite volume correlation function $\widetilde{C}_l(\tau)$ in Euclidean time [92],

$$\widetilde{C}_l(\tau) \sim \exp\left\{-E_l^i \tau\right\}. \tag{6.16}$$

This energy level, as mentioned, is a pole in the finite volume T-matrix, leading to

$$\begin{aligned} \widetilde{T}_0^{-1}(E_0^i) &= T_0^{-1}(E_0^i) + \Delta G(E_0^i) = 0, \\ T_0^{-1}(E_0) &= -\Delta G(E_0), \end{aligned} \tag{6.17}$$

where we have considered just the S-wave (corresponding to the index 0) for the two-particle eigenenergies in finite volume, which are denoted by E_0 here.

For small centre-of-mass momenta p, $p \cot \delta_0$ has the *effective range expansion* [87],

$$p \cot \delta_0 = -\frac{1}{a_0} + \frac{1}{2} r_0 p^2 + \mathcal{O}\left(p^4\right), \tag{6.18}$$

which extends to both above and below the threshold (when $p^2 < 0$). The coefficients a_0 and r_0 are the scattering length and effective range for the S-wave, respectively. Using Eq. (6.4), Eq. (6.17) and Eq. (6.18), we can thus relate the scattering lengths and effective ranges to finite volume quantities [2],

$$-\frac{1}{a_0} + \frac{1}{2} r_0 p^2 + \ldots = -8\pi E_0 \Delta G\left(E_0\right) + ip. \tag{6.19}$$

Here, the right hand side is always ensured to be real since, above threshold, the imaginary part of the first term $-8\pi E_0 \Delta G\left(E_0\right)$ cancels the second term ip, and an analytic continuation of p can be performed below the threshold as $p = i\sqrt{4M_\pi^2 - E_0^2}/2$. This Eq. (6.19) is essential for our objectives laid out at the beginning of the chapter:

- Multiple discrete energy levels E_0 may be extracted for different values of the lattice size L, which can then be used to fit the scattering lengths and effective ranges $\{a_0, r_0\}$ in order to estimate the PQChPT parameters, the LECs that appear in the expressions of the scattering lengths and effective ranges.
- Conversely, the values of $\{a_0, r_0\}$ can be evaluated from PQChPT, as we showed in the previous chapter for the scattering lengths, and applied in Eq. (6.19) to predict the discrete energy levels E_0. Comparing these predicted energy levels would test the veracity of the corresponding lattice computation.

6.2 Effective Single-Channel S-Wave Amplitudes

It is clear from our analysis in the previous chapter that the complexity of lattice computations of $\pi\pi$ scattering increases with decreasing isospin. The $I = 0$ scattering amplitude requires the evaluation of all the four different types of Wick contraction diagrams and thus is the most expensive one to carry out on the lattice. In particular, the rectangular (R, singly disconnected) and the vacuum (V, doubly disconnected) diagrams have high signal-to-noise ratios and are difficult to extract, while the crossed (C, connected) and direct (D, connected) diagrams can be computed very accurately. Using the methods of the previous chapter, we express the individual Wick contraction amplitudes in terms of specific scattering processes of mesons in $SU(4|2)$ PQChPT [1]:

$$\begin{aligned}
T^D(s,t,u) &\equiv T_{(u\bar{d})(j\bar{k})\to(u\bar{d})(j\bar{k})}(s,t,u), \\
T^C(s,t,u) &\equiv T_{(u\bar{d})(j\bar{k})\to(u\bar{k})(j\bar{d})}(s,t,u) \\
T^R(s,t,u) &\equiv T_{(j\bar{u})(u\bar{k})\to(j\bar{d})(d\bar{k})}(s,t,u), \\
T^V(s,t,u) &\equiv T_{(u\bar{d})(d\bar{u})\to(j\bar{k})(k\bar{j})}(s,t,u).
\end{aligned} \tag{6.20}$$

These amplitudes $T^X(s,t,u)$ all obey the multi-channel unitarity relation Eq. (5.18) and are thus not independent single-channel amplitudes. We can, however, construct linear combinations of

these amplitudes to obtain effectively single-channel amplitudes that can then be directly analysed using the Lüscher equation (Eq. (6.19)). In order to illustrate the formalism to construct such linear combinations, we first consider a multi-channel scattering process that contains the crossed (C), direct (D) and rectangular (R) Wick contractions only, and their amplitudes from Eq. (6.20). The minimal basis required to resolve this process into single-channel linear combinations is five channels: $(j\bar{u})(u\bar{k})$, $(j\bar{d})(d\bar{k})$, $\pi^0(j\bar{k})$, $\widetilde{\eta}(j\bar{k})$ and $\widetilde{\phi}(j\bar{k})$, where the neutral mesons are defined in flavour space as,

$$\begin{aligned}\pi^0 &= \frac{1}{\sqrt{2}}(u\bar{u} - d\bar{d}),\\ \widetilde{\eta} &= \frac{1}{\sqrt{6}}(u\bar{u} + d\bar{d} - 2j\bar{j}),\\ \widetilde{\phi} &= \frac{1}{\sqrt{12}}(u\bar{u} + d\bar{d} + j\bar{j} - 3k\bar{k}).\end{aligned} \tag{6.21}$$

The different S-wave amplitudes of this coupled five-channel process are represented in a 5×5 symmetrical matrix,

$$T_0 = \begin{pmatrix} T_0^D + T_0^R & T_0^R & \frac{1}{\sqrt{2}}T_0^C & \frac{1}{\sqrt{6}}\left(T_0^C - 2T_0^R\right) & \frac{1}{2\sqrt{3}}\left(T_0^C - 2T_0^R\right) \\ T_0^R & T_0^D + T_0^R & -\frac{1}{\sqrt{2}}T_0^C & \frac{1}{\sqrt{6}}\left(T_0^C - 2T_0^R\right) & \frac{1}{2\sqrt{3}}\left(T_0^C - 2T_0^R\right) \\ \frac{1}{\sqrt{2}}T_0^C & -\frac{1}{\sqrt{2}}T_0^C & T_0^D & 0 & 0 \\ \frac{1}{\sqrt{6}}\left(T_0^C - 2T_0^R\right) & \frac{1}{\sqrt{6}}\left(T_0^C - 2T_0^R\right) & 0 & T_0^D + \frac{2}{3}\left(T_0^C + T_0^R\right) & \frac{1}{3\sqrt{2}}\left(2T_0^R - T_0^C\right) \\ \frac{1}{2\sqrt{3}}\left(T_0^C - 2T_0^R\right) & \frac{1}{2\sqrt{3}}\left(T_0^C - 2T_0^R\right) & 0 & \frac{1}{3\sqrt{2}}\left(2T_0^R - T_0^C\right) & T_0^D + \frac{5}{6}T_0^C + \frac{1}{3}T_0^R \end{pmatrix}. \tag{6.22}$$

This matrix is diagonalised via an orthogonal transformation,

$$T_0' = UT_0U^T = \text{diag}\left(T_0^D + T_0^C, T_0^D + T_0^C, T_0^D + T_0^C, T_0^D - T_0^C, T_0^D - \frac{1}{2}T_0^C + 3T_0^R\right), \tag{6.23}$$

where each diagonal entry is now an effective single-channel S-wave amplitude that complies with the single channel unitarity condition in Eq. (6.3) and can now be parameterised via Eq. (6.4). We also note that since T^C, T^D and T^R are dependent on each other, only three of the diagonal entries of T_0' are independent.

In order to generalise this formalism to include the vacuum diagram, we need a minimal basis of twelve channels, which requires the diagonalisation of a 12×12 matrix. This extension, however, is unnecessary since the fourth linear combination including the vacuum diagram is already familiar to us - it is just the full $I = 0$ S-wave $\pi\pi$ scattering amplitude,

$$T_0^{I=0} = 2T_0^D - T_0^C + 6T_0^R + 3T_0^V. \tag{6.24}$$

The normalisation utilised in Eq. (5.5), however, requires a rescaling of this amplitude by a factor of $\frac{1}{2}$ since $T_0^{I=0}$ has identical particles. Thus, we have constructed four, $SU(4|2)$ linear combinations of

single-channel S-wave amplitudes [2]:

$$\begin{aligned} T_0^{\alpha} &= T_0^D + T_0^C, \\ T_0^{\beta} &= T_0^D - T_0^C, \\ T_0^{\gamma} &= T_0^D - \frac{1}{2}T_0^C + 3T_0^R, \\ T_0^{\delta} &= T_0^D - \frac{1}{2}T_0^C + 3T_0^R + \frac{3}{2}T_0^V. \end{aligned} \tag{6.25}$$

As alluded to earlier, the T_0^{δ} is simply the $I = 0$ scattering amplitude and the T_0^{α} is the $I = 2$ amplitude, both exact up to a factor of 2. The four linear combinations correspond to the irreducible representations of the symmetric product of two 15-plets in $SU(4)$,

$$(\mathbf{15} \otimes \mathbf{15})_{\text{symm}} = \mathbf{1} \oplus \mathbf{15} \oplus \mathbf{20} \oplus \mathbf{84}, \tag{6.26}$$

arising from the scattering of two $SU(4)$ mesons.

It has also been verified that these single-channel amplitudes fulfil the single-channel unitarity constraints from Eq. (6.3):

$$\begin{aligned} \text{Im}(T_0^D + T_0^C) &= \frac{p}{8\pi E}\left|T_0^D + T_0^C\right|^2, \\ \text{Im}(T_0^D - T_0^C) &= \frac{p}{8\pi E}\left|T_0^D - T_0^C\right|^2, \\ \text{Im}(T_0^D - \frac{1}{2}T_0^C + 3T_0^R) &= \frac{p}{8\pi E}\left|T_0^D - \frac{1}{2}T_0^C + 3T_0^R\right|^2, \\ \text{Im}(T_0^D - \frac{1}{2}T_0^C + 3T_0^R + \frac{3}{2}T_0^V) &= \frac{p}{8\pi E}\left|T_0^D - \frac{1}{2}T_0^C + 3T_0^R + \frac{3}{2}T_0^V\right|^2. \end{aligned} \tag{6.27}$$

Thus, in finite volume, each of these amplitudes independently satisfies the single-channel Lüscher equation Eq. (6.17),

$$\begin{aligned} \left(T_0^D\left(E_0^{\alpha}\right) + T_0^C\left(E_0^{\alpha}\right)\right)^{-1} &= -\Delta G\left(E_0^{\alpha}\right), \\ \left(T_0^D\left(E_0^{\beta}\right) - T_0^C\left(E_0^{\beta}\right)\right)^{-1} &= -\Delta G\left(E_0^{\beta}\right), \\ \left(T_0^D\left(E_0^{\gamma}\right) - \frac{1}{2}T_0^C\left(E_0^{\gamma}\right) + 3T_0^R\left(E_0^{\gamma}\right)\right)^{-1} &= -\Delta G\left(E_0^{\gamma}\right), \\ \left(T_0^D\left(E_0^{\delta}\right) - \frac{1}{2}T_0^C\left(E_0^{\delta}\right) + 3T_0^R\left(E_0^{\delta}\right) + \frac{3}{2}T_0^V\left(E_0^{\delta}\right)\right)^{-1} &= -\Delta G\left(E_0^{\delta}\right). \end{aligned} \tag{6.28}$$

Let the discrete energy levels $E_0^i (i = \alpha, \beta, \gamma, \delta)$ correspond to the poles of the respective finite volume T-matrix, $T_0^i(E)$. Then the linear combinations of correlation functions $\widetilde{C}^X(\tau)(X = D, C, R, V)$ all

decay as a single exponential function at large Euclidean time τ,

$$\begin{aligned}
\widetilde{C}^{\alpha}(\tau) &\equiv 2\widetilde{C}^{D}(\tau) + 2\widetilde{C}^{C}(\tau) \sim \exp\left\{-E_0^{\alpha}\tau\right\}, \\
\widetilde{C}^{\beta}(\tau) &\equiv 2\widetilde{C}^{D}(\tau) - 2\widetilde{C}^{C}(\tau) \sim \exp\left\{-E_0^{\beta}\tau\right\}, \\
\widetilde{C}^{\gamma}(\tau) &\equiv 2\widetilde{C}^{D}(\tau) - \widetilde{C}^{C}(\tau) + 6\widetilde{C}^{R}(\tau) \sim \exp\left\{-E_0^{\gamma}\tau\right\}, \\
\widetilde{C}^{\delta}(\tau) &\equiv 2\widetilde{C}^{D}(\tau) - \widetilde{C}^{C}(\tau) + 6\widetilde{C}^{R}(\tau) + 3\widetilde{C}^{V}(\tau) \sim \exp\left\{-E_0^{\delta}\tau\right\}.
\end{aligned} \tag{6.29}$$

6.3 Scattering Lengths and Effective Ranges

We now provide the $SU(4|2)$ PQChPT predictions of the scattering lengths and effective ranges, which are extensions of the derivations in the Chapter 5. These are obtained via an expansion of $\mathrm{Re}\left[\left(T_0^i(E)\right)^{-1}\right]$ around the $\pi\pi$ threshold, for each $i = \alpha, \beta, \gamma, \delta$. The analytical results are [2],

$$\begin{aligned}
a_0^{\alpha} &= \frac{M_\pi}{16\pi F_\pi^2}\left[1 + \frac{M_\pi^2}{\pi^2 F_\pi^2}\left(-\frac{\bar{l}_1}{12} - \frac{\bar{l}_2}{6} + \frac{\bar{l}_3}{32} + \frac{\bar{l}_4}{8} - \frac{1}{32}\right)\right], \\
r_0^{\alpha} &= \frac{48\pi F_\pi^2}{M_\pi^3}\left[1 + \frac{M_\pi^2}{\pi^2 F_\pi^2}\left(\frac{\bar{l}_1}{12} + \frac{\bar{l}_2}{18} - \frac{7\bar{l}_3}{96} - \frac{\bar{l}_4}{8} + \frac{31}{288}\right)\right],
\end{aligned} \tag{6.30}$$

$$\begin{aligned}
a_0^{\beta} =& -\frac{M_\pi}{16\pi F_\pi^2}\left[1 - 4\mu_\pi + \frac{M_\pi^2}{F_\pi^2}\left(\frac{\bar{l}_1}{12\pi^2} + \frac{\bar{l}_2}{6\pi^2} - \frac{\bar{l}_3}{32\pi^2} - \frac{\bar{l}_4}{8\pi^2} - 96L_0^{\mathrm{PQ,r}}\right.\right. \\
&\left.\left. -32L_3^{\mathrm{PQ,r}} + 32L_5^{\mathrm{PQ,r}} - 32L_8^{\mathrm{PQ,r}} - \frac{3}{32\pi^2}\right)\right], \\
r_0^{\beta} =& -\frac{48\pi F_\pi^2}{M_\pi^3}\left[1 + \frac{100}{9}\mu_\pi + \frac{M_\pi^2}{F_\pi^2}\left(-\frac{\bar{l}_1}{12\pi^2} - \frac{\bar{l}_2}{18\pi^2} + \frac{7\bar{l}_3}{96\pi^2} + \frac{\bar{l}_4}{8\pi^2} + \frac{160}{3}L_0^{\mathrm{PQ,r}}\right.\right. \\
&\left.\left. +32L_3^{\mathrm{PQ,r}} - \frac{160}{3}L_5^{\mathrm{PQ,r}} + \frac{224}{3}L_8^{\mathrm{PQ,r}} + \frac{61}{288\pi^2}\right)\right],
\end{aligned} \tag{6.31}$$

$$\begin{aligned}
a_0^{\gamma} =& -\frac{7M_\pi}{32\pi F_\pi^2}\left[1 - \frac{18}{7}\mu_\pi + \frac{M_\pi^2}{F_\pi^2}\left(\frac{\bar{l}_1}{42\pi^2} + \frac{\bar{l}_2}{21\pi^2} - \frac{\bar{l}_3}{112\pi^2} - \frac{\bar{l}_4}{28\pi^2} + \frac{144}{7}L_0^{\mathrm{PQ,r}}\right.\right. \\
&\left.\left. +\frac{48}{7}L_3^{\mathrm{PQ,r}} + \frac{48}{7}L_5^{\mathrm{PQ,r}} + \frac{48}{7}L_8^{\mathrm{PQ,r}} + \frac{5}{56\pi^2}\right)\right], \\
r_0^{\gamma} =& -\frac{288\pi F_\pi^2}{49M_\pi^3}\left[1 - \frac{110}{63}\mu_\pi + \frac{M_\pi^2}{F_\pi^2}\left(\frac{\bar{l}_1}{126\pi^2} + \frac{17\bar{l}_2}{189\pi^2} + \frac{25\bar{l}_3}{1008\pi^2} - \frac{\bar{l}_4}{84\pi^2}\right.\right. \\
&\left.\left. +\frac{592}{21}L_0^{\mathrm{PQ,r}} + \frac{496}{21}L_3^{\mathrm{PQ,r}} + \frac{16}{7}L_5^{\mathrm{PQ,r}} - \frac{400}{21}L_8^{\mathrm{PQ,r}} - \frac{25}{189\pi^2}\right)\right],
\end{aligned} \tag{6.32}$$

$$
\begin{aligned}
a_0^\delta &= -\frac{7M_\pi}{32\pi F_\pi^2}\left[1+\frac{M_\pi^2}{\pi^2F_\pi^2}\left(\frac{5\bar{l}_1}{84}+\frac{5\bar{l}_2}{42}-\frac{5\bar{l}_3}{224}+\frac{\bar{l}_4}{8}+\frac{5}{32}\right)\right],\\
r_0^\delta &= -\frac{288\pi F_\pi^2}{49M_\pi^2}\left[1+\frac{M_\pi^2}{\pi^2F_\pi^2}\left(\frac{11\bar{l}_1}{84}+\frac{43\bar{l}_2}{378}+\frac{125\bar{l}_3}{2016}-\frac{\bar{l}_4}{8}-\frac{479}{864}\right)\right].
\end{aligned}
\tag{6.33}
$$

Here, $\mu_\pi = \left(M_\pi^2/\left(32\pi^2F_\pi^2\right)\right)\ln\left(M_\pi^2/\mu^2\right)$, with the renormalisation scale μ from Eq. (5.8), and the scale-independent physical pion mass and pion decay constant are M_π and F_π. As in Eq. (5.13) and Eq. (5.12), the $\{\bar{l}_i\}$ and the $\{L_i^{PQ,r}\}$ are the LECs from the $SU(4|2)$ PQChPT Lagrangian.

We have now completed the construction of the formalism required to carry out the analysis outlined in Chapter 5. The discrete, finite volume energy levels $\{E_0^\alpha, E_0^\beta\}$, determined precisely on the lattice since they are only dependent on the connected Wick contraction diagrams C and D, can be used to accurately determine several physical and unphysical LECs of the theory via the fitting of the predicted $\left\{a_0^{\alpha,\beta}, r_0^{\alpha,\beta}\right\}$. This is especially useful in the case of $\left\{a_0^\beta, r_0^\beta\right\}$ since these are dependent upon the unphysical LECs $L_0^{\mathrm{PQ,r}}$ and $L_3^{\mathrm{PQ,r}}$, which have high uncertainties. Multiple lattice computations of E_0^β for different lattice sizes L can be utilised for better fitting and, ultimately, a better estimation of these LECs.

Using these more precise values of $L_0^{\mathrm{PQ,r}}$ and $L_3^{\mathrm{PQ,r}}$ and the PQChPT predicted values of $\left\{a_0^\gamma, r_0^\gamma\right\}$, the energy level E_0^γ can be predicted using the single-channel Lüscher equation Eq. (6.19). Thus, the theoretical prediction combined with the lattice QCD calculated E_0^γ will provide a detailed inspection of the accuracy of lattice QCD computations of the rectangular (R), singly disconnected diagram. This method may also be extended to the fourth energy level E_0^δ, but since it is just the $I = 0$ energy level and is independent of unphysical LECs, it is straightforward to compute the theoretical prediction using $SU(2)$ ChPT.

6.4 Numerical Analysis

We shall now perform the numerical analysis to complete the procedure outlined in the previous section. We use the lattice QCD data of $\pi\pi$ scattering provided to us by the *European Twisted Mass* collaboration that uses $N_f = 2+1+1$ and lattice spacing $a = 0.086$ fm [76, 93]. We also use data from two different ensembles that have the same bare QCD parameters, but different volumes, corresponding to different lattice sizes. They are called A40.32 and A40.24, which correspond to $(L/a)^3 \times T/a = 32^3 \times 64$ and $24^3 \times 48$ respectively. As already elucidated, we are first required to extract the energy levels $\{E_0^\alpha, E_0^\beta\}$ using the connected (crossed (C) and direct (D)) correlation functions. We follow the technique described in [58], in order to minimise pollution from thermal states, and define,

$$
R_i(\tau + a/2) \equiv \frac{\widetilde{C}^i(\tau) - \widetilde{C}^i(\tau + a)}{C_\pi^2(\tau) - C_\pi^2(\tau + a)},
\tag{6.34}
$$

where $C_\pi(\tau)$ is the single pion two-point correlation function and $i = \alpha, \beta$. Next, we fit the data to a functional form of this function

$$
R_i(\tau + a/2) = A\left(\cosh\left(\delta E_0^i \tau'\right) + \sinh\left(\delta E_0^i \tau'\right)\coth\left(2M_\pi \tau'\right)\right),
\tag{6.35}
$$

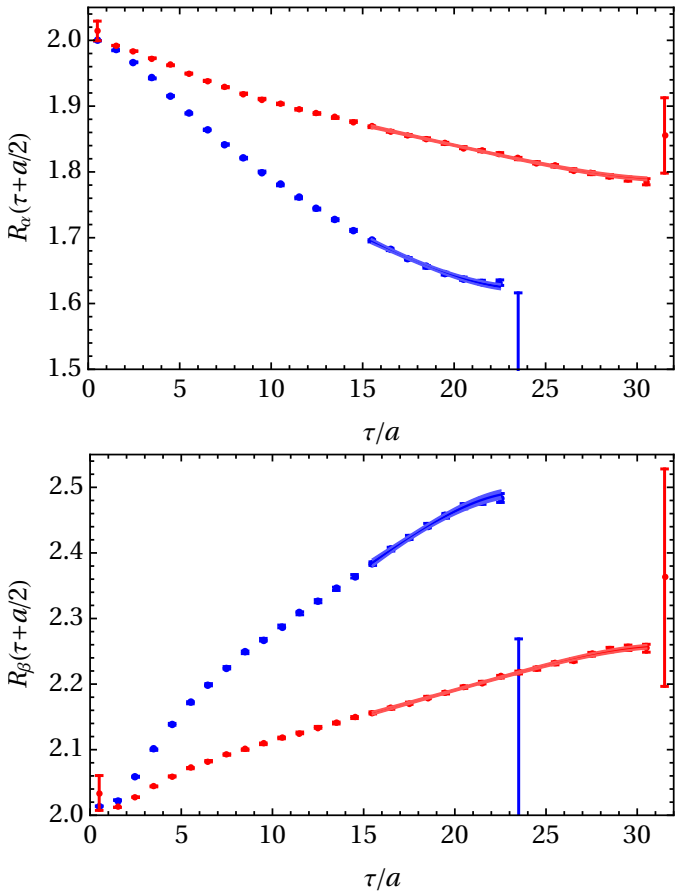

Figure 6.1: Fit to the function $R_i(\tau + a/2)$ defined in Eq. (6.35) for $i = \alpha$ (top) and β (bottom). The blue and red dots represent the data from the ensembles A40.24 and A40.32 of [76], respectively.

with $\tau' = \tau + a/2 - T/2$ and the energy shift δE_0^i is to be extracted,

$$\delta E_0^i = E_0^i - 2M_\pi. \tag{6.36}$$

The pion masses used in [76] at finite volume are $aM_\pi = 0.1415(2)$ and $0.1446(3)$ for the ensembles A40.32 and A40.24 respectively. The relation of these finite volume values to the infinite volume values we require is outlined in Appendix D, along with the error analysis implemented in this fitting procedure.

We use the bootstrap method for estimating the errors of the fitted discrete energy levels [2]. In Fig. 6.1, we plot the distribution of the mean values for 1500 bootstrap samples, wherein the error is taken as the standard deviation of this distribution. The accuracy of results from data fitting depends on the fit range, and it is preferable to consider a large number of fit ranges and average over the results using a carefully chosen weight [70]. Here, however, we compromise and perform a single fit for each ensemble over a specific fit range, and the best-fit curves are shown in Fig 6.1. This fit range, $16a \leq \tau \leq 31a$ for $A40.32$ and $16a \leq \tau \leq 23a$ for $A40.24$, is chosen since it best reproduces the $I = 2$ energy shifts in [70].

Correlation function	$a\,\delta E_0$ (A40.32)	$a\,\delta E_0$ (A40.24)	a_0/a	r_0/a
$\widetilde{C}^{I=2}$	0.0033(1)	0.0082(3)	1.09(6)	53(107)
$\widetilde{C}^{I=2}$, SU(2) ChPT			1.300(19)	83(2)
$\widetilde{C}^{\alpha}$	0.0034(1)	0.0083(3)	1.124(54)	41(97)
$\widetilde{C}^{\beta}$	−0.0036(1)	−0.0086(3)	−1.429(77)	140(85)

Table 6.1: The fitted energy shifts, the extracted inverse scattering lengths and effective ranges (with an infinite volume pion mass of about 323 MeV) obtained using the connected $\pi\pi$ correlation functions. For comparison, we list the $I = 2$ values with the corresponding errors from the original lattice paper [76] in the second row, and include the NLO ChPT predictions of the $I = 2$ threshold parameters in the third row.

The different fitted energy levels and the resulting threshold parameters are displayed in Table 6.1. It is evident that the scattering lengths are determined to a high accuracy, whereas the effective ranges are riddled with high errors. This conforms with our expectations since the effective range is the second term in the effective range expansion Eq. (6.18), and affects the discrete energy levels to a much smaller degree (Eq. (6.19)). This phenomenon has already been observed in [70]. We also quote the $I = 2$ scattering length and effective range predicted by ChPT at NLO obtained from Eq. (6.30). There is a small discrepancy of about 2.4σ between the scattering length of NLO ChPT and the performed fit to lattice data. This discrepancy probably arises due to the lattice fitting of $\bar{l}_1^{\text{phys}}$ and $\bar{l}_2^{\text{phys}}$, since these quantities are absent in the pion mass and pion-decay constant in infinite volume NLO ChPT, and are only estimated via finite size effects. Here, we introduce the 'physical' LECs $\bar{l}_i^{\text{phy}}$ as,

$$\bar{l}_i\left(M_\pi\right) = \bar{l}_i^{\text{phy}} - \ln\left(M_\pi^2/M_{\pi,\,\text{phy}}^2\right), \tag{6.37}$$

where the physical pion mass is, $M_{\pi,\text{phy}} \approx 138$ MeV.

The next step of our process involves the fitting of the unphysical LECs $\left\{L_0^{\text{PQ,r}}, L_3^{\text{PQ,r}}\right\}$ by modifying the expressions for a_0^β and r_0^β:

$$\begin{aligned} 3L_0^{\text{PQ,r}} + L_3^{\text{PQ,r}} =& -\frac{1}{512\pi M_\pi a_0^\beta} - \frac{F_\pi^2}{32M_\pi^2}\left(1+4\mu_\pi\right) + \frac{\bar{l}_1}{384\pi^2} + \frac{\bar{l}_2}{192\pi^2} - \frac{\bar{l}_3}{1024\pi^2} - \frac{\bar{l}_4}{256\pi^2} \\ &+ L_5^{\text{PQ,r}} - L_8^{\text{PQ,r}} - \frac{3}{1024\pi^2} \\ L_0^{\text{PQ,r}} =& \frac{1}{2048\pi}\left(-\frac{3}{M_\pi a_0^\beta} + M_\pi r_0^\beta\right) + \frac{F_\pi^2\mu_\pi}{6M_\pi^2} + \frac{\bar{l}_2}{384\pi^2} + \frac{\bar{l}_3}{1024\pi^2} - \frac{1}{2}L_5^{\text{PQ,r}} \\ &+ L_8^{\text{PQ,r}} + \frac{17}{6144\pi^2}. \end{aligned} \tag{6.38}$$

It is particularly beneficial to obtain a precise value of the linear combination $3L_0^{\text{PQ,r}} + L_3^{\text{PQ,r}}$ since it is independent of the effective range r_0^β and the large uncertainty that accompanies it, and it appears in the scattering lengths $\left\{a_0^\beta, a_0^\gamma\right\}$. Our estimation of this linear combination agrees well with the NNLO fit mentioned in the previous chapter [84], and also has the advantage of being determined with a lower uncertainty. However, there is a disparity of about 1.6σ in the values of L_0^{PQ} extracted by us and

Parameters	Previous	This Work
F_0 [MeV]	85.58(38)	
$\bar{l}_1^{\text{phy}}$	−0.309(139)	
$\bar{l}_2^{\text{phy}}$	4.325(10)	
$\bar{l}_3^{\text{phy}}$	3.537(47)	
$\bar{l}_4^{\text{phy}}$	4.735(17)	
$10^3 L_5^{\text{PQ},r}$	0.501(43)	
$10^3 L_8^{\text{PQ},r}$	0.581(22)	
$10^3(3L_0^{\text{PQ},r} + L_3^{\text{PQ},r})$	−0.6(1.4)	−0.70(18)
$10^3 L_0^{\text{PQ},r}$	1.0(1.1)	5.7(1.9)

Table 6.2: The $SU(2)$ ChPT and $SU(4|2)$ PQChPT LECs relevant for our analysis. Values for the pion decay constant F_0 in the chiral limit and the physical LECs $\{\bar{l}_i^{\text{phy}}\}$ are taken from [93]. The LECs $\{L_5^{\text{PQ,r}}, L_8^{\text{PQ,r}}\}$ and the combination $\{3L_0^{\text{PQ,r}} + L_3^{\text{PQ},r}, L_0^{\text{PQ,r}}\}$ are obtained from [84] via NLO and NNLO fits respectively. In the third column, our fitted values of $\{3L_0^{\text{PQ,r}} + L_3^{\text{PQ},r}, L_0^{\text{PQ,r}}\}$ are listed. The renormalisation scale of the unphysical LECs is 1 GeV.

the values obtained in [84]. Since our analysis has been entirely performed at NLO and the analysis in [84] required more unstable fits at NNLO, which are very sensitive to the fitting procedure, we assert that our result of L_0^{PQ} is more realistic and well-founded.

We now turn to the next step in our procedure - prediction of the energy shifts $\left\{\delta E_0^\gamma, \delta E_0^\delta\right\}$ as functions of the lattice size L. We are now able to utilise our estimations of the LECs in Table 6.2 and calculate the scattering lengths and effective ranges in Eq. (6.32) and Eq. (6.33). Since the scattering length a_0^γ depends on the linear combination $3L_0^{\text{PQ,r}} + L_3^{\text{PQ,r}}$, which has been determined reasonably precisely above, the value of the scattering length is estimated accurately. However, the expression for r_0^γ contains L_0^{PQ} that has a large uncertainty, particularly for the larger pion mass that increases effects from the counterterms. As mentioned already, the scattering length and effective range $\left\{a_0^\delta, r_0^\delta\right\}$ for the $I = 0$ amplitude depend only on physical LECs and are accurately estimated. The energy shift δE_0^δ is then determined via a numerical solution of Eq. (6.19). The energy shifts are plotted in Fig. 6.2 for $3 < LM_\pi < 5$, using three different pion masses, $M_\pi = 138$, 236 and 330 MeV. These results warrant a few observations:

- Both the γ and δ channels have negative energy shifts, indicating that they are attractive in nature. Their magnitudes also increase with increasing pion mass and decreasing lattice size.
- The majority of the uncertainty of δE_0^γ is due to r_0^γ, which has a higher impact as δE_0^γ gets larger. This indicates that the effective range expansion is breaking down in this limit.
- This leads to the error bar for δE_0^γ diminishing even at a relatively large pion mass M_π of 330 MeV, with $LM_\pi > 4$, providing us with a controlled and accurate prediction of this energy shift.

We thus provide specific, concrete predictions of energy shifts that can act as consistency checks for lattice QCD calculations of disconnected diagrams in mesonic scattering.

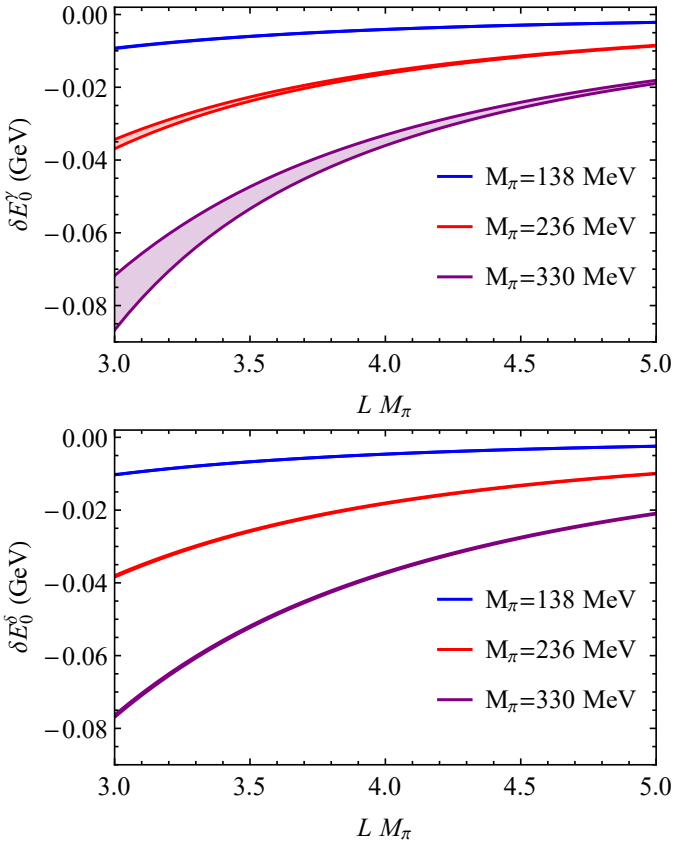

Figure 6.2: Prediction of the energy shifts δE_0^γ and δE_0^δ as a function of the lattice size L at $M_\pi = 138$ MeV (blue), 236 MeV (red) and 330 MeV (purple).

6.5 Summary

It was essential, after the derivation of infinite volume results for the different connected and disconnected Wick contraction diagrams in Chapter 5, to chart a meaningful path towards relating these results to the lattice QCD calculated observables in the finite volume. In this chapter, we have shown how the threshold parameters of $\pi\pi$ scattering, obtained via a deft construction of single-channel amplitudes containing different combinations of connected and disconnected diagrams, may be related to the discrete energy levels calculated in the finite volume.

Our strategy to accomplish this began with an elaborate mechanism to derive an adapted version of the famed Lüscher equation that directly compared the infinite volume scattering length and effective range with the discrete energy shift in the finite volume for a particular diagram. The effective single-channel S-wave amplitudes that we constructed laid the path for a multi-step approach to provide exact predictions for the calculation of two specific correlation functions on the lattice. Firstly, we developed single-channel amplitudes that contained only connected contributions. We utilised accurate lattice data for these connected contributions to fit our threshold parameters and obtained a new level of precision of the LECs $L_0^{\rm PQ}$ and $L_3^{\rm PQ}$ and their linear combination. We then input these parameters into amplitudes containing disconnected contributions to provide stringent predictions of

the corresponding energy levels, which any future lattice QCD calculation must adhere to, since these predictions are founded in a concrete, unitary EFT.

CHAPTER 7

Conclusion

In this work, we illustrated a method to relate effective field theoretical methods to specific, finite volume quantities computed on the lattice. We began with a description of QCD and its low-energy effective field theory, ChPT, and provided the theoretical context for our investigations. In particular, we detailed the complex symmetry structure of the QCD vacuum, the resulting hadronic spectrum and, in particular, the dynamics of the lightest mesons, the pions. Using $SU(2)$ ChPT, we replicated the most significant quantities related to the pions up to next-to-leading order [33] - mass renormalisation (Eq. (3.63)), wavefunction renormalisation (Eq. (3.64)), the renormalisation of the pion-decay constant (Eq. (3.65)) and the full scattering amplitude (Eq. (3.67)).

In order to execute the stated goal of separating the different connected and disconnected diagrams and evaluating their individual contributions to $\pi\pi$ scattering, we were required to enlarge ChPT via the trick of partial quenching. We developed $SU(4|2)$ partially quenched ChPT, resulting in the inclusion of unphysical mesons. Certain scattering processes of these mesons corresponded to the different connected and disconnected Wick contractions of quarks (Eq. (6.20)). This allowed us to provide infinite volume predictions of (the imaginary parts of) the partial-wave projected amplitudes (Fig. 5.7) and scattering lengths (Eq. (5.25) and (Eq. (5.31)) [1]. These predictions are dependent on the low-energy constants appearing in the NLO $SU(4|2)$ PQChPT Lagrangian (Eq. (4.16)), some of which (and their linear combinations) had been determined to a poor accuracy (Table 5.2) by previous works.

We then proceeded to outline a strategy to directly contrast our PQChPT-derived predictions with definite lattice QCD calculations of the different diagrams. Since, on the lattice, the evaluated quantities are discrete energy levels in the finite volume, a relation to the infinite volume threshold parameters required the usage of the Lüscher equation. We derived a modified form of the famous Lüscher equation that related the single-channel S-wave scattering lengths and effective ranges to the specific discrete energy shifts (Eq. (6.19)). This was followed by a diagonalisation procedure to obtain different, single-channel linear combinations of the connected and disconnected diagram amplitudes, from which we derived fully analytical expressions for the threshold parameters (Eqs. (6.30), (6.31), (6.32) and (6.33)) [2].

The scattering lengths and effective ranges in these four equations are dependent on different combinations of the connected and disconnected diagrams. The threshold parameters of Eq. (6.30) are obtained from the $I = 2$ $\pi\pi$ scattering amplitude, and are thus dependent only on the physical LECs from $SU(2)$ ChPT. The $\{a_0^\beta, r_0^\beta\}$ of Eq. (6.31), however, are dependent on the linear combination

of unphysical LECs $3L_0^{\mathrm{PQ,r}} + L_3^{\mathrm{PQ,r}}$ and the LEC L_0^{PQ}, and also contain only connected (crossed, C and direct, D) diagram contributions. This allowed us to fit our analytical expressions for $\{a_0^\beta, r_0^\beta\}$ to actual lattice data for these connected contributions (Table 6.1) and obtain newer, more precise values for the aforementioned LECs (Table 6.2) [2].

This increase in precision of the unphysical LECs $3L_0^{\mathrm{PQ,r}} + L_3^{\mathrm{PQ,r}}$ and L_0^{PQ} enabled us to plug them back into the expressions for the $\{a_0^\gamma, r_0^\gamma\}$, which contain contributions from the singly-disconnected (rectangular, R) diagram. This allowed us to use the Lüscher equation (Eq. 6.19)) to obtain precise bounds for the discrete energy shift δE_0^γ, which forms a concrete, stringent prediction for future lattice QCD explorations of $\pi\pi$ scattering (Fig. 6.2). We also provided a similar prediction for the energy shift δE_0^δ, which simply corresponds to the total $I = 0$ $\pi\pi$ scattering amplitude and contains contributions from all the different types of Wick contraction diagrams.

The various predictions of this work - the numerical estimations of the unphysical PQChPT LECs, and the energy shifts corresponding to different connected and disconnected diagrams - highlight the efficacy of combining EFT methods with the computational prowess of lattice QCD. It enabled us to obtain LECs at a higher precision, while also providing numerical bounds for future lattice QCD studies of $\pi\pi$ scattering. We stress that such a synergy and interplay between chiral effective field theories and lattice QCD is going to be vitally important for all future explorations of hadronic processes. The extension of this work, in particular, to include the strange quark in $SU(6|3)$ PQChPT and evaluate πK scattering processes is already underway. Another exciting avenue of future research is the employment of the framework detailed in this work to evaluate the disconnected contributions to the πN σ-term, which is a crucial ingredient in various nucleon matrix elements involved in dark matter direct detection experiments.

APPENDIX A

Noether's Theorem

Noether's theorem provides the connection between continuous symmetries and conserved quantities of a physical system [94]. We apply Noether's theorem to evaluate conserved currents and charges of QCD in Chapter 2 [95]. In order to formalise Noether's theorem, we start with a general Lagrangian which depends on fields Φ_i and their partial derivatives, $\partial_\mu \Phi_i$ $(i = 1, \ldots, n)$,

$$\mathcal{L} = \mathcal{L}\left(\Phi, \partial_\mu \Phi\right), \tag{A.1}$$

where the index i has been suppressed. It is straightforward to obtain the equations of motion for this Lagrangian,

$$\frac{\partial \mathcal{L}}{\partial \Phi_i} - \partial_\mu \frac{\partial \mathcal{L}}{\partial \partial_\mu \Phi_i} = 0, \quad i = 1, \ldots, n. \tag{A.2}$$

We now assume that the Lagrangian is invariant under a global symmetry transformation of the constituent fields. This global symmetry can be promoted to a local one in order to derive the Noether currents. The tranformations, in this case, depend on r, real, local parameters $\epsilon_a(x)$,

$$\Phi_i(x) \mapsto \Phi_i'(x) = \Phi_i(x) + \delta\Phi_i(x) = \Phi_i(x) - i\varepsilon_a(x) F_{ai}[\Phi(x)], \tag{A.3}$$

leading to a variation of the Lagrangian (up to order ϵ^2),

$$\begin{aligned}
\delta\mathcal{L} =& \mathcal{L}\left(\Phi', \partial_\mu \Phi'\right) - \mathcal{L}\left(\Phi, \partial_\mu \Phi\right) \\
=& \frac{\partial \mathcal{L}}{\partial \Phi_i}\delta\Phi_i + \frac{\partial \mathcal{L}}{\partial \partial_\mu \Phi_i}\partial_\mu \delta\Phi_i \\
=& -i\partial_\mu \varepsilon_a F_{ai} - i\varepsilon_a \partial_\mu F_{ai} \\
=& \varepsilon_a \left(-i\frac{\partial \mathcal{L}}{\partial \Phi_i}F_{ai} - i\frac{\partial \mathcal{L}}{\partial \partial_\mu \Phi_i}\partial_\mu F_{ai}\right) + \partial_\mu \varepsilon_a \left(-i\frac{\partial \mathcal{L}}{\partial \partial_\mu \Phi_i}F_{ai}\right) \\
\equiv& \varepsilon_a \partial_\mu J_a^\mu + \partial_\mu \varepsilon_a J_a^\mu.
\end{aligned} \tag{A.4}$$

Here, we have defined a four-current density for each infinitesimal transformation of the fields,

$$J_a^\mu = -i\frac{\partial \mathcal{L}}{\partial \partial_\mu \Phi_i} F_{ai}. \tag{A.5}$$

Next, we can calculate the divergence of this four-current,

$$\begin{aligned} \partial_\mu J_a^\mu &= -i\left(\partial_\mu \frac{\partial \mathcal{L}}{\partial \partial_\mu \Phi_i}\right) F_{ai} - i\frac{\partial \mathcal{L}}{\partial \partial_\mu \Phi_i}\partial_\mu F_{ai} \\ &= -i\frac{\partial \mathcal{L}}{\partial \Phi_i} F_{ai} - i\frac{\partial \mathcal{L}}{\partial \partial_\mu \Phi_i}\partial_\mu F_{ai} \end{aligned} \tag{A.6}$$

where the equations of motion have been utilised and Eq. (A.4) has thus been verified. The four-currents and their divergences can be obtained from Eq. (A.4) as,

$$\begin{aligned} J_a^\mu &= \frac{\partial \delta \mathcal{L}}{\partial \partial_\mu \varepsilon_a}, \\ \partial_\mu J_a^\mu &= \frac{\partial \delta \mathcal{L}}{\partial \varepsilon_a}. \end{aligned} \tag{A.7}$$

Since the parameters ϵ_a have been chosen to be local, but the Lagrangian was assumed to be invariant only under global transformations, the term $\partial_\mu \varepsilon_a$ vanishes and the four-current is conserved since the divergence also disappears. We can define the charge for this conserved current as,

$$Q_a(t) = \int d^3x J_a^0(t, \vec{x}), \tag{A.8}$$

which is a constant of motion as it is time-independent. This procedure can then be applied to chiral symmetry in QCD as explained in Chapter 2.

APPENDIX B

The Groups $SU(N)$ and $SU(N+M|M)$

We will provide a brief introduction to the Lie groups relevant to this work, the special unitary groups. In particular, $SU(2)$ and the graded group $SU(4|2)$ are crucial ingredients in the construction of Chiral Perturbation Theory and Partially Quenched Chiral Perturbation Theory, respectively.

The group $SU(N)$ is the set of all unitary, unimodular $N \times N$ matrices U with unit determinant, which act on $\mathbb{C}^N$ [96]:

$$UU^\dagger = \mathbb{1}_{N\times N}, \quad \det U = 1. \tag{B.1}$$

The simply connected, compact Lie algebra $\mathfrak{su}(N)$ of the group $SU(N)$ has (n^2-1) independent generators which satisfy the Lie bracket,

$$\left[T^a, T^b\right] = f^{abc}T^c, \tag{B.2}$$

where T^a are $N \times N$ matrices which form the basis of the algebra in the fundamental representation and the f^{abc} are the structure constants which encode the local properties of the group.

B.1 $SU(2)$

The basis of $SU(2)$ thus has three elements, which are given by the Pauli matrices,

$$\tau_1 = \begin{pmatrix} 0 & 1 \\ 1 & 0 \end{pmatrix}, \quad \tau_2 = \begin{pmatrix} 0 & -i \\ i & 0 \end{pmatrix}, \quad \tau_3 = \begin{pmatrix} 1 & 0 \\ 0 & -1 \end{pmatrix}, \tag{B.3}$$

and the structure constants,

$$\left[\frac{\tau_a}{2}, \frac{\tau_b}{2}\right] = i\epsilon_{abc}\frac{\tau_c}{2}. \tag{B.4}$$

They have the usual trace properties,

$$\mathrm{Tr}\left\{\tau_a\right\} = 0, \quad \mathrm{Tr}\left\{\tau_a\tau_b\right\} = 2\delta_{ab}. \tag{B.5}$$

Every $SU(2)$ group element is generated by these matrices and thus a group element U may be parameterised as

$$U = \exp\left(-i\sum_{a=1}^{3}\Theta_a\frac{\tau^a}{2}\right), \tag{B.6}$$

where the Θ_a are three real, independent parameters. The identity is given by $\Theta = 0$, $U = \mathbb{1}_{2\times2}$ and can be reached by smooth, infinitesimal transformations in the parameter space, and thus defines $SU(2)$ as being simply connected.

'Graded' indicates that the group element U of $SU(N+M|M)$ contains both commuting and anticommuting elements [97, 98]

$$U = \begin{pmatrix} A_1 & A_2 \\ A_3 & A_4 \end{pmatrix}, \tag{B.7}$$

where A_1, A_4 are $(a\times a), (b\times b)$ blocks of commuting c-numbers and A_2, A_3 are $(a\times b), (b\times a)$ blocks of anticommuting Grassmann numbers. The matrix U is unitary and belongs to $U(N+M|M)$ if $UU^\dagger = U^\dagger U = 1$, as in the usual case, but this requires complex conjugation of the anticommuting variables, $(\eta_1\eta_2)^* \equiv \eta_2^*\eta_1^*$.

We also define a 'supertrace' so that the cyclic property is retained,

$$\mathrm{Str}[U] \equiv \sum_{i=1}^{a} U_{ii} - \sum_{i=a+1}^{a+b} U_{ii} \quad \Rightarrow \quad \mathrm{Str}\left(U_1U_2\right) = \mathrm{Str}\left(U_2U_1\right). \tag{B.8}$$

Similarly, a 'superdeterminant' is defined as,

$$\mathrm{Sdet}\,U \equiv \exp\left[\mathrm{Str}\left(\ln U\right)\right] = \frac{\det(A - BD^{-1}C)}{\det(D)} \tag{B.9}$$

with $\mathrm{Sdet}\left(U_1U_2\right) = \mathrm{Sdet}\left(U_1\right)\mathrm{Sdet}\left(U_2\right)$. Thus, $U \in SU\left(N+M|M\right)$ is an unitary graded matrix with unit superdeterminant.

B.2 $SU(4|2)$

Specifically for the case of $SU(4|2)$, the group element A with gradation $(a|b)$ has the form,

$$U = \begin{pmatrix} A_1 & A_2 \\ A_3 & A_4 \end{pmatrix} \tag{B.10}$$

where $A_1\left(A_4\right)$ is a 4×4 (2×2) matrix of c -numbers while $A_2\left(A_3\right)$ is a 4×2 (2×4).

The non-linear representation of the Nambu-Goldstone bosons of PQChPT is given by

$$U = \exp\left\{\frac{2i}{F_0}\sum_{a=1}^{35}\phi^a T^a\right\}, \tag{B.11}$$

with the normalisation of the supertraceless generators

$$\mathrm{Str}\left[T^a T^b\right] = \frac{1}{2} g^{ab} \tag{B.12}$$

and the metric is a 35-dimensional matrix (with I_n the n -dimensional identity matrix),

$$g = \mathrm{diag}\left(I_{15}, -\tau^2, -\tau^2, -\tau^2, -\tau^2, -1, -\tau^2, -\tau^2, -\tau^2, -\tau^2, -I_3\right). \tag{B.13}$$

APPENDIX C

Dimensional Regularisation

In the calculations of the pion mass, wavefunction and pion-decay constant renormalisation, up to Next-to-Leading Order, a quadratically divergent integral such as in the one-point loop of Fig. 3.7 is encountered. The calculation of the external leg correction in the $\pi\pi$ scattering amplitude due to Fig. 3.4 also requires the evaluation of such a loop diagram. In d spacetime dimensions, this has the form,

$$A_0(M^2) = \mu^{4-d} \int \frac{d^d k}{(2\pi)^d} \frac{i}{k^2 - M^2 + i\epsilon}, \tag{C.1}$$

where k is the loop momentum and μ is the renormalisation scale. The renormalisation scale is included to ensure that the integral has the correct dimension for arbitrary d. Since the integral is analytic in Euclidean space, we can perform a Wick rotation $k^0 \mapsto ik^0$. The integral measure can be rewritten in terms of polar coordinates,

$$\int d^d k = \int_0^\infty dk\ k^{d-1} \int_0^{2\pi} d\phi \int_0^\pi d\theta_{d-2} \sin(\theta_{d-2}) \ldots \int_0^\pi d\theta_1 \sin^2(\theta_1). \tag{C.2}$$

The angular integration is via the formula,

$$\int_0^\pi d\theta \sin^n \theta = \frac{\Gamma(\frac{n+1}{2})\,\Gamma(\frac{1}{2})}{\Gamma(\frac{n}{2}+1)}, \quad n \in \mathbb{N}, \tag{C.3}$$

and along with the following representation of the beta-function,

$$B(a+1, b+1) = \int_0^\infty dt\, t^a\, (t+1)^{-2-a-b} = \frac{\Gamma(a+1)\,\Gamma(b+1)}{\Gamma(a+b+2)}, \quad \text{for } \mathrm{Re}(x), \mathrm{Re}(y) > 0 \tag{C.4}$$

we find the following expression for the loop integral [99],

$$A_0(M^2) = (M^2)^{\frac{d}{2}-1}\, \frac{\mu^{4-d}}{(4\pi)^{\frac{d}{2}}}\, \Gamma\left(1 - \frac{d}{2}\right). \tag{C.5}$$

At $d \mapsto 4$, the Γ function contains a pole. The properties of the Γ function can be used to expand the right hand side of the above expression in $\frac{1}{d-4}$, to obtain

$$A_0(M^2) = \frac{M^2}{16\pi^2}\left[2\lambda + \ln\left(\frac{M^2}{\mu^2}\right) + O(d-4)\right], \tag{C.6}$$

where $\Gamma'(1) = \gamma_E$ is the Euler-Mascheroni constant. The pole is contained in λ,

$$\lambda = \frac{1}{4\pi^2}\,\mu^{d-4}\left[\frac{1}{d-4} - \frac{1}{2}\left(\ln 4\pi + \Gamma'(1) + 1\right)\right]. \tag{C.7}$$

This motivates the definition of the renormalised LECs in Eq. (3.52):

$$\begin{aligned} l_i &= l_i^r + \gamma_i\lambda, \quad i = 1, ..., 7 \\ h_i &= h_i^r + \delta_i\lambda, \quad i = 1, 2, 3, \end{aligned}$$

and the coefficients γ_i are given by

$$\gamma_1 = \frac{1}{3}, \quad \gamma_2 = \frac{2}{3}, \quad \gamma_3 = -\frac{1}{2}, \quad \gamma_4 = 2. \tag{C.8}$$

Next, we require the scalar two-point loop integral for the calculation of the diagram Fig. 3.3. This loop integral is logarithmically divergent and has the form,

$$B_0\left(q^2, M^2\right) = \mu^{4-d}\int \frac{d^dk}{(2\pi)^d}\frac{i}{\left(k^2 - M^2\right)\left[(k+q)^2 - M^2\right]}, \tag{C.9}$$

where q is the loop momentum. Firstly, we apply Feynman's trick is applied to combine the denominator:

$$\frac{1}{A\cdot B} = \int_0^1 dx \frac{1}{\left[Ax + B(1-x)\right]^2}, \tag{C.10}$$

which gives

$$B_0\left(q^2, M^2\right) = \mu^{4-d}\int \frac{d^dk}{(2\pi)^d}\int_0^1 dx \frac{i}{\left[k^2 + x(q^2 - 2k\cdot q) - M^2\right]^2}. \tag{C.11}$$

Now, with a variable shift $k \to k + xq$,

$$B_0\left(q^2, M^2\right) = \mu^{4-d}\int \frac{d^dk}{(2\pi)^d}\int_0^1 dx \frac{i}{\left[k^2 + x(x-1)q^2 - M^2\right]^2}. \tag{C.12}$$

We can Wick rotate the momentum variable k, then perform the angular integration and expand in $(d-4)$ as in the previous case to obtain,

$$B_0\left(q^2, M^2\right) = \frac{1}{16\pi^2}\left[2\lambda + \ln\left(\frac{M^2}{\mu^2}\right) + 1 + \bar{J}(q^2) + O(d-4)\right]. \tag{C.13}$$

where the loop function is given by,

$$\begin{aligned}
\bar{J}(q^2) &= \int_0^1 dx \frac{1}{\left[M^2 + x(1-x)q^2\right]^{d-4}} \\
&= \int_0^1 dx \, \exp\left\{(d-4)\ln\left(\frac{M^2 + x(1-x)q^2}{4\pi\mu^2}\right)\right\} \\
&= \frac{1}{16\pi^2}\left[\sigma(q^2)\ln\frac{\sigma(q^2)-1}{\sigma(q^2)+1} + 2\right], \quad x > 4M^2
\end{aligned} \tag{C.14}$$

with the phase space factor,

$$\sigma(q^2) = \sqrt{1 - \frac{4M^2}{q^2}}. \tag{C.15}$$

APPENDIX D

Numerical Quantities

D.1 Error Analysis

The errors in our fitting procedure outlined in Chapter 6 are calculcated via the simple procedure described here. For any quantity F which is a function of variables $\{a_i\}$, each variable contains its known central value and an assumed symmetric error,

$$a_i = a_i^c \pm \delta a_i. \tag{D.1}$$

These errors of the different variables are assumed to be uncorrelated. In this case, the error of the function F is given by the quadrature formula [100],

$$\delta F = \sqrt{\sum_i \left(\frac{\partial F}{\partial a_i}\delta a_i\right)^2}. \tag{D.2}$$

Since F may depend upon the variables $\{a_i\}$ in a complicated manner, we approximate the partial derivative as,

$$\frac{\partial F}{\partial a_i} \approx \frac{F\left(a_i^c + \delta a_i, \{a_j^c\}_{j\neq i}\right) - F\left(a_i^c - \delta a_i, \{a_j^c\}_{j\neq i}\right)}{2\delta a_i}. \tag{D.3}$$

This allows us to rewrite the uncertainty of F as,

$$\delta F \approx \frac{1}{2}\sqrt{\sum_i \left(F\left(a_i^c + \delta a_i, \{a_j^c\}_{j\neq i}\right) - F\left(a_i^c - \delta a_i, \{a_j^c\}_{j\neq i}\right)\right)^2}, \tag{D.4}$$

which is then implemented numerically in our calculations.

D.2 Quantities at Infinite Volume

As mentioned in Chapter 6, we use the lattice ensembles A40.32 and A40.24 provided to us by the European Twisted Mass (ETM) Collaboration [76, 93]. In order to carry out the fitting of our analytical threshold parameters with the discrete energy level data for the correlation functions of the

connected diagrams, we need to relate the infinite volume pion mass and pion-decay constant to the finite volume values used by the collaboration. This involves a simple correction to the finite volume values, depending on the lattice spacing a and the lattice size L.

- Values in the finite volume ($f_\pi = \sqrt{2}F_\pi$):
  1. A40.32: $M_\pi = 0.1415(2)$, $\frac{M_\pi}{f_\pi} = 2.068(08)$.
  2. A40.24: $M_\pi = 0.1446(3)$, $\frac{M_\pi}{f_\pi} = 2.202(13)$.
- The relation between the finite and infinite volume values is provided by the *finite volume factor*:

$$O^\infty = \frac{O^{FV}}{K}. \tag{D.5}$$

  Thus, we obtain for the pion mass and pion-decay constant,

$$M_\pi^\infty = \frac{M_\pi^{FV}}{K_{M_\pi}} \frac{M_\pi^\infty}{f_\pi} = \left(\frac{M_\pi^\infty}{f_\pi}\right)^{FV} \frac{K_{f_\pi}}{K_{M_\pi}}. \tag{D.6}$$

- The correction factors are given to be:
  1. A40.32: $K_{M_\pi} = 1.0039(28)$, $K_{f_\pi} = 0.9874(24)$.
  2. A40.24: $K_{M_\pi} = 1.0206(95)$, $K_{f_\pi} = 0.9406(84)$.
- Pion mass and pion-decay constant at infinite volume: Computing the errors using the quadrature formula in the previous section, we obtain for $L \mapsto \infty$,
  1. A40.32: $M_\pi^\infty = 0.14095(44)$, $\left(\frac{M_\pi}{f_\pi}\right)^\infty = 2.034(11)$.
  2. A40.24: $M_\pi^\infty = 0.14168(135)$, $\left(\frac{M_\pi}{f_\pi}\right)^\infty = 2.029(29)$.

The values from the two ensembles A40.32 and A40.24 are combined by using a weighted mean,

$$\overline{x} = \frac{\sum_i x_i \sigma_i^{-2}}{\sum_i \sigma_i^{-2}}, \tag{D.7}$$

where the standard deviation σ is,

$$\sigma_{\overline{x}} = \sqrt{\frac{1}{\sum_i \sigma_i^{-2}}}. \tag{D.8}$$

We finally obtain our values:

$$M_\pi^\infty = 0.14102(42), \quad \left(\frac{M_\pi}{F_\pi}\right)^\infty = 2.876(14). \tag{D.9}$$

Bibliography

[1] N. R. Acharya et al., *Connected and disconnected contractions in pion–pion scattering*, Nucl. Phys. **B922** (2017) 480, arXiv: 1704.06754 [hep-lat] (cit. on pp. 2, 35, 38, 54, 65).

[2] N. R. Acharya et al., *Constraints on disconnected contributions in $\pi\pi$ scattering*, JHEP **04** (2019) 165, arXiv: 1902.10290 [hep-lat] (cit. on pp. 2, 54, 56, 57, 59, 65, 66).

[3] N. R. Acharya et al., *Theta-dependence of the lightest meson resonances in QCD*, Phys. Rev. **D92** (2015) 054023, arXiv: 1507.08570 [hep-ph] (cit. on p. 3).

[4] S. Glashow, *Partial Symmetries of Weak Interactions*, Nucl. Phys. **22** (1961) 579 (cit. on p. 5).

[5] S. Weinberg, *A Model of Leptons*, Phys. Rev. Lett. **19** (1967) 1264 (cit. on p. 5).

[6] A. Salam, *Weak and Electromagnetic Interactions*, Conf. Proc. **C680519** (1968) 367 (cit. on p. 5).

[7] J. W. F. Valle, *Neutrinos and the challenges of particle physics*, PoS **NOW2018** (2019) 022, arXiv: 1812.07945 [hep-ph] (cit. on p. 5).

[8] B. Wang et al., *Dark Matter and Dark Energy Interactions: Theoretical Challenges, Cosmological Implications and Observational Signatures*, Rept. Prog. Phys. **79** (2016) 096901, arXiv: 1603.08299 [astro-ph.CO] (cit. on p. 5).

[9] E. Graverini, *Flavour anomalies: a review*, J. Phys. Conf. Ser. **1137** (2019) 012025, arXiv: 1807.11373 [hep-ex] (cit. on p. 5).

[10] P. W. Higgs, *Broken symmetries, massless particles and gauge fields*, Phys. Lett. **12** (1964) 132 (cit. on p. 6).

[11] F. Englert and R. Brout, *Broken Symmetry and the Mass of Gauge Vector Mesons*, Phys. Rev. Lett. **13** (1964) 321, [,157(1964)] (cit. on p. 6).

[12] G. Luders, *Proof of the TCP theorem*, Annals Phys. **2** (1957) 1, [Annals Phys.281,1004(2000)] (cit. on p. 7).

[13] F.-K. Guo and U.-G. Meissner, *Baryon electric dipole moments from strong CP violation*, JHEP **12** (2012) 097, arXiv: 1210.5887 [hep-ph] (cit. on p. 7).

[14] V. Baluni, *CP Violating Effects in QCD*, Phys. Rev. **D19** (1979) 2227 (cit. on p. 8).

[15] R. J. Crewther et al., *Chiral Estimate of the Electric Dipole Moment of the Neutron in Quantum Chromodynamics*, Phys. Lett. **88B** (1979) 123, [Erratum: Phys. Lett.91B,487(1980)] (cit. on p. 8).

[16] F.-K. Guo and U.-G. Meißner, *Cumulants of the QCD topological charge distribution*, Phys. Lett. **B749** (2015) 278, arXiv: 1506.05487 [hep-ph] (cit. on p. 8).

[17] M. Tanabashi et al., *Review of Particle Physics*, Phys. Rev. **D98** (2018) 030001 (cit. on pp. 8, 12, 20).

[18] S. L. Adler, *Axial vector vertex in spinor electrodynamics*, Phys. Rev. **177** (1969) 2426, [,241(1969)] (cit. on p. 10).

[19] J. S. Bell and R. Jackiw, *A PCAC puzzle: $\pi^0 \to \gamma\gamma$ in the σ model*, Nuovo Cim. **A60** (1969) 47 (cit. on p. 10).

[20] S. Scherer and M. R. Schindler, *A Primer for Chiral Perturbation Theory*, Lect. Notes Phys. **830** (2012) pp.1 (cit. on p. 11).

[21] C. Vafa and E. Witten, *Restrictions on Symmetry Breaking in Vector-Like Gauge Theories*, Nucl. Phys. **B234** (1984) 173 (cit. on p. 11).

[22] S. R. Coleman and J. Mandula, *All Possible Symmetries of the S Matrix*, Phys. Rev. **159** (1967) 1251 (cit. on p. 12).

[23] Y. Nambu, *Axial vector current conservation in weak interactions*, Phys. Rev. Lett. **4** (1960) 380, [,107(1960)] (cit. on p. 12).

[24] J. Goldstone, *Field Theories with Superconductor Solutions*, Nuovo Cim. **19** (1961) 154 (cit. on p. 12).

[25] J. Goldstone, A. Salam and S. Weinberg, *Broken Symmetries*, Phys. Rev. **127** (1962) 965 (cit. on p. 12).

[26] K. G. Wilson, *The Renormalization Group and Strong Interactions*, Phys. Rev. **D3** (1971) 1818 (cit. on p. 13).

[27] D. J. Gross and F. Wilczek, *Ultraviolet Behavior of Nonabelian Gauge Theories*, Phys. Rev. Lett. **30** (1973) 1343, [,271(1973)] (cit. on p. 13).

[28] S. Aoki et al., *FLAG Review 2019*, (2019), arXiv: 1902.08191 [hep-lat] (cit. on p. 13).

[29] S. Weinberg, *Phenomenological Lagrangians*, Physica **A96** (1979) 327 (cit. on pp. 15, 17, 23).

[30] U. G. Meissner, *Recent developments in chiral perturbation theory*, Rept. Prog. Phys. **56** (1993) 903, arXiv: hep-ph/9302247 [hep-ph] (cit. on p. 17).

[31] J. Bijnens, G. Colangelo and G. Ecker, *The Mesonic chiral Lagrangian of order p**6*, JHEP **02** (1999) 020, arXiv: hep-ph/9902437 [hep-ph] (cit. on p. 17).

[32] A. A. Petrov and A. E. Blechman, *Effective Field Theories*, WSP, 2016, ISBN: 9789814434928, 9789814434942, URL: http://www.worldscientific.com/worldscibooks/10.1142/8619 (cit. on p. 20).

[33] J. Gasser and H. Leutwyler, *Chiral Perturbation Theory to One Loop*, Annals Phys. **158** (1984) 142 (cit. on pp. 21, 24, 27–29, 35, 47, 65).

[34] M. Gell-Mann, R. J. Oakes and B. Renner, *Behavior of current divergences under SU(3) x SU(3)*, Phys. Rev. **175** (1968) 2195 (cit. on p. 21).

[35] J. L. Petersen, *Meson-meson scattering*, Phys. Rept. **2** (1971) 155 (cit. on p. 23).

[36] S. Weinberg, *The Quantum theory of fields. Vol. 1: Foundations*, Cambridge University Press, 2005, ISBN: 9780521670531, 9780511252044 (cit. on p. 24).

[37] J. Gasser and H. Leutwyler, *Chiral Perturbation Theory: Expansions in the Mass of the Strange Quark*, Nucl. Phys. **B250** (1985) 465 (cit. on pp. 25, 35).

[38] C. W. Bernard and M. F. L. Golterman, *Partially quenched gauge theories and an application to staggered fermions*, Phys. Rev. **D49** (1994) 486, arXiv: hep-lat/9306005 [hep-lat] (cit. on p. 31).

[39] S. R. Sharpe and N. Shoresh, *Physical results from unphysical simulations*, Phys. Rev. **D62** (2000) 094503, arXiv: hep-lat/0006017 [hep-lat] (cit. on p. 31).

[40] C. Bernard and M. Golterman, *On the foundations of partially quenched chiral perturbation theory*, Phys. Rev. **D88** (2013) 014004, arXiv: 1304.1948 [hep-lat] (cit. on p. 31).

[41] S. Sharpe, "Applications of Chiral Perturbation theory to lattice QCD", *Workshop on Perspectives in Lattice QCD Nara, Japan, October 31-November 11, 2005*, 2006, arXiv: hep-lat/0607016 [hep-lat] (cit. on pp. 31, 33).

[42] M. Golterman, "Applications of chiral perturbation theory to lattice QCD", *Modern perspectives in lattice QCD: Quantum field theory and high performance computing. Proceedings, International School, 93rd Session, Les Houches, France, August 3-28, 2009*, 2009 423, arXiv: 0912.4042 [hep-lat], URL: http://inspirehep.net/record/840837/files/arXiv:0912.4042.pdf (cit. on p. 31).

[43] A. Morel, *Chiral Logarithms in Quenched QCD*, J. Phys.(France) **48** (1987) 1111 (cit. on p. 32).

[44] M. Golterman, S. R. Sharpe and R. L. Singleton Jr., *Effective theory for quenched lattice QCD and the Aaoki phase*, Phys. Rev. **D71** (2005) 094503, arXiv: hep-lat/0501015 [hep-lat] (cit. on p. 33).

[45] S. R. Sharpe and N. Shoresh, *Partially quenched chiral perturbation theory without Phi0*, Phys. Rev. **D64** (2001) 114510, arXiv: hep-lat/0108003 [hep-lat] (cit. on pp. 33, 34).

[46] L. Giusti and M. Lüscher, *Chiral symmetry breaking and the Banks-Casher relation in lattice QCD with Wilson quarks*, JHEP **03** (2009) 013, arXiv: 0812.3638 [hep-lat] (cit. on p. 34).

[47] S. R. Sharpe and R. S. Van de Water, *Unphysical operators in partially quenched QCD*, Phys. Rev. **D69** (2004) 054027, arXiv: hep-lat/0310012 [hep-lat] (cit. on p. 35).

[48] S. R. Sharpe, R. Gupta and G. W. Kilcup, *Lattice calculation of $I = 2$ pion scattering length*, Nucl. Phys. **B383** (1992) 309 (cit. on p. 37).

[49] R. Gupta, A. Patel and S. R. Sharpe, *$I = 2$ pion scattering amplitude with Wilson fermions*, Phys. Rev. **D48** (1993) 388, arXiv: hep-lat/9301016 [hep-lat] (cit. on p. 37).

[50] Y. Kuramashi et al., *Lattice QCD calculation of full pion scattering lengths*, Phys. Rev. Lett. **71** (1993) 2387 (cit. on pp. 37, 39).

[51] M. Fukugita et al., *Hadron scattering lengths in lattice QCD*, Phys. Rev. **D52** (1995) 3003, arXiv: hep-lat/9501024 [hep-lat] (cit. on p. 37).

[52] S. Aoki et al., *I=2 pion scattering length with the Wilson fermion*, Phys. Rev. **D66** (2002) 077501, arXiv: hep-lat/0206011 [hep-lat] (cit. on p. 37).

[53] X. Du et al., *I = 2 pion scattering length with improved actions on anisotropic lattices*, Int. J. Mod. Phys. **A19** (2004) 5609, arXiv: hep-lat/0404017 [hep-lat] (cit. on p. 37).

[54] J.-W. Chen et al., *Ginsparg-Wilson pions scattering on a staggered sea*, Phys. Rev. **D73** (2006) 074510, arXiv: hep-lat/0510024 [hep-lat] (cit. on p. 37).

[55] X. Li et al., *Anisotropic lattice calculation of pion scattering using an asymmetric box*, JHEP **06** (2007) 053, arXiv: hep-lat/0703015 [hep-lat] (cit. on p. 37).

[56] S. R. Beane et al., *Precise Determination of the I=2 pi pi Scattering Length from Mixed-Action Lattice QCD*, Phys. Rev. **D77** (2008) 014505, arXiv: 0706.3026 [hep-lat] (cit. on p. 37).

[57] S. Aoki et al., *Lattice QCD Calculation of the rho Meson Decay Width*, Phys. Rev. **D76** (2007) 094506, arXiv: 0708.3705 [hep-lat] (cit. on p. 37).

[58] X. Feng, K. Jansen and D. B. Renner, *The pi+ pi+ scattering length from maximally twisted mass lattice QCD*, Phys. Lett. **B684** (2010) 268, arXiv: 0909.3255 [hep-lat] (cit. on pp. 37, 58).

[59] X. Feng, K. Jansen and D. B. Renner, *Resonance Parameters of the rho-Meson from Lattice QCD*, Phys. Rev. **D83** (2011) 094505, arXiv: 1011.5288 [hep-lat] (cit. on p. 37).

[60] J. J. Dudek et al., *The phase-shift of isospin-2 pi-pi scattering from lattice QCD*, Phys. Rev. **D83** (2011) 071504, arXiv: 1011.6352 [hep-ph] (cit. on p. 37).

[61] C. B. Lang et al., *Coupled channel analysis of the rho meson decay in lattice QCD*, Phys. Rev. **D84** (2011) 054503, [Erratum: Phys. Rev.D89,no.5,059903(2014)], arXiv: 1105.5636 [hep-lat] (cit. on p. 37).

[62] S. Aoki et al., *ρ Meson Decay in 2+1 Flavor Lattice QCD*, Phys. Rev. **D84** (2011) 094505, arXiv: 1106.5365 [hep-lat] (cit. on p. 37).

[63] S. R. Beane et al., *The I=2 pipi S-wave Scattering Phase Shift from Lattice QCD*, Phys. Rev. **D85** (2012) 034505, arXiv: 1107.5023 [hep-lat] (cit. on p. 37).

[64] J. J. Dudek, R. G. Edwards and C. E. Thomas, *S and D-wave phase shifts in isospin-2 pi pi scattering from lattice QCD*, Phys. Rev. **D86** (2012) 034031, arXiv: 1203.6041 [hep-ph] (cit. on p. 37).

[65] C. Pelissier and A. Alexandru, *Resonance parameters of the rho-meson from asymmetrical lattices*, Phys. Rev. **D87** (2013) 014503, arXiv: 1211.0092 [hep-lat] (cit. on p. 37).

[66] J. J. Dudek, R. G. Edwards and C. E. Thomas, *Energy dependence of the ρ resonance in $\pi\pi$ elastic scattering from lattice QCD*, Phys. Rev. **D87** (2013) 034505, [Erratum: Phys. Rev.D90,no.9,099902(2014)], arXiv: 1212.0830 [hep-ph] (cit. on p. 37).

[67] Z. Fu, *Lattice QCD study of the s-wave ππ scattering lengths in the I=0 and 2 channels*, Phys. Rev. **D87** (2013) 074501, arXiv: 1303.0517 [hep-lat] (cit. on p. 37).

[68] X. Feng et al., *Timelike pion form factor in lattice QCD*, Phys. Rev. **D91** (2015) 054504, arXiv: 1412.6319 [hep-lat] (cit. on p. 37).

[69] Z. Bai et al., *Standard Model Prediction for Direct CP Violation in $K \to \pi\pi$ Decay*, Phys. Rev. Lett. **115** (2015) 212001, arXiv: 1505.07863 [hep-lat] (cit. on p. 37).

[70] C. Helmes et al., *Hadron-hadron interactions from $N_f = 2 + 1 + 1$ lattice QCD: isospin-2 ππ scattering length*, JHEP **09** (2015) 109, arXiv: 1506.00408 [hep-lat] (cit. on pp. 37, 59, 60).

[71] D. J. Wilson et al., *Coupled $\pi\pi, K\bar{K}$ scattering in P-wave and the ρ resonance from lattice QCD*, Phys. Rev. **D92** (2015) 094502, arXiv: 1507.02599 [hep-ph] (cit. on p. 37).

[72] G. S. Bali et al., *ρ and K^* resonances on the lattice at nearly physical quark masses and $N_f = 2$*, Phys. Rev. **D93** (2016) 054509, arXiv: 1512.08678 [hep-lat] (cit. on p. 37).

[73] J. Bulava et al., *$I = 1$ and $I = 2$ $\pi - \pi$ scattering phase shifts from $N_f = 2 + 1$ lattice QCD*, Nucl. Phys. **B910** (2016) 842, arXiv: 1604.05593 [hep-lat] (cit. on p. 37).

[74] D. Guo et al., *Rho resonance parameters from lattice QCD*, Phys. Rev. **D94** (2016) 034501, arXiv: 1605.03993 [hep-lat] (cit. on p. 37).

[75] R. A. Briceño et al., *Isoscalar ππ scattering and the σ meson resonance from QCD*, Phys. Rev. Lett. **118** (2017) 022002, arXiv: 1607.05900 [hep-ph] (cit. on p. 37).

[76] L. Liu et al., *Isospin-0 ππ s-wave scattering length from twisted mass lattice QCD*, Phys. Rev. **D96** (2017) 054516, arXiv: 1612.02061 [hep-lat] (cit. on pp. 37, 58–60, 77).

[77] C. Alexandrou et al., *P-wave ππ scattering and the ρ resonance from lattice QCD*, Phys. Rev. **D96** (2017) 034525, arXiv: 1704.05439 [hep-lat] (cit. on p. 37).

[78] F.-K. Guo et al., *Tetraquarks, hadronic molecules, meson-meson scattering and disconnected contributions in lattice QCD*, Phys. Rev. **D88** (2013) 074506, arXiv: 1308.2545 [hep-lat] (cit. on pp. 38, 41).

[79] M. Della Morte and A. Jüttner, *Quark disconnected diagrams in chiral perturbation theory*, JHEP **11** (2010) 154, arXiv: 1009.3783 [hep-lat] (cit. on p. 38).

[80] A. Juttner, *Revisiting the pion's scalar form factor in chiral perturbation theory*, JHEP **01** (2012) 007, arXiv: 1110.4859 [hep-lat] (cit. on p. 38).

[81] G. Passarino and M. J. G. Veltman, *One Loop Corrections for e+ e- Annihilation Into mu+ mu- in the Weinberg Model*, Nucl. Phys. **B160** (1979) 151 (cit. on p. 42).

[82] G. Colangelo, J. Gasser and H. Leutwyler, *ππ scattering*, Nucl. Phys. **B603** (2001) 125, arXiv: hep-ph/0103088 [hep-ph] (cit. on pp. 45–47).

[83] J. Bijnens and G. Ecker, *Mesonic low-energy constants*, Ann. Rev. Nucl. Part. Sci. **64** (2014) 149, arXiv: 1405.6488 [hep-ph] (cit. on pp. 45–47).

[84] P. A. Boyle et al., *Low energy constants of SU(2) partially quenched chiral perturbation theory from N_f=2+1 domain wall QCD*, Phys. Rev. **D93** (2016) 054502, arXiv: 1511.01950 [hep-lat] (cit. on pp. 45–47, 60, 61).

[85] M. Luscher, *Volume Dependence of the Energy Spectrum in Massive Quantum Field Theories. 2. Scattering States*, Commun. Math. Phys. **105** (1986) 153 (cit. on p. 51).

[86] M. Luscher, *Two particle states on a torus and their relation to the scattering matrix*, Nucl. Phys. **B354** (1991) 531 (cit. on p. 51).

[87] R. J. Eden et al., *The analytic S-matrix*, Cambridge Univ. Press, 1966 (cit. on pp. 51, 54).

[88] E. E. Salpeter and H. A. Bethe, *A Relativistic equation for bound state problems*, Phys. Rev. **84** (1951) 1232 (cit. on p. 53).

[89] J. A. Oller, E. Oset and J. R. Pelaez, *Meson meson interaction in a nonperturbative chiral approach*, Phys. Rev. **D59** (1999) 074001, [Erratum: Phys. Rev.D75,099903(2007)], arXiv: hep-ph/9804209 [hep-ph] (cit. on p. 53).

[90] M. Döring et al., *Unitarized Chiral Perturbation Theory in a finite volume: Scalar meson sector*, Eur. Phys. J. **A47** (2011) 139, arXiv: 1107.3988 [hep-lat] (cit. on p. 53).

[91] M. Doring et al., *Dynamical coupled-channel approaches on a momentum lattice*, Eur. Phys. J. **A47** (2011) 163, arXiv: 1108.0676 [hep-lat] (cit. on p. 53).

[92] T. DeGrand and C. E. Detar, *Lattice methods for quantum chromodynamics*, 2006 (cit. on p. 53).

[93] R. Baron et al., *Light hadrons from lattice QCD with light (u,d), strange and charm dynamical quarks*, JHEP **06** (2010) 111, arXiv: 1004.5284 [hep-lat] (cit. on pp. 58, 61, 77).

[94] E. Noether, *Invariant Variation Problems*, Gott. Nachr. **1918** (1918) 235, [Transp. Theory Statist. Phys.1,186(1971)], arXiv: physics/0503066 [physics] (cit. on p. 67).

[95] M. Gell-Mann and M. Levy, *The axial vector current in beta decay*, Nuovo Cim. **16** (1960) 705 (cit. on p. 67).

[96] G. Costa and G. Fogli, *Symmetries and group theory in particle physics. An introduction to space-time and internal symmetries*, Lect. Notes Phys. **823** (2012) 1 (cit. on p. 69).

[97] B. S. DeWitt, *Supermanifolds*, Cambridge Monographs on Mathematical Physics, Cambridge Univ. Press, 2012, ISBN: 9781139240512, 9780521423779, URL: http://www.cambridge.org/mw/academic/subjects/physics/theoretical-physics-and-mathematical-physics/supermanifolds-2nd-edition?format=AR (cit. on p. 70).

[98] P. G. O. Freund, *Introduction to Supersymmetry*,
Cambridge Monographs on Mathematical Physics, Cambridge Univ. Press, 2012,
ISBN: 9781139241939, 9780521356756,
URL: http://www.cambridge.org/mw/academic/subjects/physics/theoretical-physics-and-mathematical-physics/introduction-supersymmetry?format=AR
(cit. on p. 70).

[99] G. 't Hooft and M. J. G. Veltman, *Regularization and Renormalization of Gauge Fields*,
Nucl. Phys. **B44** (1972) 189 (cit. on p. 73).

[100] L. Lista, *Statistical Methods for Data Analysis in Particle Physics*,
Lect. Notes Phys. **941** (2017) 1 (cit. on p. 77).

List of Figures

List of Tables